



WE-NEED

WatEr NEEDs, availability, quality and sustainability



Deliverable Number:	D1.4a
Work package number:	WP1
Deliverable title	REPORT ON CHARACTERIZATION OF FIELD SITES
Type	Report
Dissemination Level	Public

Lead participant	Politecnico di Milano
Contributing scientists and other personnel	Emanuela Bianchi Janetti, Laura Guadagnini, Martina Siena, Ceriotti Giulia, Dell'Oca Aronne, Fadji Zaouna Maina, Guadagnini Alberto, Porta Giovanni Michele, Orsi Enrico Maria, Matteo Valsecchi, Monica Riva

Scheduled delivery date	20 October 2017
Actual / forecast delivery date	20 October 2017

Deliverable summary

This document provides preliminary results obtained in the context of hydrogeological characterization of the two field sites analysed in the project: Cremona and Bologna Aquifer systems, located in the Po Plain, Northern Italy. The analysis of available sedimentological information allows to identify the main classes of geomaterials (or facies) that constitute the geological makeup of each system. The heterogeneous structures of these aquifers are modelled by stochastic distributions of facies, conditioned on the basis of the available data. For the Cremona site, the aquifer architecture is reconstructed with a sequential indicator algorithm. Then, hydraulic conductivity distributions are inferred on the basis of two diverse conceptual schemes: (1) Composite Medium and (2) Overlapping Continuum. For both the approaches, groundwater flow is simulated. A Global Sensitivity Analysis is performed to assess the impact of the uncertainty associated with (a) the spatial distribution of hydraulic conductivity, and (b) the conceptual model adopted to describe the system, including boundary conditions. For the Bologna site, we compare the performance of two techniques for the reconstruction of facies distributions, respectively based on (1) sequential indicator and (2) transition probability simulation. For each technique, multiple realizations are generated and analyzed within a Monte Carlo framework. The effect of the reconstruction method is inferred by comparing key ensemble statistics. In each Monte Carlo realization, hydraulic conductivity distribution is calibrated. The results are then examined using formal model quality criteria.



D1.4a

Report on characterization of field sites

Contents

1. Introduction.....	4
2. Cremona site.....	4
2.1 Conceptual and Numerical model.....	7
2.1.1 Probabilistic facies reconstruction.....	7
2.1.2 Groundwater flow model.....	9
2.2 Sensitivity analysis.....	10
2.2.1 Morris Indices	11
2.2.2 Sobol Indices	12
2.3 Results and discussion.....	13
2.3.1 Probabilistic facies reconstruction.....	13
2.3.2 Sensitivity analysis.....	18
2.4 Model Calibration.....	23
2.4.1 Maximum Likelihood Approach	23
2.4.2 Model Identification Criteria	24
2.4.3 Hydraulic conductivity estimates	25
2.5 Ongoing and future planned activities	27
3. Bologna site.....	28
3.1 Conceptual and Numerical model.....	28
3.1.1 Probabilistic facies reconstruction: SISIM simulations.....	30
3.1.2 Probabilistic facies reconstruction: TPROGS simulations.....	31
3.1.2 Groundwater flow model.....	36
3.2 Model Calibration.....	38
3.3 Ongoing and future planned activities	42
References	43
Annex I - Hydrogeological cross sections of the Cremona Aquifer.....	45



Annex II - Hydrogeological cross sections of the Bologna Aquifer 59



1. Introduction

This deliverable provides the preliminary results obtained in the context of hydrogeological characterization of the two field sites analysed within the project: the Bologna and the Cremona Aquifer systems, representing different but complementary realities. The *Bologna Aquifer* is a key source of water for the metropolitan area of Bologna. The *Cremona Aquifer* is located in the so-called *Springs Belt*. Natural high-quality water springs are the main supply to agriculture and a key environmental driver. The *Bologna* and *Cremona* sites are archetypal of two distinct realities of alluvial aquifers, and can be considered representative of diverse environmental settings of Europe-wide interest.

The deliverable is structured as follows: Section 2 provides the analysis performed for the Cremona site. The methodology applied for aquifer architecture reconstruction is described in Section 2.1, the sensitivity analysis in Section 2.2 and the main results we obtained in Section 2.3. Section 2.4 focuses on parameter calibration while ongoing and future planned activities are listed in Section 2.5. The techniques used for the reconstruction of facies distributions for the Bologna site are detailed in Section 3, which includes the description of conceptual and numerical model (Section 3.1), model calibration (Section 3.2) and ongoing and future planned activities (Section 3.3). The characterization of the two field sites is expected to be completed at month 30th of the project.

2. Cremona site

The study area is part of the high-medium Alluvial Po Plain. It lies between the city of Bergamo (Northern Italy) and the confluence of the Adda and Serio rivers (see Figure 2.1). The planar surface of the investigated domain is about 785 km² and it contains both agricultural (84%) and urban (16%) regions. A key feature of the study area is the occurrence of high-quality water springs, which are the main supply to agriculture and a key environmental driver. The area is part of the so-called “springs belt” located at the transition between the high plain, characterized by an upper thickness formed by coarse alluvial deposits within which a mainly phreatic aquifer is hosted, and the low plain where the topographic surface becomes less steep and clayey sediments with lower hydraulic conductivity become more abundant.

Natural springs constitute treasures around which local economies thrive, governing population fluxes and favouring social prosperity. They form a unique ecosystem with a remarkable appeal for tourism and leisure activities. Figure 2.1b displays the main hydrogeological features of the area including the location of (i) springs, (ii) meteorological stations, (iii) hydrometric level stations and (iv) pumping/monitoring wells, which provide data for this study.

Within the Po plain the groundwater resource is mostly located in the continental and marine strata of Plio-Pleistocene age. The quaternary sedimentary sequence is overall



regressive and is formed by, from the bottom to the top, basal turbiditic sands and clays, a prograding fluvio-deltaic sedimentary wedge, continental sediments (Regione Emilia Romagna, ENI-AGIP, 1998; Regione Lombardia, ENI-AGIP, 2002). We reconstruct the hydrogeological architecture of the study area on the basis of stratigraphic information (<http://www.geoportale.regione.lombardia.it/download-dati>) and reconstructed hydrogeological sections (Maione et al., 1991; Beretta et al., 1992; Regione Lombardia, ENI-AGIP, 2002) (see Figure 2.1b, 2.2 and Annex I).

Due to the aim of the work and data availability, the investigation considers sediments up to 290 m thick (average thickness of 120 m). The aquifer system essentially shows (a) a surface, locally semiconfined, portion generally formed by high transmissivity sediments and characterized by relatively large flow values and (b) a deeper, semiconfined/confined portion characterized by alternation between sediments of various grain sizes and hydraulic conductivity. Recharge is due to infiltration from rainfall, from the northern sector and from water used for irrigation. The hydrogeological setting of the area is schematized in Figure 2.2 which displays a North-South (SECT 1) and an East-West (SECT 2) section. Additional hydrogeological cross-sections are reported in Annex I.

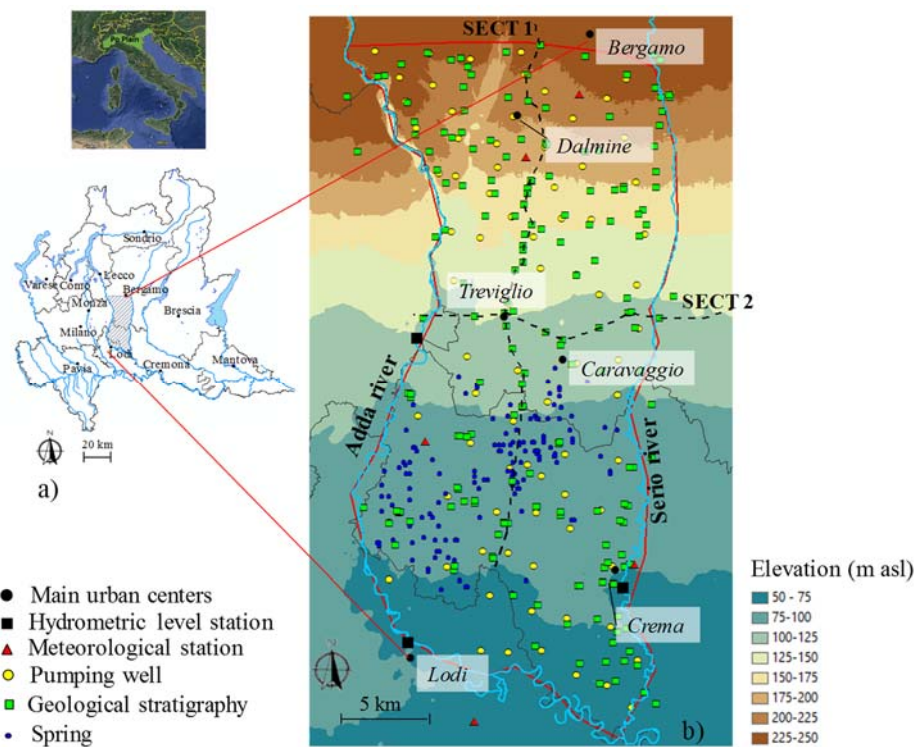


Figure 2.1. a) Geographical framework of the study area (dashed area) within the Lombardia region. b) Location of hydrometric level and meteorological stations, pumping wells, geological stratigraphies and springs.



The superficial thickness of the aquifer consists of clastic continental deposits mainly formed by conglomerate (fluvio-glacial Mindel) in the high plain, fluvio-glacial gravels and sands (Riss-Wurm) in the lowlands and within the erosion furrows in the conglomerate, recent alluvial gravels and sands deposited by rivers. In the Northern portion of the domain the conglomeratic deposit (whose degree of permeability is related to the degree of fracturing) is prevalent, while in the Southern portion loose gravel and sand deposits are more abundant. Layers of clay (with variable planar/lateral continuity) are intercalated within the aquifer. The thickness of the aquifer ranges from 40 to 80 m, along the North-South direction. Then, coarse clastic (fractured conglomerates in the Northern portion of the area) sediments and clays alternate. Inside the porous and/or fractured layers, there are semi-confined or artesian aquifers.

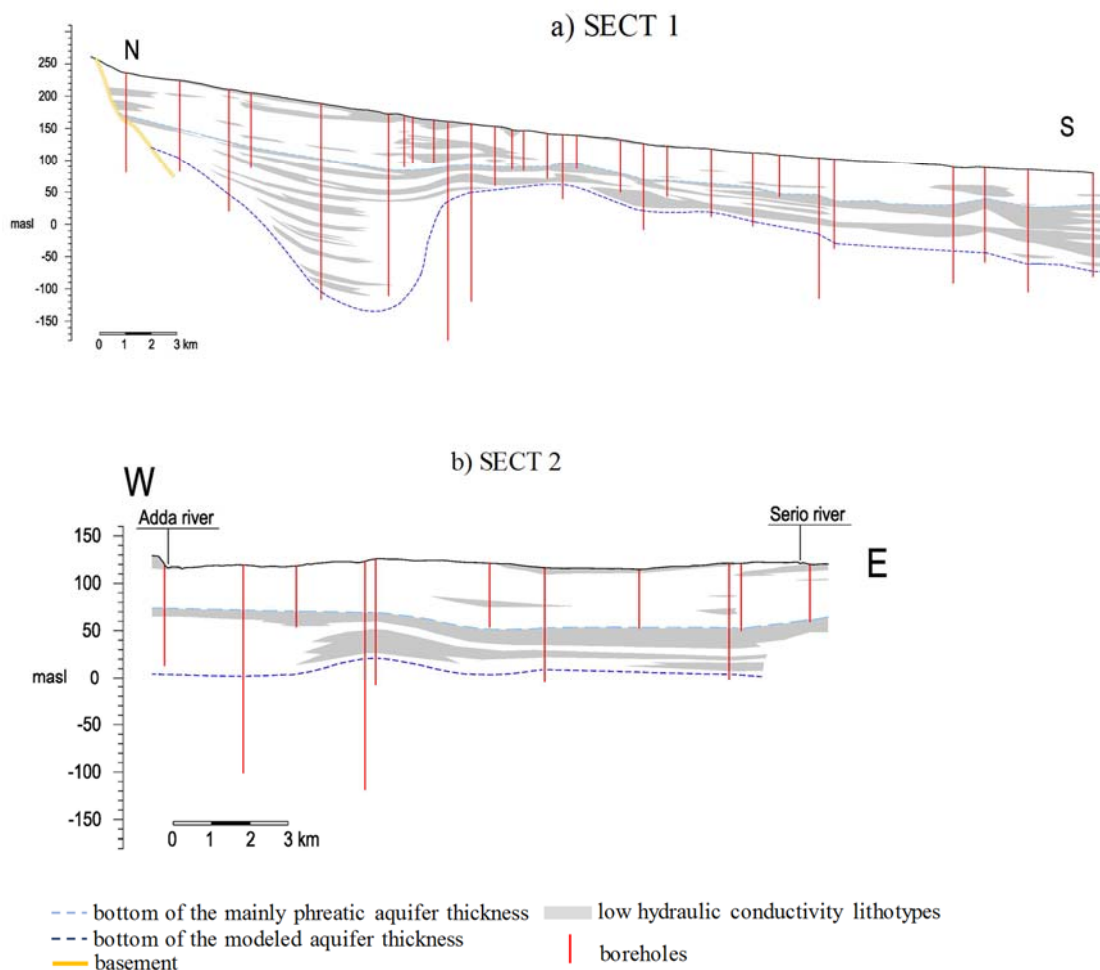


Figure 2.2. a) SECT 1 (North-South direction); b) SECT 2 (West-East direction), modified from Maione et al., 1991.



2.1 Conceptual and Numerical model

2.1.1 Probabilistic facies reconstruction

The following major lithostratigraphic units can be recognized in the area of interest: gravel and sand locally interrupted by silt and clay lenses; alternation of lithotypes formed by gravel, sand, silt and clay; silt and clay deposits with sand inclusions; silt and sand deposits. The data available from stratigraphic information and reconstructed lithostratigraphic sections are homogenized and divided into $n_f = 5$ facies (or classes/geomaterials) summarized in Table 2.1. These five classes form the basis for the definition of indexed variables by which we describe the distribution of geomaterials in the aquifer. According to the texture of each class the hydraulic conductivity values may vary within an interval. Lower and upper bounds of these intervals are reported in Table 2.2.

Based on the described lithologic categorization of the data, we studied the three dimensional distribution of facies within the aquifer by means of geostatistical methods. As previously indicated, we rely on the identification of $n_f = 5$ classes, i.e., 5 geomaterials, identified as M_i ($i = 1, 2, \dots, 5$). We evaluate the variogram of each geomaterial according to the following procedure:

- 1) We start upon assigning a value of the indicator, $I = 1$, to samples where material M_1 is observed, while assigning $I = 0$ to locations where other samples are available.
- 2) Three-dimensional indicator variography is then performed. Resulting sample variograms are interpreted and modeled by different theoretical variograms (Spherical, Gaussian, Exponential, pure Nugget) and key geostatistical parameters (sill, range, nugget, anisotropy pattern) are identified for each class. Model quality criteria are used to select the best variogram model.

Steps 1-2 are repeated for each geomaterial. We followed two different methodologies to reconstruct the spatial variability of the geomaterial, namely “*The Composite Medium approach*” and “*The Overlapping Continuum approach*”.

In the *Composite Medium* approach, each block of the numerical model is formed by a geomaterial. The analysis is based on the following steps:

- 1) Indicator Kriging of facies 1 is performed (Isaaks and Srivastava, 1990) by assigning $I = 1$, to samples where M_1 is observed, while assigning $I = 0$ to locations where M_i with $i \neq 1$ is detected. The zone occupied by M_1 is delimited by the iterative procedure proposed by Guadagnini et al. (2004). The authors imposed a threshold corresponding to the experimental volumetric percentage of M_1 to reconstruct a spatial distribution of M_1 which is consistent with the observed volumetric fractions.
- 2) We reconstruct the region occupied by M_2 by repeating step 1 in the sub-domain external to the region occupied by M_1 . This iterative algorithm is repeated removing,



at each iteration, data relative to the class for which it has already been estimated the related geomaterial spatial distribution until all the cells in the model domain have been assigned to a geomaterial.

- 3) The conductivity value assigned to each cell of the model domain consists in one (constant) value for each facies.

The *Overlapping Continuum* approach considers that the system can be modelled as many composite media coexisting in space. The idea is that each point in the domain represents a finite volume in which each one of the (five) geomaterials can coexist in different volumetric percentage. Indicator Kriging of facies i (with $i = 1, \dots, 5$) is performed. Kriged values of the indicator coincide with the estimated probability (or volumetric percentage) of finding M_i within each block of the domain. The hydraulic conductivity value of a grid cell (or block), K_j , is then calculated as a weighted mean of the conductivities of materials occurring in the block, k_i . We tested the following two weighted averages:

$$(1) \text{ Arithmetic mean (AM)} \quad K_j = \sum_{i=1}^{n_f} I_{i,j} k_i$$

$$(2) \text{ Geometric mean (GM)} \quad K_j = \prod_{i=1}^{n_f} k_i^{I_{i,j}} \quad \text{with } j= 1, 2, \dots, N_j$$

$I_{i,j}$ and N_j being, respectively, the estimated volumetric fraction of geomaterial i within block j (with $\sum_{i=1}^{n_f} I_{i,j} = 1$) and the number of grid blocks. As mentioned above, we assumed that each geomaterial is associated with a constant hydraulic conductivity.

Class	Geological material	Volumetric percentage (%)
1	Clay and silt	36.77
2	Fine and silty sand	4.73
3	Gravel, sand and gravel	32.92
4	Compact conglomerate, sandstone	14.94
5	Fractured conglomerate	10.64

Table 2.1. List of geological materials composing the five classes and related volumetric percentage.



Parameter	Short name	Description	Lower bound	Upper bound	Unit
p_1	k_1	Clay and silt conductivity	10^{-8}	10^{-5}	m/s
p_2	k_2	Fine and silty sand conductivity	10^{-7}	10^{-4}	m/s
p_3	k_3	Gravel, sand and gravel conductivity	10^{-4}	10^{-2}	m/s
p_4	k_4	Compact conglomerate conductivity	10^{-6}	10^{-3}	m/s
p_5	k_5	Fractured conglomerate conductivity	10^{-3}	10^{-1}	m/s
p_6	p_6	Total flow rate from Northern boundary	4.83	14.47	m^3/s
p_7	p_7	River stage	0.0	3.0	m

Table 2.2. Selected uncertain parameters and associated range of variability.

2.1.2 Groundwater flow model

We developed a steady state three-dimensional groundwater flow model covering the area of interest of size 23 km (East-West direction) \times 48 km (North-South direction) \times 475 m (depth). The system is discretised by $230 \times 240 \times 95$ (\approx 5.2 million) cells of uniform size $100 \times 200 \times 5$ m. Inactive cells have been inserted to obtain realistic topography surface of the area and of the bottom of the aquifer. The numerical code MODFLOW-2005 (Harbaugh, 2005) is used to simulate groundwater flow.

Recharge terms included in the model comprise infiltration from precipitations, irrigational water and percolation from channels in the non-urban zones, aqueduct and sewage system losses in the urban region. Withdrawals from the aquifer system are managed by the public administration for drinking, industrial and agricultural purposes. The amount of water withdrawal related to the diverse existing activities is reported in the Catasto Regionale delle Utenze Idriche (<http://www.cittametropolitana.mi.it/>). A complete and up-to-date record reporting the exact location of the complete set of pumping wells is not available. For this reason, we assign the water withdrawal within a given municipality to a system of wells located at the center of the municipality itself. The screens of these pumping wells are set at a depth of $60 \div 80$ m, $40 \div 50$ m or $20 \div 30$ m depending on whether they are supplying drinking water for the population, industrial or agricultural activities, respectively. Springs are simulated as drains and their outflow-rate is proportional to the difference between the hydraulic head and the elevation of ground level.

A Dirichlet boundary condition is imposed to the grid cells located along the Adda and Serio rivers (see Figure 2.3). This choice relies on the results of previous studies, showing that both rivers have a direct hydraulic connection with the groundwater system. Maione et al. (1991) showed how the Adda river drains water from the aquifer along its entire course. The



Serio river partially drains the aquifer, while hydraulic equilibrium conditions with the aquifer are observed along other parts of the river. A Neumann boundary condition is imposed along the Northern boundary of the model (see Figure 2.3).

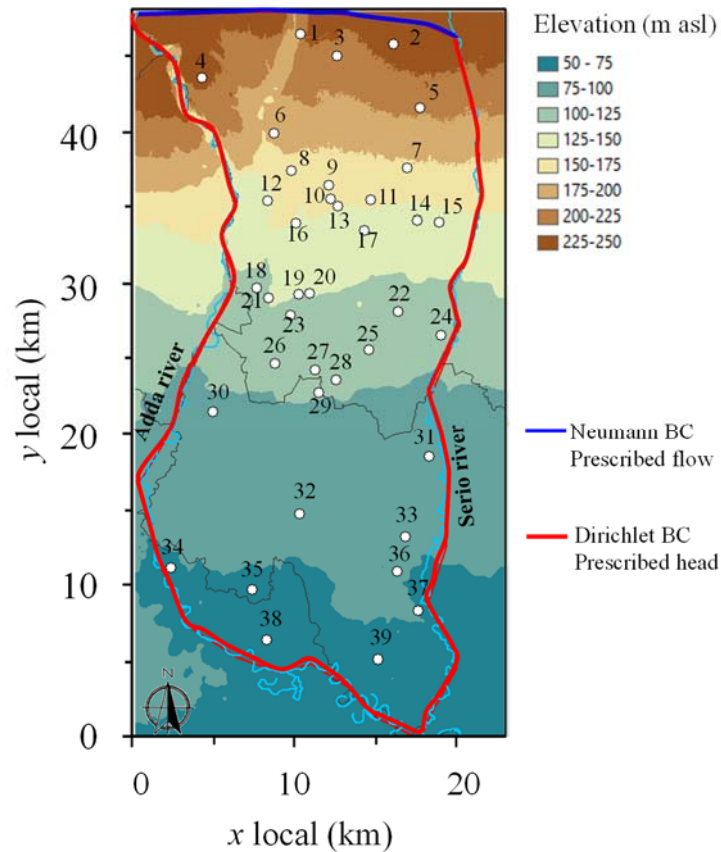


Figure 2.3 Location of monitoring wells and boundary condition of the numerical model.

2.2 Sensitivity analysis

We considered a set of $N = 7$ uncertain parameters (see table 2.2), each one described by a uniform probability distribution within a corresponding interval of variability. These parameters are collected in a vector $\mathbf{p} = (p_1, \dots, p_N)$. The parameter space is then defined as $\Gamma = [\mathbf{p}^{\min}, \mathbf{p}^{\max}]$ where \mathbf{p}^{\min} and \mathbf{p}^{\max} indicate the vectors containing respectively lower and upper bounds of parameter variability intervals. The output of the groundwater model (hydraulic heads) can be expressed as a function of the unknown parameters, i.e. $f(\mathbf{p}) : \Gamma \rightarrow \mathbb{R}$.

In our study, selected uncertain parameters are associated with (i) the hydraulic conductivity (k_i with $i = 1, \dots, 5$) of the five geomaterials composing the aquifer and the model



boundary conditions, i.e. (ii) the total flow rate entering from the Northern boundary (p_6) and (iii) the river stages, delimiting model at the Western, Eastern and Southern sides (p_7). The lower and upper bounds of the intervals of variability of the selected uncertain parameters are listed in Table 2.2. The choice of the width of the intervals associated with hydraulic conductivities (k_i , $i = 1, \dots, 5$) is based on geological features as explained in Section 2.1.1. Considering the boundary conditions, Rametta (2008) estimated a total incoming flow rate, \bar{p}_6 , of $9.65 \text{ m}^3/\text{s}$ based on the hydrological balance of the Serio basin, located at the north of the study area. In our analyses, we allow p_6 to vary amongst $0.5 \times \bar{p}_6$ and $1.5 \times \bar{p}_6$. Since a description of the spatial distribution of p_6 is not available, we set the total incoming flow rate as uniformly distributed along the boundary. The range of variability of the Dirichlet boundary condition (p_7) has been defined considering that the river stage may vary between the river bottom (0 m) and the mean elevation of the river banks (approximately equal to 3 m). This datum has been derived from topographic sections of the Adda and Serio rivers (available from Autorità di bacino del fiume Po).

We applied the two global sensitivity analyses briefly described in the following to assess the impact of the uncertainty associated with the selected seven model parameters on the hydraulic head monitored at the 39 observation wells depicted in Figure 2.3. Note that each well is identified by a numeric code (ID) which is associated with a number that increases from North to South to facilitate the interpretation of the results.

2.2.1 Morris Indices

The methodology proposed by Morris (1991) and Campolongo et al. (2007) derives measures of global sensitivity by averaging a set of local derivatives, or elementary effect, evaluated at r selected trajectories of sample points in the parameter space Γ . For a given model, each trajectory requires $N+1$ model runs in which each parameter is perturbed (one at a time) by a fixed increment Δ . The elementary effect of the i -th parameter (EE_i), for a selected trajectory j , is defined as

$$EE_i(j) = \frac{f(p_1, \dots, p_i + \Delta, \dots, p_N) - f(\mathbf{p})}{\Delta} \quad (2.1)$$

where $f(\cdot)$ is the model output. Each trajectory yields one estimate of the elementary effect for each parameter. We evaluate the EE_i for r trajectories to avoid the dependence of the results on the location of the initial point in the parameter space (Campolongo et al. 2007). An estimate of total effect the i -th parameter can be computed from the absolute mean, μ_i^* , of the EE_i over the set of r trajectories

$$\mu_i^* = \frac{1}{r} \sum_{j=1}^r |EE_i(j)| \quad (2.2)$$



If μ^* is substantially different from zero, it indicates that the i -th parameter significantly affects the model output. The advantage of this method relies on the low computational cost associated with the evaluation of sensitivity indices. It requires a number of forward model simulations equal to $r(N+1)$. In our application we obtain stable results with $r = 30$ (i.e. 240 model runs). As drawback, the index μ^* does not give information about the joint effect of parameter uncertainty, as quantified by the Sobol indices described in the next section.

2.2.2 Sobol Indices

Sobol sensitivity analysis is a variance-based method which allows to quantify the uncertainty in the model output due to uncertain parameters and to their interactions (Sobol, 1993, 2001; Sudret, 2007; Formaggia et al. 2013; Dell’Oca et al. 2017). It can be shown that if the model response $f(\mathbf{p})$ belongs to the space of square-integrable functions, then the following expansion holds

$$f(\mathbf{p}) = f_0 + \sum_{i=1}^N f_i(p_i) + \sum_{1 \leq i < j \leq N} f_{ij}(p_i, p_j) + \dots + f_{1, \dots, N}(p_1, \dots, p_N) \quad (2.3)$$

where f_0 is the expected value of $f(\mathbf{p})$ and $f_{i_1, \dots, i_s}(\{i_1, \dots, i_s\} \subseteq \{1, \dots, N\})$ are orthogonal polynomials with respect to a probability measure. The total variance, $V[f]$, of $f(\mathbf{p})$ can then be written as

$$V[f] = \sum_{i=1}^N V_i + \sum_{1 \leq i < j \leq N} V_{ij} + \dots + V_{1, \dots, N} \quad (2.4)$$

Here, V_i is the contribution to the variance of the model output due to the effect of the uncertain input parameter p_i when considered individually, and V_{i_1, \dots, i_s} is due to interaction of the uncertain model parameters belonging to the subset $\{p_{i_1}, \dots, p_{i_s}\}$. The Sobol indices are then defined as

$$S_{i_1, \dots, i_s} = \frac{V_{i_1, \dots, i_s}}{V} \quad (2.5)$$

Sobol indices (2.5) express the contribution of a subset of model parameters $\{p_{i_1}, \dots, p_{i_s}\}$ to the total model variance. One can define $2^N - 1$ Sobol indices from (2.5) such as

$$\sum_{i=1}^N S_i + \sum_{1 \leq i < j \leq N} S_{ij} + \dots + S_{i_1, \dots, i_n} = 1 \quad (2.6)$$



The principal Sobol indices S_i in (2.6) describe the influence of the model parameters i when considered individually and the mixed terms $S_{i,j}$ account for possible interactions between parameters i and j . Total Sobol indices for the i -th parameter are then defined as

$$S_i^T = 1 - \frac{V_{-i}}{V} \quad (2.7)$$

where V_{-i} indicates the fraction of the total variance attributed to all parameters except the i -th.

Sobol indices are evaluated numerically in Section 2.3 through the use of a model-order-reduction technique based on the generalized Polynomial Chaos Expansion (gPCE) approach. This technique consists of approximating $f(\mathbf{p})$ by a linear combination of multivariate Legendre polynomials (Ghanem and Spanos, 1991; Xiu and Karniadakis, 2002; Le Maitre and Knio, 2010). The computational cost of this sensitivity analysis strongly depends on the order of the gPCE. In this work we obtained stable results with a gPCE of order 4 which requires 2437 model runs. The selection of this gPCE has been performed comparing the results obtained employing gPCE of diverse orders (details not shown).

The evaluation of Sobol indices is computationally more demanding than the Morris screening methodology. However, key advantages of this methodology are: (i) it allows to compute the effect of the interaction amongst uncertain parameters, (ii) the series of polynomials theoretically converges to exact results as more and more terms are included and (iii) the reduced model that we obtain together with the Sobol indices evaluation can be effectively used in the context of model calibration, reducing significantly the computational cost associated with model inversion (see e.g. Laloy et al., 2013; Colombo et al., 2017).

2.3 Results and discussion

2.3.1 Probabilistic facies reconstruction

Volumetric percentages of the five facies associated with the model domain are listed in Table 2.1. Figure 2.4 depicts a planar view of the model with boundary conditions and illustrates the distribution of the five facies obtained using the *Composite Medium* approach along three horizontal cross-sections, corresponding to elevation 120 m, 70 m and -30 m a.s.l. One longitudinal (North-South) and two a transverse (East-West) sections of the model are shown in Figure 2.5 with the corresponding patterns of geomaterials and boundary conditions. The reconstructed geomaterial distribution is in good agreement with available geological cross sections of the area (see Figure 2.2 and Annex I). The estimated volumetric percentage of each geological facies obtained considering the *Overlapping Continuum* conceptualization is depicted in Figure 2.6 for a selected layer of the model corresponding to the elevation of 70 m



a.s.l. In this framework the volumetric fraction of a lithofacies can also be interpreted as its probability of occurrence at a given location.

Figure 2.7 displays the average distribution of geomaterials along a longitudinal (South-North) cross section computed using the *Composite Medium* and the *Overlapping Continuum* methodology. Globally, the two approaches lead to similar results. According to the geology of the area, compact and fractured conglomerates (Classes 4 and 5) are mostly detected in the Northern part of the model where fine and silty sand (Class 2) is absent. Clay and silt and gravel (Classes 1 and 3) can be found along the entire longitudinal cross section, being these geomaterials associated with the higher volumetric percentage. As expected, the *Overlapping Continuum* approach leads to a smoother spatial variation of the percentage of geomaterials with respect to the *Composite Medium* methodology.

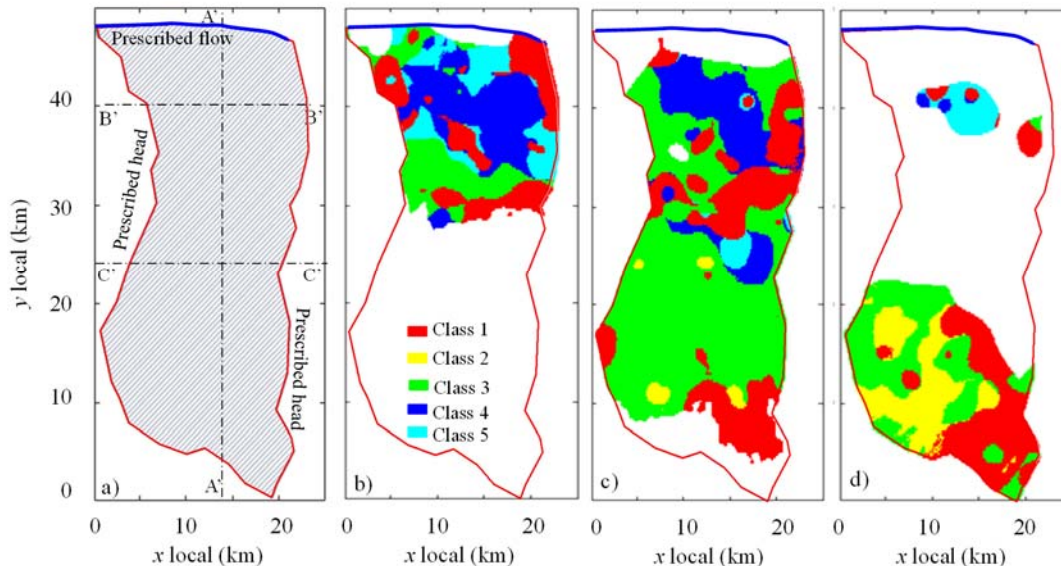


Figure 2.4. Planar view of the model domain. a) Boundary conditions; distribution of the facies in the *Composite Medium approach* within b) layer 30 (i.e., 120 m a.s.l), c) layer 40 (i.e., 70 m a.s.l.) and d) layer 60 (i.e., -30 m a.s.l).

Figure 2.8 displays the log-conductivity field, $Y = \ln K$, reconstructed along a longitudinal cross section and using the three model conceptualizations. The conductivity of the five geomaterials have been set at values consistent with their geological texture, corresponding to the midpoint of their intervals of variability listed in Table 2.2 (i.e. $k_1 = 10^{-7}$ m/s, $k_2 = 10^{-6}$ m/s, $k_3 = 10^{-3}$ m/s, $k_4 = 10^{-5}$ m/s and $k_5 = 10^{-2}$ m/s). In the *Composite Medium* approach (Figure 2.8a) each cell of the model is associated with a constant hydraulic conductivity value. This leads to a heterogeneous medium where blocks characterized by different conductivity values can be



close (or touch). A smoother K distribution is reconstructed using the *Overlapping Continuum* models. We also observe that the *Overlapping Continuum* model computed with the arithmetic mean (AM, Figure 2.8b) leads to a Y field characterized by higher values than its counterpart computed with the geometric mean (GM, Figure 2.8c). Moreover, the spatial heterogeneity of Y described by AM is significantly smaller than the one reconstructed with GM. The mean of Y field, $\langle Y \rangle$, and its standard deviation, σ_Y , are respectively equal to (i) -6.7 and 1.20 for AM and (ii) -10.5 and 1.63 for GM.

Sample pdfs of Y are depicted in Figures 2.9a, b for AM and in Figures 2.9c, d for GM together with pdfs associated with the *Composite Medium* conceptualization. Gaussian pdfs with $\langle Y \rangle$ and σ_Y equal to that of the samples are also shown. Figure 2.9 highlights that the sample pdf of Y for GM presents a slightly bimodal behavior with tails that decay nearly following a Gaussian pdf. When considering AM, sample pdf of Y is clearly non Gaussian, and it displays a long left tail.

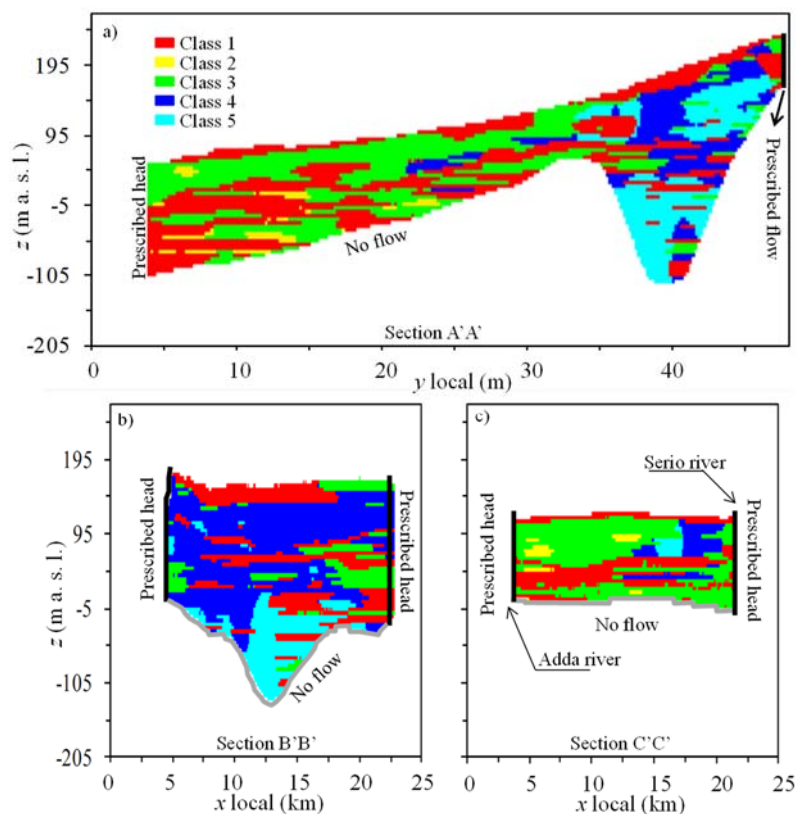


Figure 2.5. *Composite Medium* approach. Facies distribution in Section a) A'A'; b) B'B' and c) C'C'. Boundary conditions are also reported. The location of the vertical cross-sections is displayed in Figure 2.4. Vertical exaggeration factor of 50.

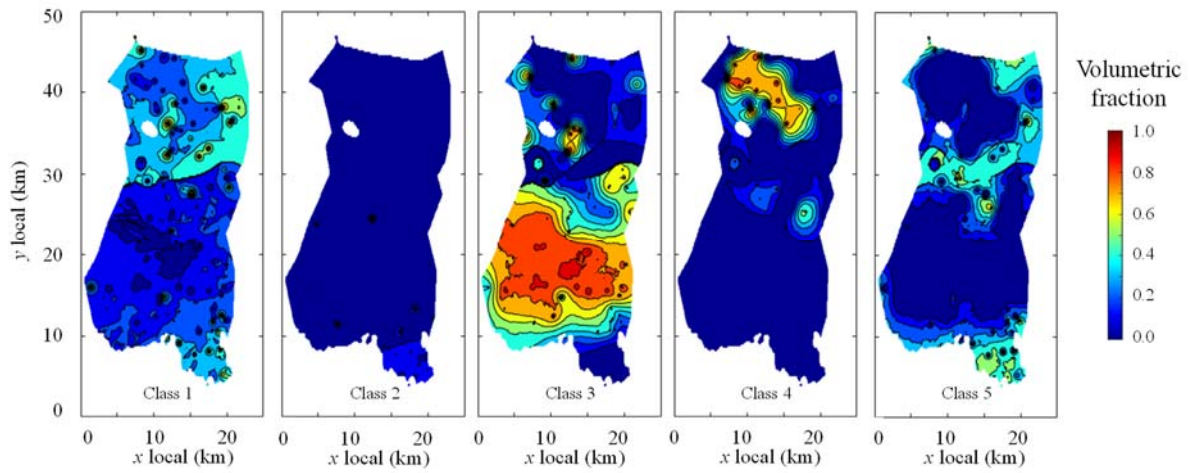


Figure 2.6. *Overlapping Continuum approach*. Volumetric fraction of facies a) 1; b) 2; c) 3; d) 4; and e) 5 within layer 40 (i.e., 70 m a.s.l.).

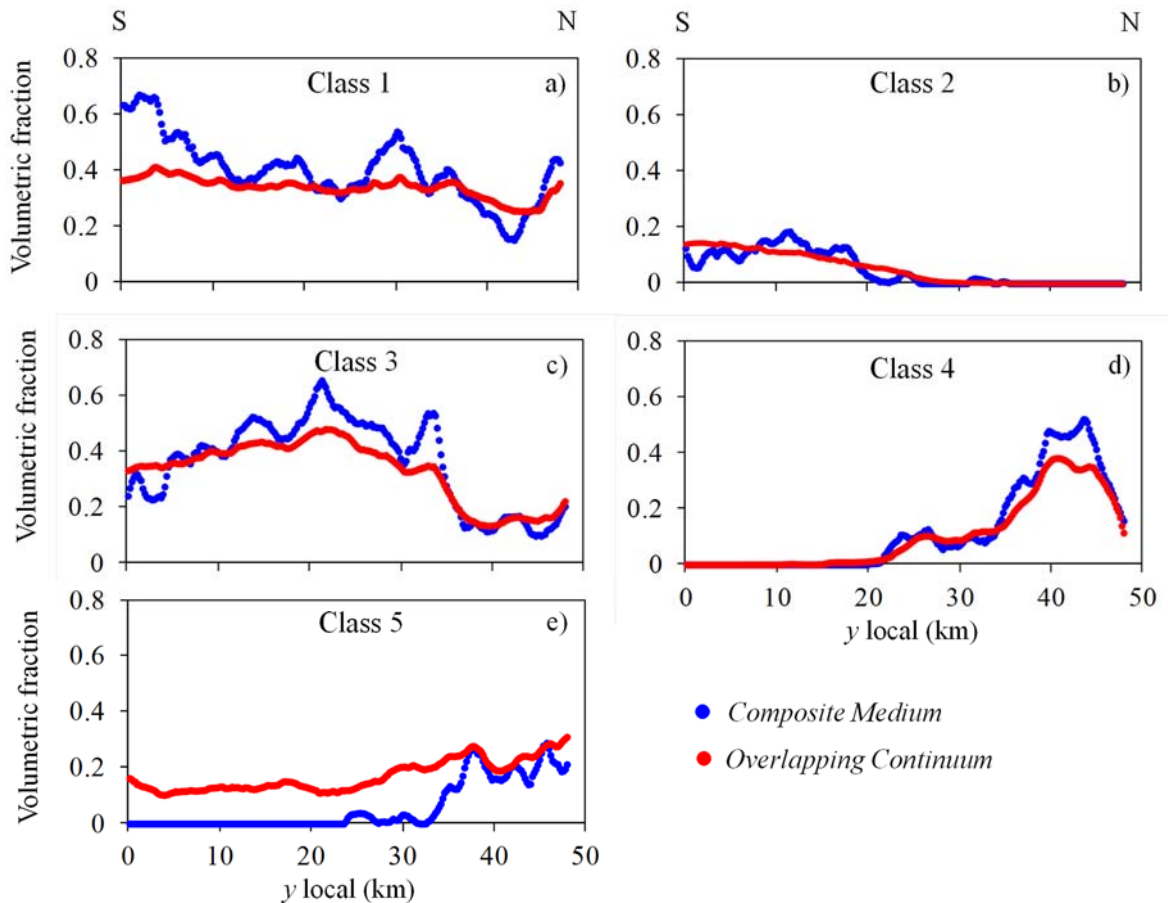


Figure 2.7. Average distribution of geomaterial volumetric fractions along South- North direction for *Composite Medium* and *Overlapping Continuum* approach and facies a) 1; b) 2; c) 3; d) and e) 5.

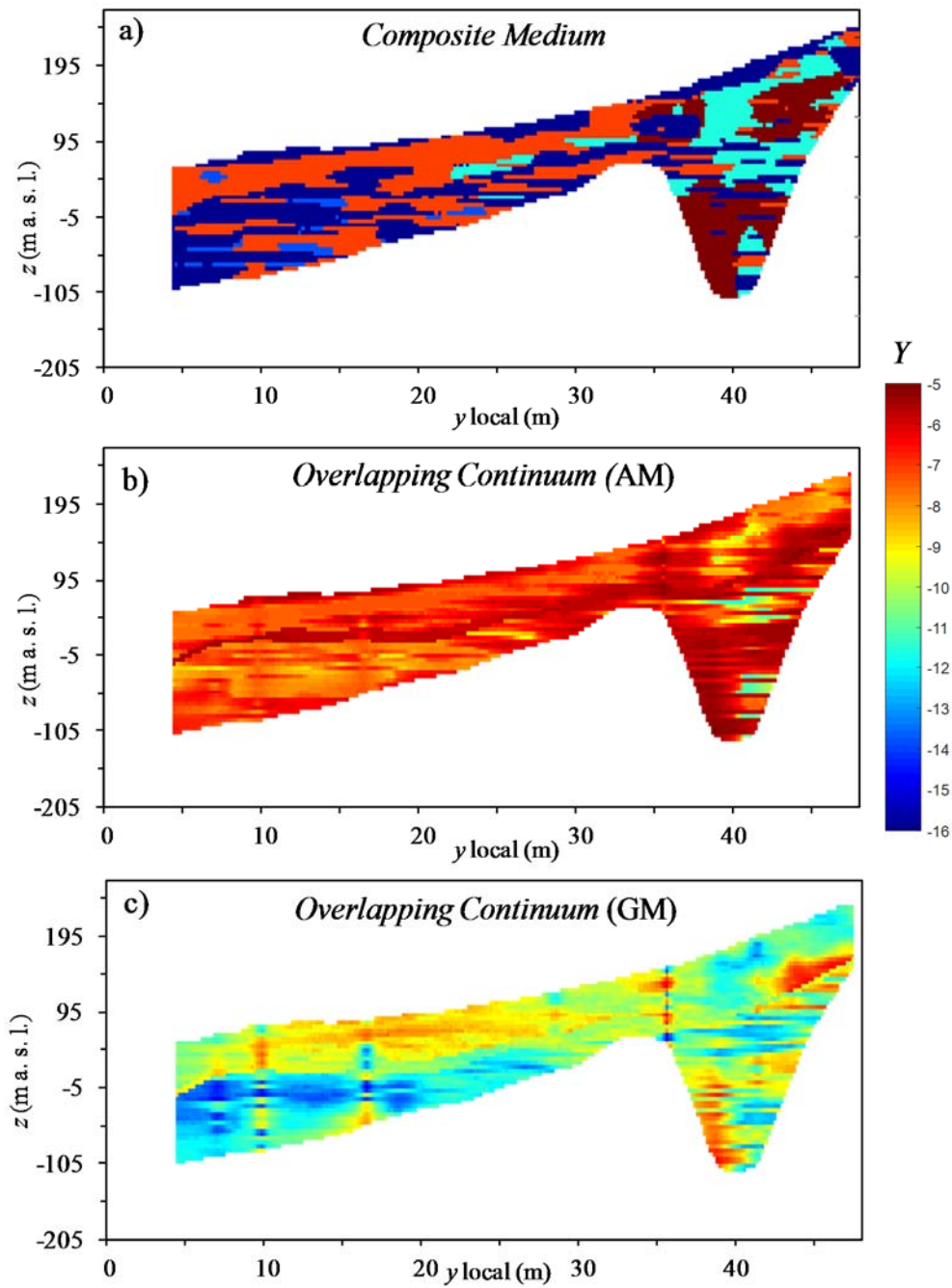


Figure 2.8. Spatial distribution of $Y = \ln K$ along Section A'A' (see Figure 2.4a) for a) *Composite Medium*, b) AM and c) GM. Vertical exaggeration factor of 50.

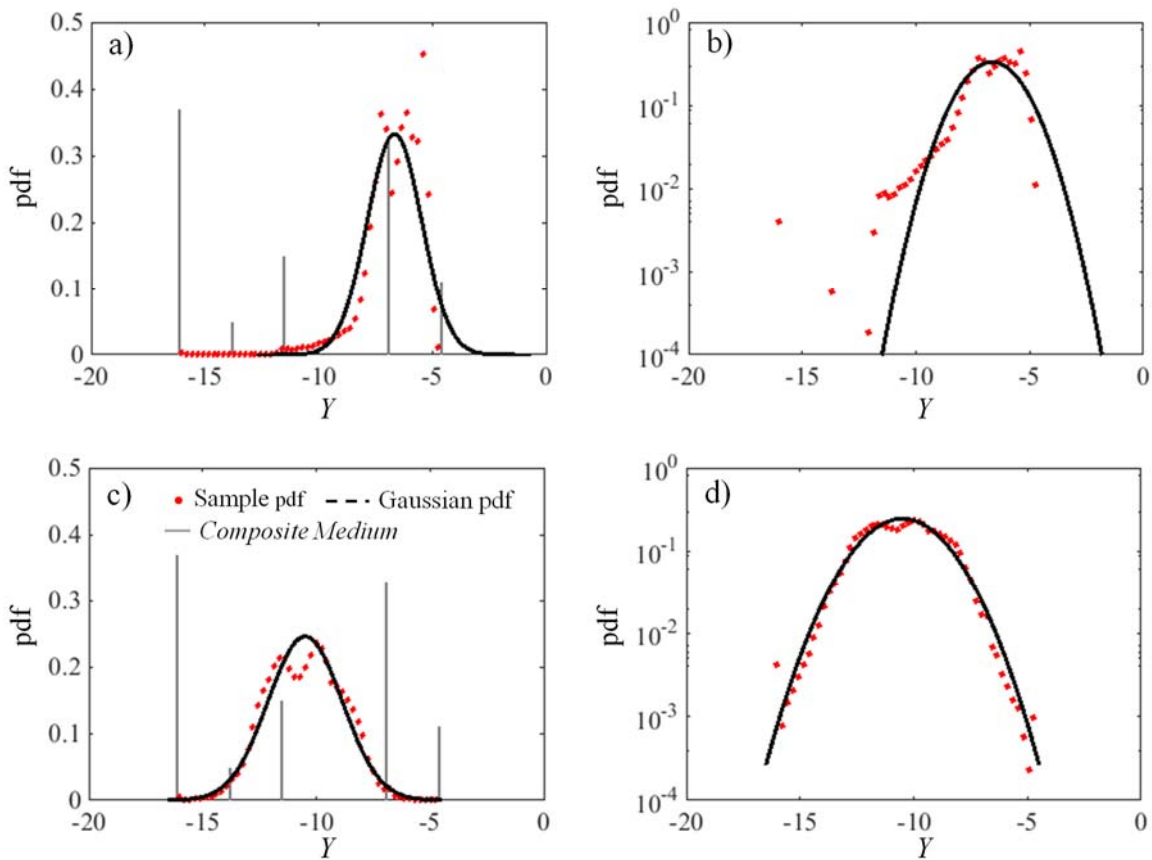


Figure 2.9. Sample pdfs of $Y = \ln K_j$ for AM (a, b) and GM (c, d) on arithmetic (a, c) and semi logarithmic (b, d) scales. Also shown are Gaussian pdfs with mean and variance equal to that of the samples (dashed curves) and the pdfs Y associated with the *Composite Medium* model.

2.3.2 Sensitivity analysis

Figure 2.10 depicts the average hydraulic head, normalized by the corresponding observed head, evaluated at the 39 observation wells (see Figure 2.3 for well locations and ID number) using the three model conceptualizations. These plots overlap results respectively associated with the Morris screening methodology (blue squares, corresponding to normalized hydraulic heads averaged over 240 model runs) and with the Sobol indices evaluations (red dots, corresponding to normalized hydraulic heads averaged over 2437 model runs). Uncertainty intervals equal to ± 2 standard deviations around the mean are also shown with blue and red dashed lines for the Morris and Sobol indices, respectively. The width of uncertainty intervals decreases with increasing the number of model evaluations. Wells located in the Northern area are generally associated with a larger uncertainty, respect to observation in the Southern zone.



Figure 2.11 depicts the sensitivity indices associated with the 7 uncertain parameters for *Composite Medium* approach. We plot (i) the dimensional Morris measure μ_i^* (Figure 2.11a), with $i = 1, \dots, N = 7$; (ii) the normalized Morris measure (Figure 2.11b) defined as $\bar{\mu}_i^* = \mu_i^* / \sum_{i=1}^N \mu_i^*$ and (iii) the total Sobol indices S_i^T (Figure 2.11c). Corresponding results for AM and GM are reported in Figure 2.12 and 2.13, respectively.

For all the conceptual models analyzed, the Northern area is the one that is most sensitive to the variability of the uncertain parameters (Figures 2.11a, 2.12a and 2.13a). In this area GM conceptualization is characterized by higher values of hydraulic heads and higher variation due to uncertainty of input parameters. This result is associated with the combined effect of the model boundary conditions and to the fact that GM is characterized by low Y values, with respect to the other schemes (see Figure 2.8).

Both Morris and Sobol indices identify consistent ranking of model parameters (see Figures 2.11b,c, 2.12b,c and 2.13b,c). The Morris indices, based on a relatively small number of model runs, are able to isolate the most sensitive parameters. Sobol indices also allow identifying the impact of the interaction among parameters on the total output variance. This effect is relevant when $\sum_{i=1}^N S_i^T > 1$. In our case the latter condition is satisfied only at a very limited number of points for all the considered model conceptualizations (Figure 2.11c, 2.12c and 2.13c) showing that the output variance is mainly influenced by the effect of the parameters by themselves and it is weakly affected by parameter interactions.

Focusing on the effect of geomaterial conductivities we observe that model outcomes are not significantly affected by the hydraulic conductivity of sand (k_2) and compact conglomerate (k_4) for all the considered observation points. This result is consistent with the observation that these geomaterials constitute respectively 5% and 15 % of the system. Conductivities of gravel (k_3) and fractured conglomerate (k_5) affect the distributions of hydraulic heads in the aquifer for all the considered conceptual models and most of the observation points. This results can be related to the fact that these two geomaterials are associated with the higher values of hydraulic conductivities. The effect of k_5 is negligible only for the *Composite Medium* model at some Southern location of the aquifer where this material is (practically) absent (see Figure 2.4c and Annex I). The uncertainty associated with clay conductivity (k_1) significantly affect model outcomes for *Composite Medium* and GM (Figures 2.11 and 2.13) while does not affect hydraulic head distribution in AM (Figure 2.12) despite its high volumetric percentage (37%). This result can be interpreted considering that the arithmetic mean tends to reduce the importance of the low conductivity facies (e.g. clay) while enhance the effect of high permeability textures. This effect can be appreciated also by looking at the log conductivity fields displayed in Figure 2.8b.



Considering the boundary conditions note that the parameter associated with Neumann boundary conditions, the Northern total flow rate (p_6), affects only the Northern sector of the aquifer system for *Composite Medium* and AM approaches. The uncertainty associated with this boundary condition produces higher variations of hydraulic heads within GM. This result is associated with the combined effect of the boundary conditions applied to the model and to the fact that the latter approach is characterized by low Y values. The River-stage boundary conditions, p_7 , affects the hydraulic head significantly (in particular in the Southern sector of the study area) for *Composite Medium* and AM. Note that for the *Composite Medium* case, at some observation points very close to the rivers (e.g. 31, 34, 37 and 38) Morris indices tend to underestimate the effect of this boundary conditions. On the other hand, p_7 does not affect model outcomes significantly for GM, except at some locations very close to the rivers (e.g. points 24, 34, 37 and 38).

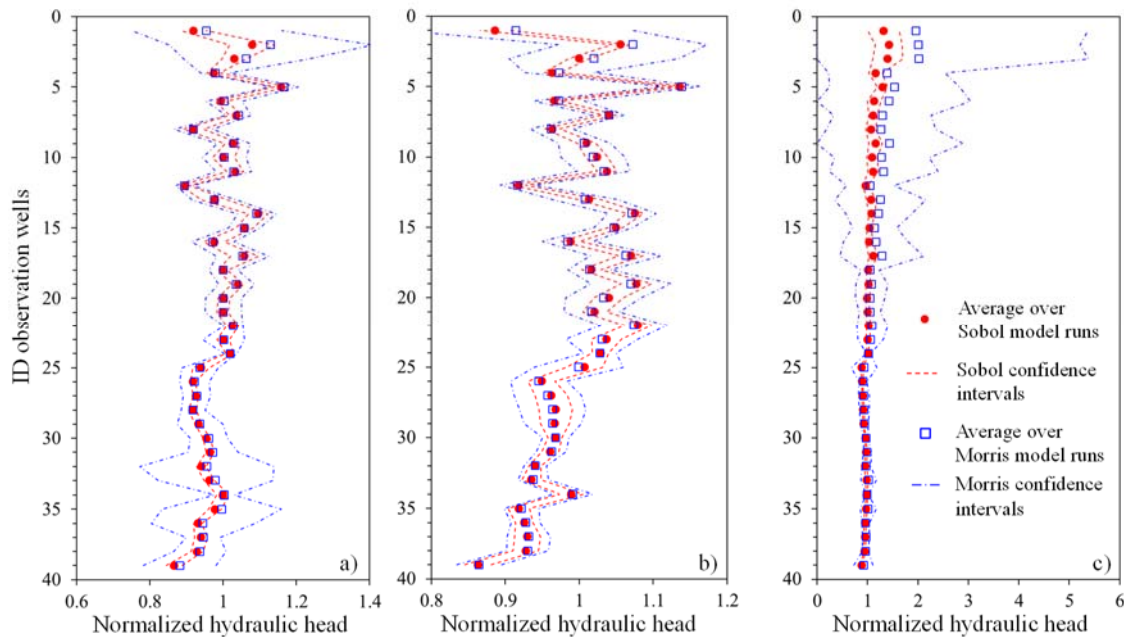


Figure 2.10. Average hydraulic head, normalized by the corresponding observed value, obtained from model runs performed for computing Morris (blue squares) and Sobol (red dots) indices at the 39 observation wells for a) *Composite Medium*, b) AM and c) GM. Uncertainty intervals equal to ± 2 standard deviations around the mean are also shown (dashed curves).

A global comparison of Morris and total Sobol sensitivity indices, for the three model conceptualizations are presented in Figure 2.14a and b, respectively where we depict the average value of scaled Morris, $\langle \bar{\mu}_i^* \rangle$, and total Sobol indices, $\langle S_i^T \rangle$, over the 39 hydraulic head observation points. Error bars in the figure represent ± 1 standard deviation around mean



values. Considering the average response of the three models we note that the two sensitivity measures display consistent trends. When looking at this mean behavior, outcomes of all three model conceptualizations are not significantly affected by the uncertainty of fine sand and compact conglomerate conductivities (k_2 and k_4). Additionally, the response of AM is also not affected by the variability of clay conductivity (k_1). Dirichlet and Neumann boundary conditions, hydraulic conductivities k_3 and k_5 related respectively to gravel and fractured conglomerates affect the computed hydraulic head distribution for all the conceptual models analyzed.

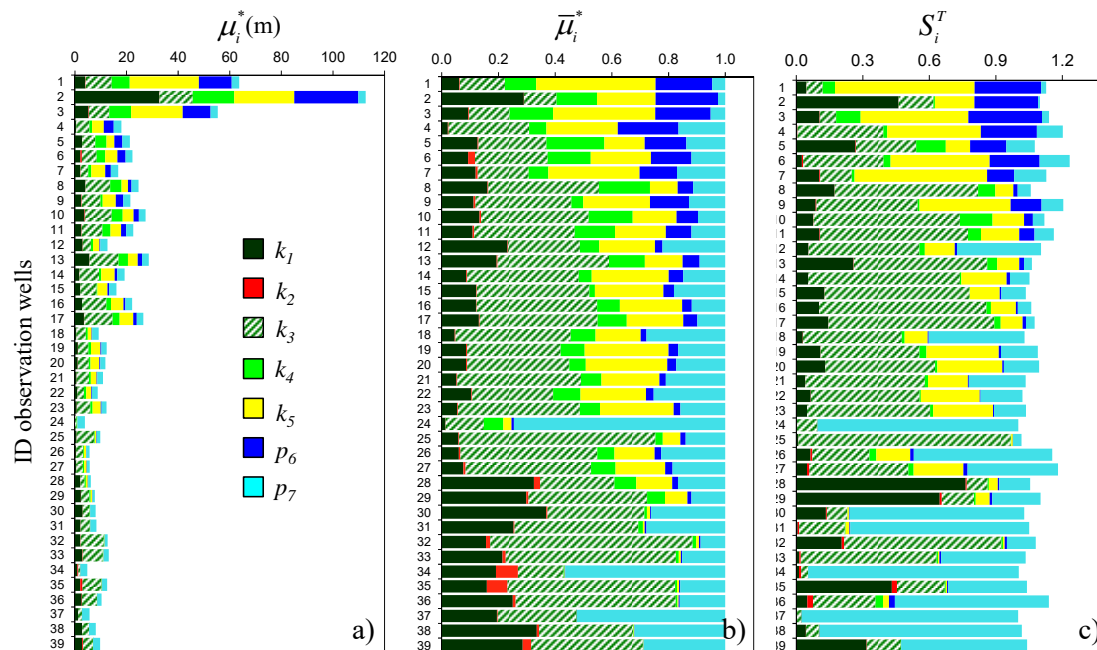


Figure 2.11. *Composite Medium* approach. a) Morris index μ_i^* ; b) Morris scaled index $\bar{\mu}_i^*$ and c) total Sobol index S_i^T for 39 observation wells.

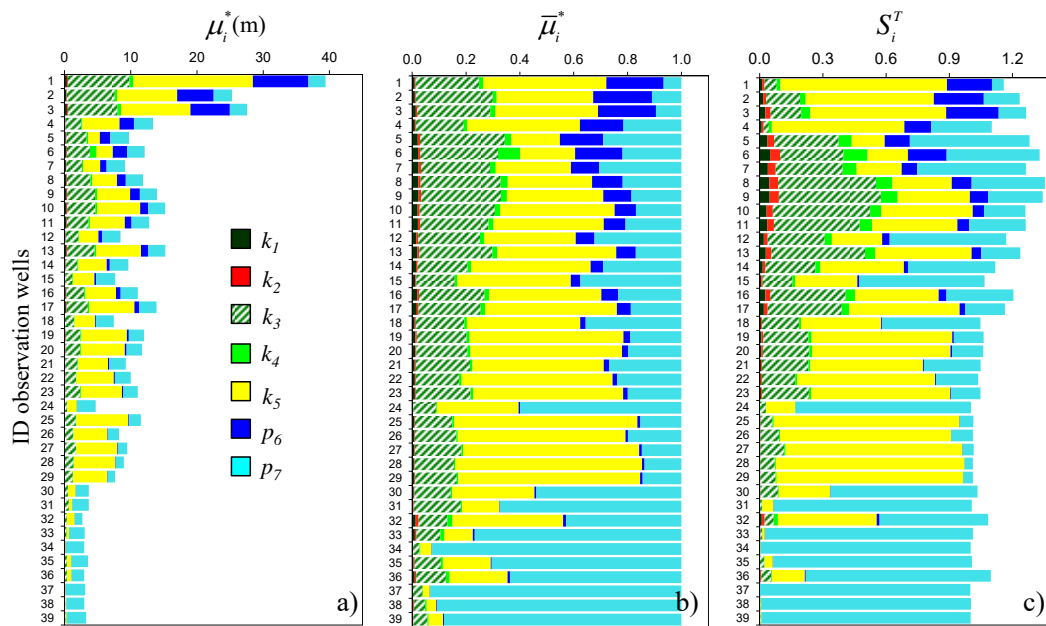


Figure 2.12. *Overlapping Continuum approach, AM.* a) Morris index μ_i^* ; b) Morris scaled index $\bar{\mu}_i^*$ and c) total Sobol index S_i^T for 39 observation wells.

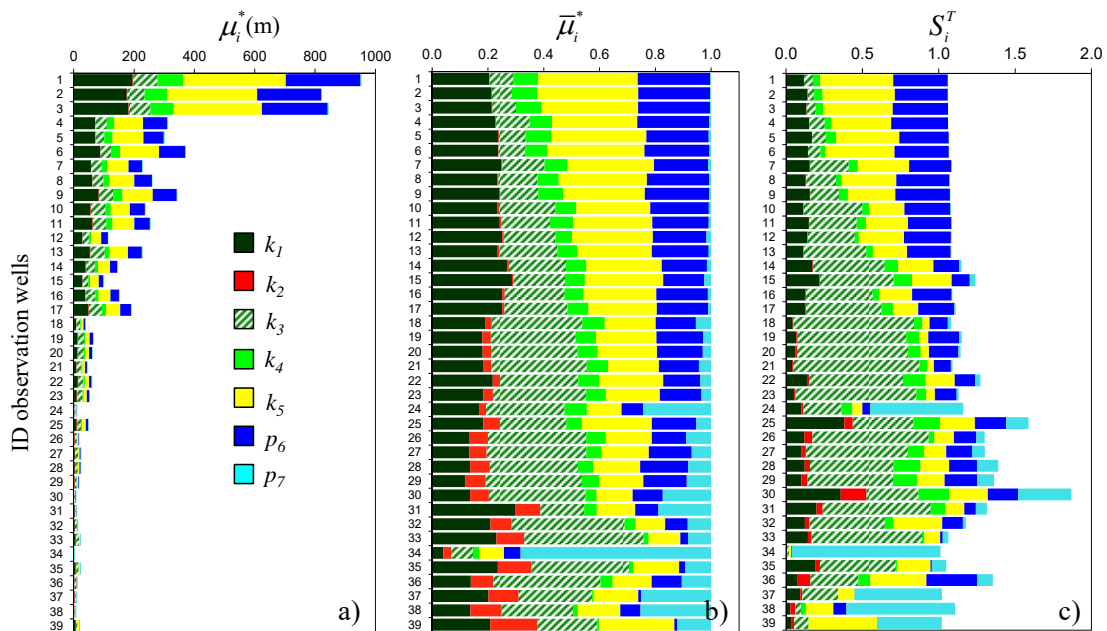


Figure 2.13. *Overlapping Continuum approach, GM.* a) Morris index μ_i^* ; b) Morris scaled index $\bar{\mu}_i^*$ and c) total Sobol index S_i^T for 39 observation wells.

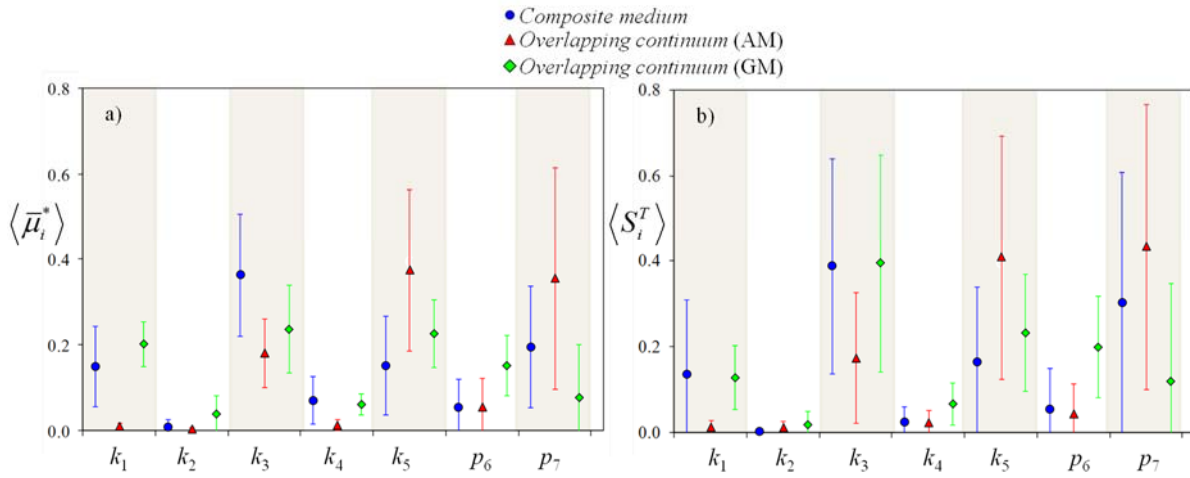


Figure 2.14 Sensitivity indices, averaged over the 39 observation wells. a) Average scaled Morris Index $\langle \bar{\mu}_i^* \rangle$ and b) average total Sobol index $\langle S_i^T \rangle$. Error bars represent ± 1 standard deviation around mean values.

2.4 Model Calibration

2.4.1 Maximum Likelihood Approach

Let N be the number of unknown model parameters and N_h be the number of hydraulic head measurements. We introduce the vector of unknown model parameters, $\mathbf{p} = [p_1, p_2, \dots, p_N]$, the vector of hydraulic head measurements, $\mathbf{h}^* = [h_1^*, h_2^*, \dots, h_{N_h}^*]$, the vector of model predictions, $\hat{\mathbf{h}} = [\hat{h}_1, \hat{h}_2, \dots, \hat{h}_{N_h}]$, and the covariance matrix of the head measurement errors, \mathbf{C}_h . As commonly assumed (e.g., Carrera and Neuman, 1986), we consider errors h_i^* to be uncorrelated. This renders \mathbf{C}_h diagonal with the nonzero terms equal to the head observation error variance, σ_h^2 .

The Maximum Likelihood (ML) estimate, $\hat{\mathbf{p}}$, of \mathbf{p} is obtained by minimizing the negative log likelihood criterion (e.g., Carrera and Neumann, 1986; Bentley, 1993; Poeter and Hill, 1997; Tarantola, 2005; Carrera et al., 2005; Chavent, 2010)

$$NLL = \sum_i^{N_h} \frac{J_i}{\sigma_h^2} + \ln |\mathbf{C}_h| + N_h \ln(2\pi) \quad (2.8)$$

with respect to \mathbf{p} . In Eq. (2.8), J_i is defined as the squared difference between measured and predicted hydraulic heads



$$J_i = (h_i^* - \hat{h}_i)^2 . \quad (2.9)$$

Considering σ_h^2 as a constant minimizing *NLL* (for fixed N_h) is equivalent to the minimization of the least square criterion

$$J = \sum_{i=1}^{N_h} (h_i^* - \hat{h}_i)^2 \quad (2.10)$$

Minimization of Eq. (2.10) is performed using the iterative Levenberg–Marquardt algorithm implemented in the public domain code PEST (Doerthy, 2002). Then, the ML estimate of σ_h^2 is given by

$$\hat{\sigma}_h^2 = \frac{J_{\min}}{N_h} \quad (2.11)$$

where J_{\min} is the minimum of J .

The sensitivity analysis performed in the previous section allows to identify for each model conceptualization the parameters which mainly affect the model outcomes i.e. hydraulic heads. Most influent parameter for each conceptualization have been calibrated using the procedure explained above. According to the results of the sensitivity analysis we calibrate parameters k_1 , k_3 and k_5 for *Composite Medium* and GM models and k_3 , k_5 for AM. For each conceptual model, insensitive parameters and boundary conditions are fixed to values consistent with the geological features of the corresponding classes, as reported in Table 2.5. As calibration data, we consider yearly-averaged hydraulic heads collected at each observation well (i.e., $N_h = 39$) during year 2015 (see Figure 2.3). The observation wells have been included in the numerical model and the measured hydraulic head is associated with the depth of the well screen. When the latter information is not available the piezometric level is associated with the maximum depth of the well.

2.4.2 Model Identification Criteria

When a set of N_M available alternative interpretive models is available, one can use various criteria to (a) rank these models, and/or (b) weigh predictions generated by multiple models (e.g., Akaike, 1974; Schwartz, 1978; Kashyap, 1982; Hurvich and Tsai, 1989; Neuman, 2003; Neuman and Wierenga, 2003; Ye et al., 2004, 2008, Neuman et al., 2011)

$$AIC = NLL + 2N_p , \quad (2.12)$$

$$AIC_c = NLL + 2N_p + \frac{2N_p(N_p + 1)}{N_h - N_p - 1} , \quad (2.13)$$

$$BIC = NLL + N_p \ln(N_h) , \quad (2.14)$$

$$KIC = NLL - N_p \ln(2\pi) - \ln|\mathbf{Q}| . \quad (2.15)$$



Model discrimination criteria allow to discriminate among different competing models on the basis of their quality of fit to observations, number of parameters, and quality of the available data and parameter estimates. Here, \mathbf{Q} is the Cramer-Rao lower-bound approximation for the covariance matrix of the parameter estimates. All of these identification criteria support the principle of parsimony, in the sense that when everything else is equal, one should prefer adoption of the model with the smallest number of parameters. *KIC* balances parsimony with the expected information content by means of $|\mathbf{Q}|$ and favors the model that is least probable (in an average sense) of being incorrect (Ye et al., 2008). On the other hand, Tsai and Li (2008, 2010) and Li and Tsai (2009) suggest that *KIC* can potentially favor models with large parameter estimation uncertainty following unreliable estimation of \mathbf{Q} , potentially leading to controversial results. An extensive discussion of these model selection criteria is presented in Ye et al. (2008, 2010) and Riva et al. (2011).

2.4.3 Hydraulic conductivity estimates

In order to investigate the ability of the three different conceptual models to simulate and predict the physical behavior of the system, we estimate hydraulic conductivity values by means of a ML fit of computed versus measured hydraulic heads adopting the *Composite Medium*, AM and GM models. Dirichlet and Neumann boundary conditions investigated during the sensitivity analysis are fixed to three selected constant values representing the lower bound, medium behavior and upper bound of their range of variability. The considered sets of boundary conditions are listed in Table 2.3.

Parameter short name	p_6	p_7
Parameter description	Total flow rate from Northern boundary	River stage
BC ₁	4.83 m ³ /s	0.0 m
BC ₂	12.06 m ³ /s	1.5 m
BC ₃	19.30 m ³ /s	3.0 m

Table 2.3. Boundary conditions considered during the inversion procedure.

As indicated in Table 2.4, the generalized least squares criterion, J , converges to a smaller value in case of the *Composite Medium* model and BC₂. Model identification criteria tend to favour AM with BC₃ over all remaining models. We argue that in this case the data information content supports a sophisticated scheme of the kind included in the *Overlapping Continuum* model. We note that the arithmetic mean seems to provide a more robust model with respect to the GM approach. Our results suggest that, at the considered scale of interest and on the basis of available data, sharp geological boundaries, adopted in the *Composite Medium*



methodology, play only a secondary role in the system, while local heterogeneities reproduced by the *Overlapping Continuum* approach have a more pronounced controlling effect.

	<i>Composite Medium</i>			<i>Overlapping Continuum AM</i>			<i>Overlapping Continuum GM</i>		
	BC ₁	BC ₂	BC ₃	BC ₁	BC ₂	BC ₃	BC ₁	BC ₂	BC ₃
<i>J</i>	1859	1720	1755	1951	1879	1777	1867	3212	1946
<i>NLL</i>	114.43	114.35	114.36	115.46	115.41	115.35	114.44	114.98	114.49
<i>AIC</i>	120.43	120.35	120.36	119.46	119.41	119.35	120.44	120.98	120.49
<i>AICc</i>	121.11	121.04	121.05	119.80	119.74	119.68	121.13	121.66	121.17
<i>BIC</i>	125.49	125.42	125.43	122.84	122.78	122.72	125.51	126.04	125.55
<i>KIC</i>	119.93	120.25	119.03	118.42	117.53	117.00	114.93	120.06	120.62

Table 2.4. Inversion statistic for the three conceptual models and the considered set of boundary conditions. Minima related to each conceptual model are in black bold, minima amongst all models are in red bold.

Parameter estimates are reported in Table 2.5 for the three conceptual models associated with the smaller KIC value, i.e. *Composite Medium* with BC₃, *Overlapping Continuum AM* with BC₃ and *Overlapping Continuum GM* with BC₁. The estimation error standard deviation, SD, calculated according to the ML methodology, is also reported for the estimated parameters. The estimated values are consistent with the geological features of the classes. For all conceptual models, the lowest value is associated with the clay, silt and fine sand materials, corresponding to Classes 1 and 2, while the largest conductivities are related to gravel material and the fractured conglomerate, corresponding to Classes 3 and 5.

	<i>Composite Medium (BC₃)</i>		<i>Overlapping Continuum AM (BC₃)</i>		<i>Overlapping Continuum GM (BC₁)</i>	
	<i>k</i> (m/s)	SD	<i>k</i> (m/s)	SD	<i>k</i> (m/s)	SD
<i>k</i> ₁	5.79×10 ⁻⁵	4.61×10 ⁻⁵	1.00×10 ⁻⁶	-	2.16×10 ⁻⁶	1.10×10 ⁻⁵
<i>k</i> ₂	1.00×10 ⁻⁴	-	1.00×10 ⁻⁴	-	1.00×10 ⁻⁴	-
<i>k</i> ₃	9.87×10 ⁻³	6.74×10 ⁻³	1.47×10 ⁻²	2.45×10 ⁻²	5.73×10 ⁻²	2.22×10 ⁻²
<i>k</i> ₄	1.00×10 ⁻⁵	-	1.00×10 ⁻⁵	-	1.00×10 ⁻⁵	-
<i>k</i> ₅	4.60×10 ⁻³	2.56×10 ⁻³	5.46×10 ⁻³	6.99×10 ⁻²	6.15×10 ⁻³	4.05×10 ⁻¹

Table 2.5: Parameter estimates and related estimation error standard deviation for the best three conceptual models according to KIC.

Figure 2.15 depicts simulated versus observed hydraulics heads for the three calibrated models.

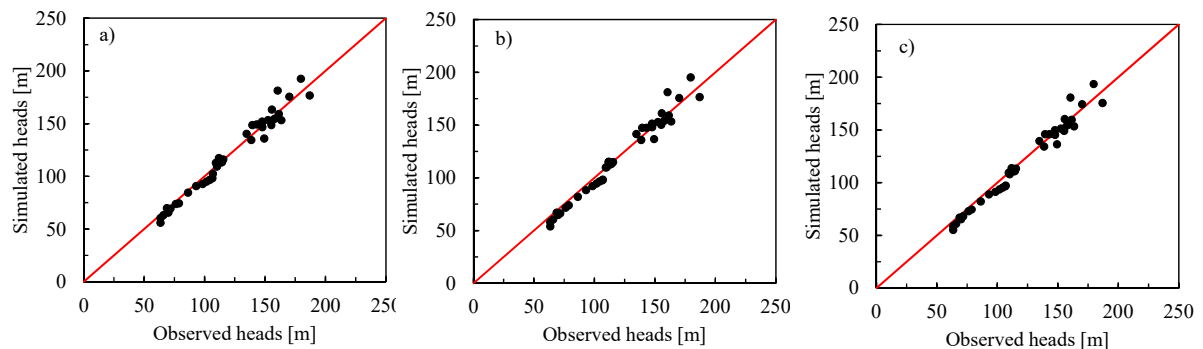


Figure 2.15: Simulated versus observed hydraulic head at monitoring stations. Simulated heads have been obtained with the a) *Composite Medium* scheme and BC_3 , b) AM with BC_3 and c) GM with BC_1 .

2.5 Ongoing and future planned activities

We are currently extending the calibrated model to transient conditions. We are also planning to further improve the site characterization considering transient meteorological, withdrawal, hydrometric and hydraulic head measurements available over the ten-year period 2006-2015. Due to the high computational cost associated with the transient model, we are planning to develop an equivalent two-dimensional system and to solve the transient flow with non-conforming finite elements. The model will be coupled with the surface recharge by means of the Nash transfer function (Chardigny, 1999; Majdalani and Ackerer, 2011). Parameters involved in the diffusivity equation (e.g., conductivity and storativity) as well as the computation of groundwater recharge through the Nash model will be estimated via an inverse ML approach. Due to the high number of parameters involved, we plan to use the adjoint state method (Carrera and Neuman, 1984; Chavent, 1974) to evaluate the gradient of the objective function as well as an approximation of the Hessian of the objective function. The latter is based on a gradient projection method (BFGS, Byrd et al., 1995). Moreover, an adaptive downscaling parameterization (ADP) (Ackerer et al., 2014; Hassane Maina et al., 2017; Hassane Maina and Ackerer, 2017) is envisioned to be used.



3. Bologna site

The Bologna aquifer system is located in the lower part of the Po plain (Emilia Romagna region, Northern Italy). It includes the alluvial fan of the Reno River, the most important hydrographic element within the area. This region is characterized by an intense anthropic activity, drawing its water supplies mainly from the underlying aquifer, resulting in the formation of a cone of depression around the city of Bologna. The extent of this phenomenon can be characterized by the reconstruction of hydraulic head distributions on the basis of available measurements of piezometric levels (see, e.g., Section 3.1.2). As reported in Deliverable 1.1, the system is composed by three aquifer groups (named A, B and C), the former being, in turn, structured into 4 units (A1, A2, A3 and A4). Here, we model the system as an upper confined aquifer (formed by A1 and A2) overlying a lower confined aquifer (formed by A3, A4 and B). Full details about available data, as well as the geological/geomorphological features of the aquifer, are provided in Deliverable 1.1.

3.1 Conceptual and Numerical model

The investigated domain, depicted in Figure 3.1, has a planar surface of about 450 km². It extends over 20×23 km² in the horizontal plane and from -450 m to 100 m a.s.l. along the vertical direction. Along the South-West side, the area is bounded by the Apennines. The system is discretized in 40 × 46 × 100 cells of uniform size of 500 m × 500 m × 5 m.

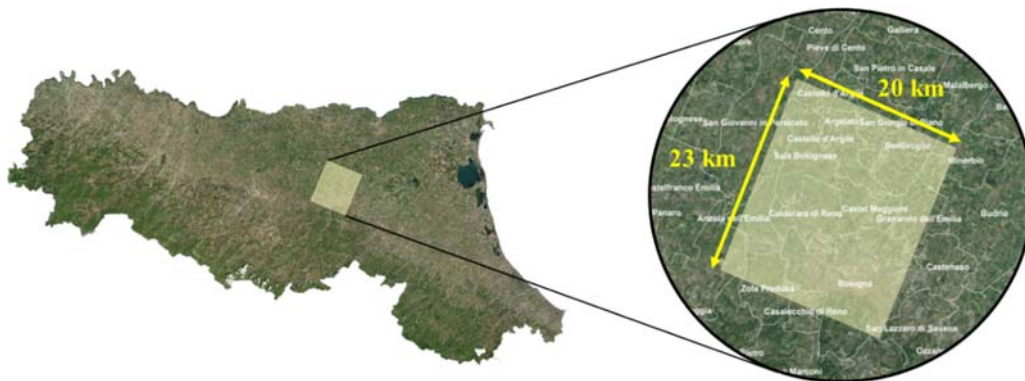


Figure 3.1. Geographical framework of the study area within the Emilia Romagna region.

The data available from stratigraphic information (more than 1300 boreholes, see Figure 3.2) and lithostratigraphic sections allowed to identify 4 main categories (facies/classes or geomaterials) within the area. These categories are listed in Table 3.1, together with their volumetric percentage. Table 3.1 also reports the mean and standard deviation of the extension



of each category along the vertical direction, L_z . It can be noted that clay and gravel are the predominant facies, constituting about the 80% of the whole dataset.

Class	Geological material	Volumetric percentage (%)	Mean of L_z [m]	Standard deviation of L_z [m]
1	Clay	52.1	17.9	15.7
2	Silt and fine sands	13.3	13.1	12.4
3	Medium-to-coarse sands	6.4	10.4	8.9
4	Gravel	28.2	11.7	9.0

Table 3.1. List of geological materials composing the four classes and their volumetric percentage. Mean and standard deviation of the extension along the vertical direction, L_z , of each geomaterial are also reported.

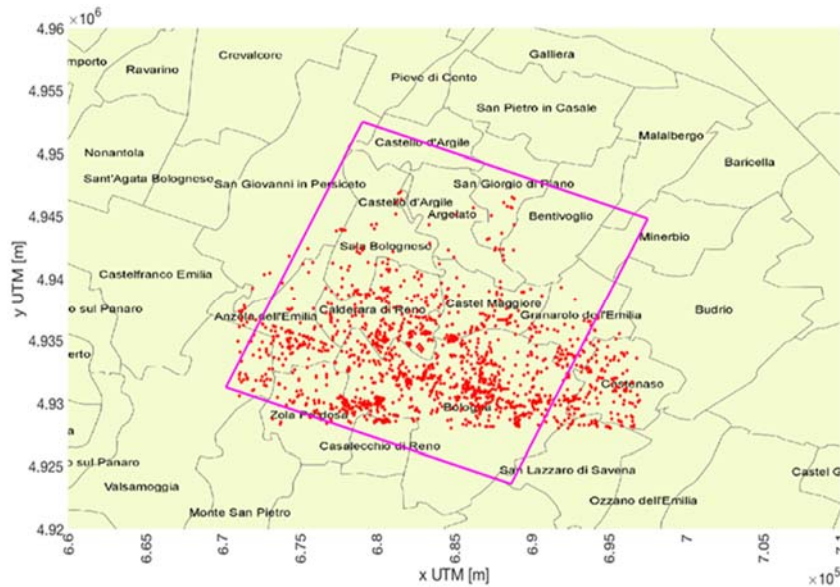


Figure 3.2. Location of the boreholes within the study area.

We conceptualized the Bologna aquifer as a Composite Medium (see Section 2.1.1) where each block of the numerical model is formed by a geomaterial. Here we use two methods for facies reconstruction and we investigate the impact of the adopted approach on the aquifer features. The first method relies on a sequential-indicator approach, (SISIM, Deutsch and Journel, 1992) where a set of Monte Carlo (MC) spatial distributions of facies is generated on the basis of a given set of variograms (one for each category). A second method is based on a transition-probability approach (TPROGS, Carle and Fogg, 1996, 1997). TPROGS realizations are based on (i) the evaluation of the probability of transition between facies and (ii) the interpretation of these probabilities with a Markov-chain model. This approach is compatible



with the generation of non-Gaussian random fields and allows to directly control facies attributes such as volume proportions and mean lengths, as well as the juxtapositional tendencies between them. In the following, key results obtained with the two approaches are compared in a MC framework, by relying on a set of $n = 100$ realizations conditioned on the lithological data.

3.1.1 Probabilistic facies reconstruction: SISIM simulations

We evaluated sample indicator variograms (see Section 2.1.1) of each category from available boreholes lithological data. The sample horizontal and vertical variograms are illustrated in Figure 3.3. Exponential models fitted to the experimental variograms are also reported in the figure and the associated parameters are collected in Table 3.2. It can be noted that the sill of the k -th category, σ_k^2 , (with $k = 1 \dots 4$) does not change with the direction, being related to the volumetric proportion, p_k , according to $\sigma_k^2 = p_k(1 - p_k)$. Parameters listed in table 3.2 have been used for the generation of 100 equally-likely realizations of facies distribution with SISIM. For a qualitative inspection of the results, Figures 3.4a and b depicts, respectively, the top horizontal plane and a vertical cross-section of one SISIM simulation.

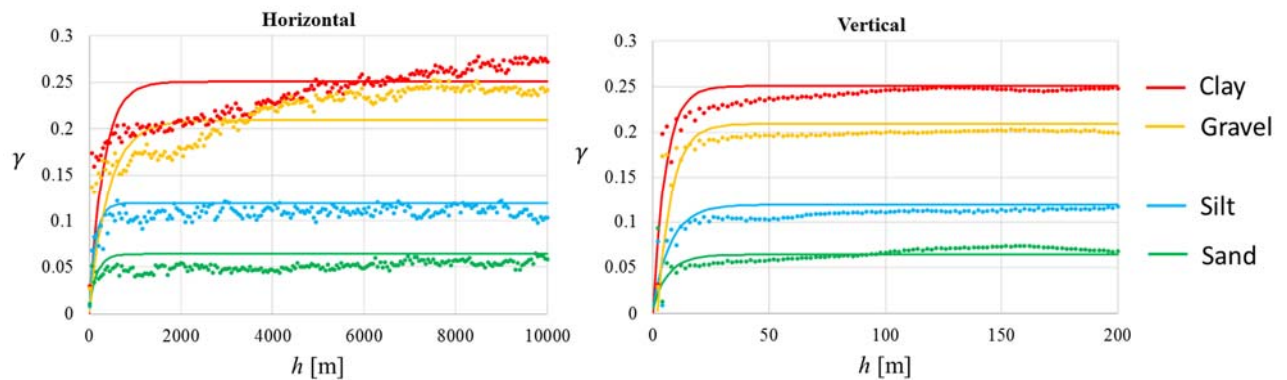


Figure 3.3 Experimental indicator variograms for each facies along the horizontal (left) and vertical (right) direction. Exponential models fitted to the experimental variograms are also reported.



Class	Geological material	Sill	Horizontal range [m]	Vertical range [m]
1	Clay	0.25	915	16
2	Silt and fine sands	0.11	419	23
3	Medium-to-coarse sands	0.06	499	20
4	Gravel	0.21	1270	18

Table 3.2. Exponential model parameters fitting sample indicator variograms.

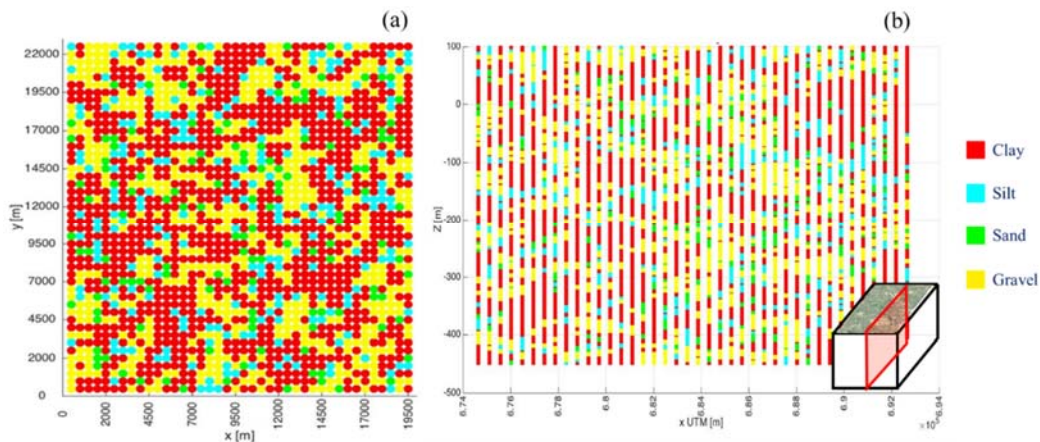


Figure 3.4. Single realization of facies generated with SISIM: (a) top horizontal layer; (b) a vertical cross-section.

3.1.2 Probabilistic facies reconstruction: TPROGS simulations

The transition probability, $t_{jk}(\mathbf{h})$, is defined as:

$$t_{jk}(\mathbf{h}) = \Pr\{k \text{ occurs at } \mathbf{x} + \mathbf{h} \mid j \text{ occurs at } \mathbf{x}\} \quad (3.1)$$

i.e., $t_{jk}(\mathbf{h})$ is the probability of finding category k at the point $\mathbf{x} + \mathbf{h}$ conditional to the presence of category j at point \mathbf{x} . The variation of $t_{jk}(\mathbf{h})$ with the separation distance (or lag) \mathbf{h} is generally called “transiogram” and can be evaluated for all possible pairs of categories (j, k) . At lag $|\mathbf{h}| = 0$, $t_{jk}(0) = 0$ if $j \neq k$ and $t_{jk}(0) = 1$ if $j = k$. Transiograms tend to p_k , i.e., the proportion of the category k , as lag increases. The procedure for the generation of random facies distributions can be summarized as follows:

- 1) Directional experimental transiograms are evaluated on the basis of available lithological data.



- 2) The sample transiograms are interpreted by a Markov-chain model. Model quality criteria are used to select the best transiogram model.
- 3) A sequential procedure is applied to infer the category in each unsampled point. The iteration is similar to the one implemented in SISIM, except for the estimation operator adopted to approximate local conditional probabilities. According to an ordinary kriging estimator (like the one implemented in SISIM) the probability for category k to occur in x_0 is a weighted sum of indicator function of category k , $i_k(x_\alpha)$, available at N locations x_α :

$$\Pr\{k \text{ occurs at } x_0 \mid i_k(x_\alpha); \alpha = 1 \dots N\} \approx \sum_{\alpha=1}^N i_k(x_\alpha) \lambda_{k,\alpha} \quad (3.2)$$

$\lambda_{k,\alpha}$ being the weights of the kriging estimator. TPROGS uses a cokriging estimator, according to which the probability for category k to occur in x_0 is approximated as a weighted sum of indicator functions of all categories, $i_j(x_\alpha)$, with $j = 1, \dots, K$, available at N locations x_α :

$$\Pr\{k \text{ occurs at } x_0 \mid i_j(x_\alpha); \alpha = 1 \dots N; j = 1 \dots K\} \approx \sum_{\alpha=1}^N \sum_{j=1}^K i_j(x_\alpha) w_{jk,\alpha} \quad (3.3)$$

being K the number of categories and $w_{jk,\alpha}$ the weights of the cokriging estimator.

- 4) Facies distribution resulting after the sequential procedure are adjusted cell-by-cell to minimize the discrepancy between the resulting experimental transiograms and the theoretical Markov-chain model inferred from the data.

Sample transiograms obtained from borehole data along directions x and z are collected respectively in Figures 3.5 and 3.6, together with the associated Markov-chain models. Their counterparts evaluated along the y -axis (not reported) are indistinguishable from those reported in Figure 3.5 for the x -axis. An example of facies distributions obtained for one realization at the top horizontal plane and on a vertical cross-section is depicted in Figures 3.7a and 3.7b, respectively. A comparison between the facies distribution obtained with SISIM and TPROGS indicates that the spatial facies arrangement strongly depends on the geostatistical method applied. SISIM allows to reproduce the covariance structure of the conditioning data and tends to generate fields with higher entropy than the TPROGS counterparts. Lee et al. (2007) and Dell'Arciprete et al. (2012) highlighted that covariance-based methods may provide the same degree of heterogeneity inherent with the data, but are not able to capture connected heterogeneity (i.e., the occurrence of channel networks). On the other hand, transition-probability approaches, such as TPROGS, tend to preserve the spatial structure of facies in a way that is consistent with the data. This observation can be gathered not only from the visual inspection of single realizations, but also considering the ensemble behavior of the generated



facies fields. We compute ensemble (i.e., over $n = 100$ MC realizations) indicator variograms and transiograms, considering the facies distributions generated via SISIM and TPROGS. The results for all categories are depicted in Figure 3.8-3.11. It can be noted that (i) all ensemble variograms converge to the theoretical value $\sigma_k^2 = p_k(1 - p_k)$; (ii) for all facies, TPROGS-based ensemble variograms are characterized by larger horizontal and vertical ranges compared to their SISIM counterparts (see Figures 3.8a and 3.8b); (iii) TPROG-based ensemble transiograms (see Figures 3.9-3.10) reach the plateau for larger separation distance respect to SISIM counterparts.

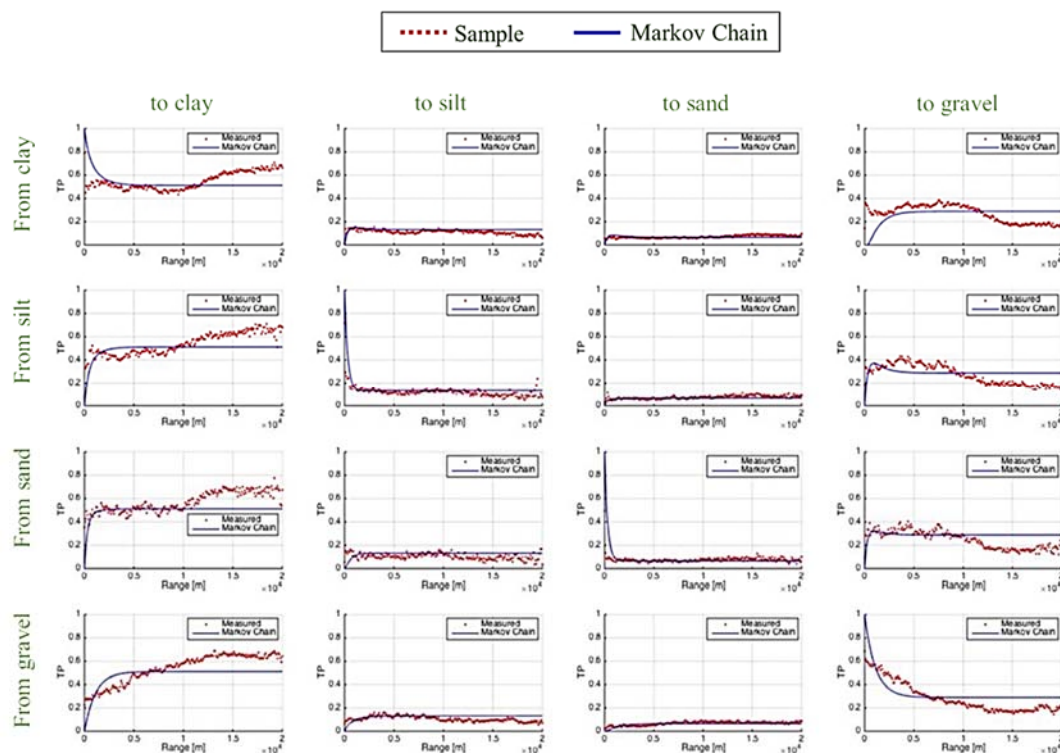


Figure 3.5 Experimental transiograms along the horizontal x -axis. Markov-chain models fitting the sample curves are also reported.

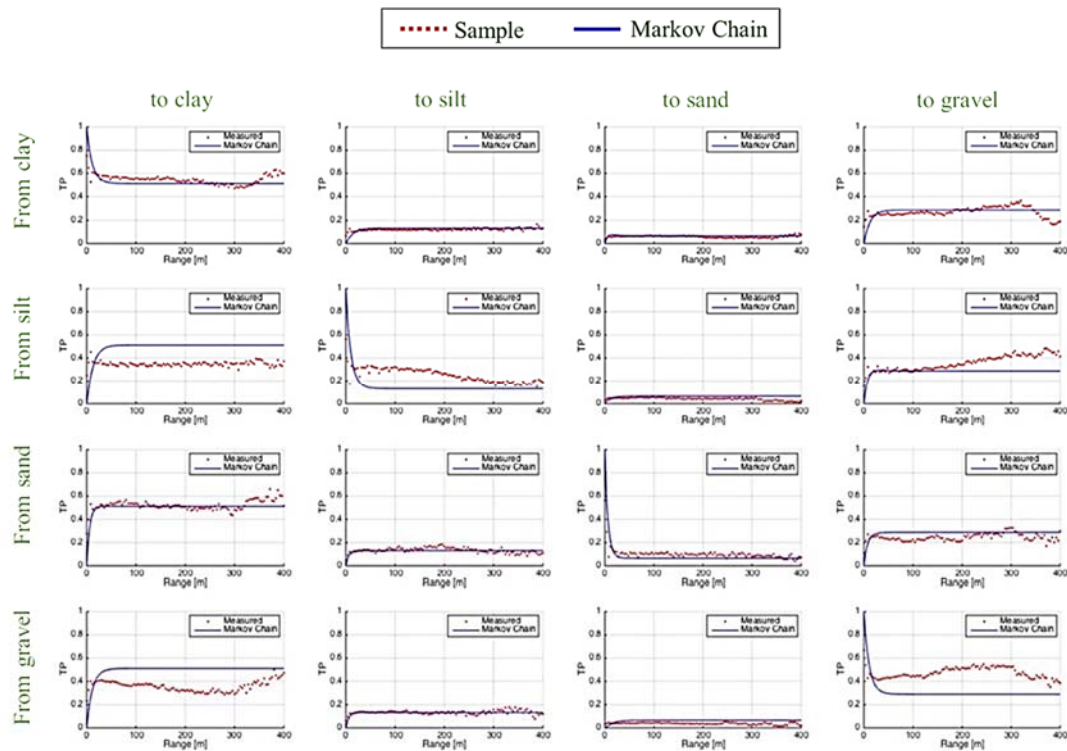


Figure 3.6 Experimental transiograms along the vertical z -axis. Markov-chain models fitting the sample curves are also reported.

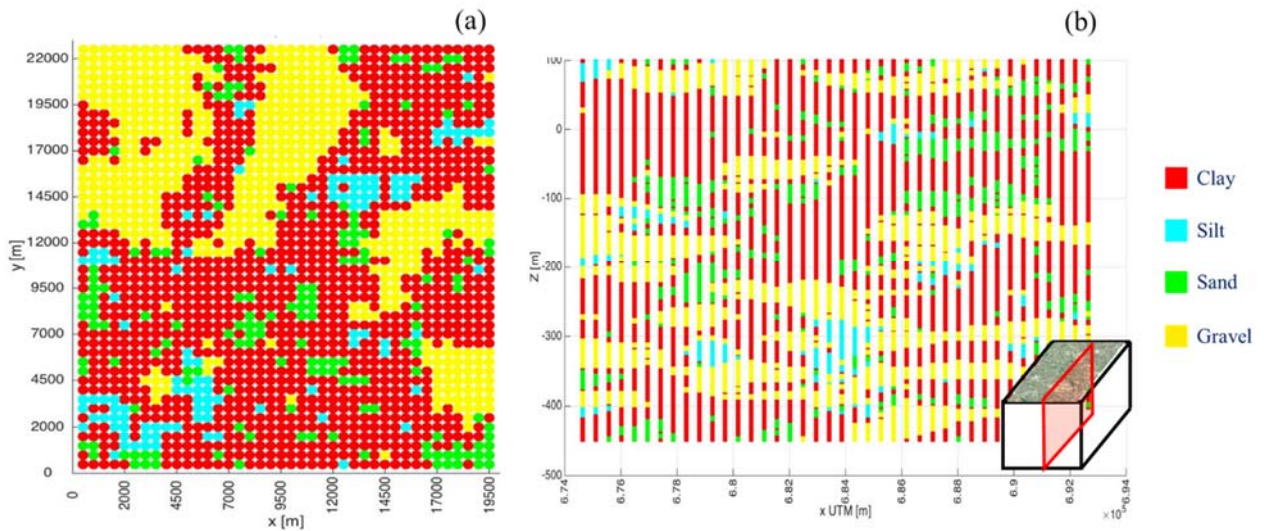


Figure 3.7 Single realization of facies generated with TPROGS: (a) top horizontal layer; (b) a vertical cross-section.

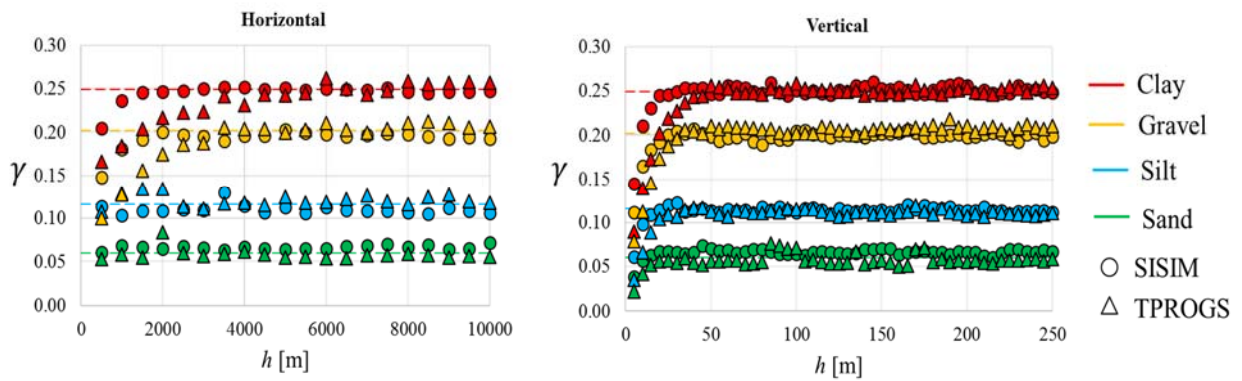


Figure 3.8 Ensemble indicator variograms computed over all SISIM (circles) and TPROGS (triangles) MC realizations along the horizontal (left) and vertical (right) directions.

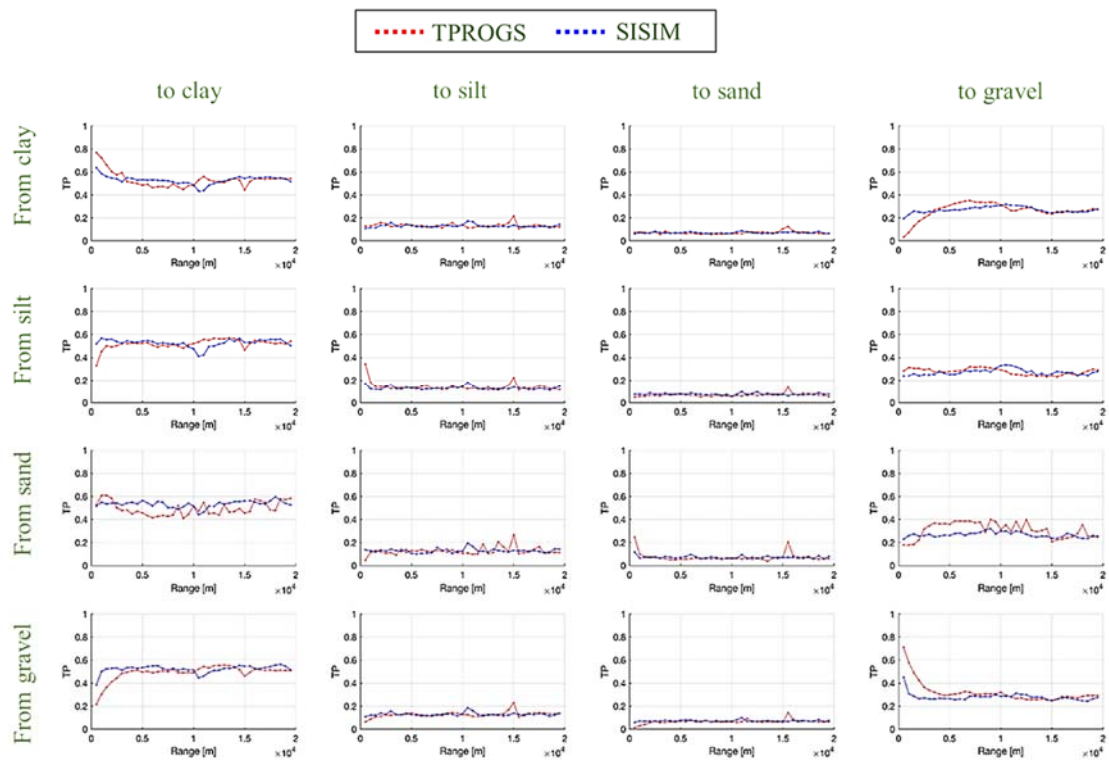


Figure 3.9 Ensemble transiograms along the x -axis obtained over all TPROGS (red) and SISIM (blue) MC realizations.

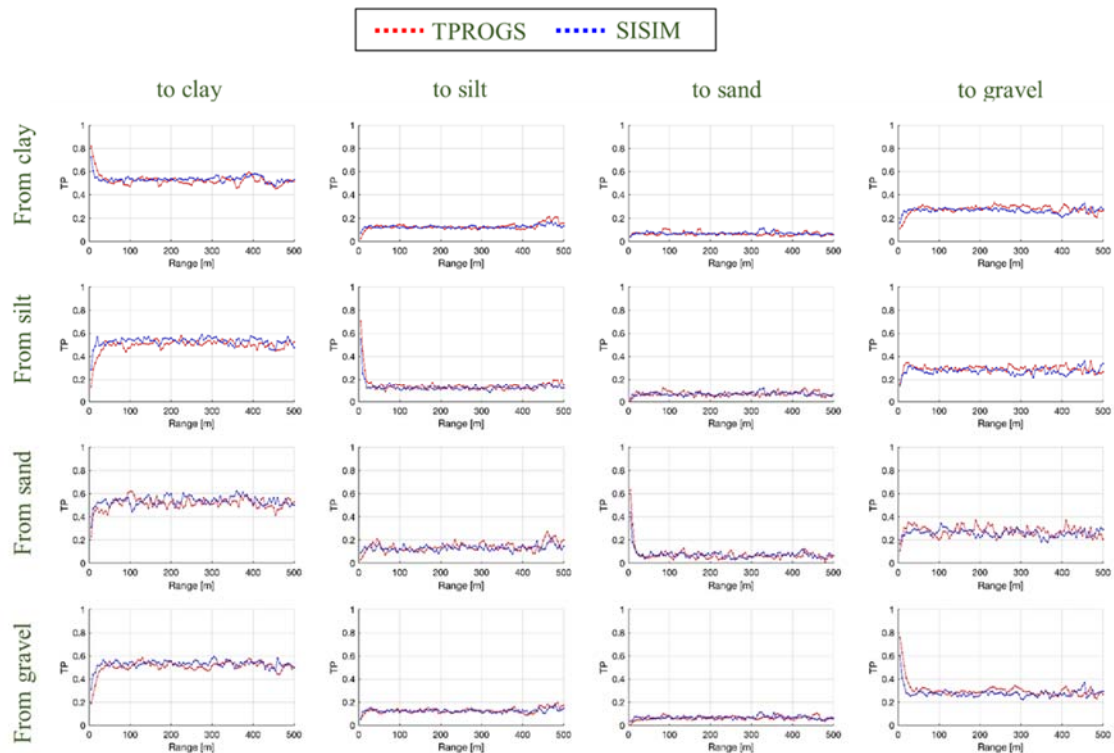


Figure 3.10 Ensemble transiograms along the z -axis obtained over all TPROGS (red) and SISIM (blue) MC realizations.

3.1.2 Groundwater flow model

We considered 50 of the 100 realizations of facies distribution generated with SISIM and with TPROGS. For each generated facies distribution, we developed a steady state, three-dimensional groundwater flow model. The numerical code MODFLOW-2005 (Harbaugh, 2005) is used to simulate groundwater flow. The initial hydraulic conductivity values associated with each facies are *i.e.* $k_1 = 10^{-8}$ m/s, $k_2 = 10^{-6}$ m/s, $k_3 = 10^{-5}$ m/s and $k_4 = 10^{-3}$ m/s respectively for clay, silt, sand and gravel. Figure 3.11 illustrates the actual domain of simulation, together with the adopted boundary conditions. Figure 3.11 also depicts the hydraulic conductivity field obtained for one realization of the SISIM set.

Values of hydraulic head, h , to be set along the boundaries are inferred from the kriged maps of h for both lower (Figure 3.12a) and upper (Figure 3.12b) confined aquifers. These maps have been obtained by interpolating the (detrended) measurements of piezometric levels, averaged over the year 2010, in each unit. As it can be seen from the comparison of Figures 3.12a and 3.12b, the value of h along each column of the boundary is not unique. We impose (i) $h = \text{constant} = h_u$ (*i.e.*, the kriged value for the upper unit) for all cells above the bottom of



the highest pumping rate. In 2010, the total volume of water withdrawal was $4.8 \times 10^7 \text{ m}^3$, for civil (15%), industrial (65%) and agricultural (20%) purposes. Recharge from precipitations has been set according to precipitation and temperature data collected by ARPAE Emilia-Romagna. Measurements are available at 7 stations within our domain, over the time window 2006-2015. The recharge from the Reno River is generally negligible (ARPA Emilia-Romagna 2005, 2008).

3.2 Model Calibration

Hydraulic conductivity values associated with the diverse geomaterials are calibrated in each MC realization on the basis of a Maximum Likelihood approach (see Section 2.4.1). As calibration data we consider yearly-averaged hydraulic heads collected at 20 monitoring wells (see Figure 3.13). A preliminary sensitivity analysis (details not shown) highlights that the model outcomes are not significantly affected by k values associated with the two categories with the smallest volume fraction – i.e., silt (13.3%) and sands (6.4 %). Therefore, reliable estimates of k_2 and k_3 cannot be obtained with the available data and we fix $k_2 = 10^{-6} \text{ m/s}$ and $k_3 = 10^{-5} \text{ m/s}$, corresponding to intermediate characteristic values for the geomaterial considered.

Figures 3.14a and 3.14b show the calibrated conductivity values obtained in all SISIM realizations respectively for clay and gravel. Corresponding results obtained in all TPROGS realizations are depicted in Figures 3.15a-b. The 95% confidence intervals, CIs, of parameter estimates (evaluated on the basis of the posterior covariance matrix \mathbf{Q} , see Section 2.4) are also reported in Figures 3.14 - 3.15. Estimates of k_1 (Figures 3.14a and 3.15a) vary appreciably amongst diverse realizations and are, in general, characterized by not negligible estimation error (quantified by the 95% CIs). On the other hand, estimates of k_4 do not vary significantly amongst the MC realizations and are characterized by relatively small 95% CIs.

In Figures 3.16-3.17 we assess the stability of the MC-based mean $Y = \ln k$, $\langle Y \rangle_n$, for SISIM and TPROGS, respectively. The error in the evaluation of the sample mean scales with $1/\sqrt{n}$, n being the number of MC simulations. Following Ballio and Guadagnini (2004) we can write

$$Pr \left[\langle Y \rangle_n - t_{n-1} \left(1 - \frac{\alpha}{2} \right) \frac{S_n}{\sqrt{n}} \leq \langle Y \rangle \leq \langle Y \rangle_n + t_{n-1} \left(1 - \frac{\alpha}{2} \right) \frac{S_n}{\sqrt{n}} \right] = 1 - \alpha \quad (3.4)$$

where $\langle Y \rangle$ is the ensemble mean of Y , S_n is the sample standard deviation of Y (computed on the basis of n realizations), t_{n-1} is the Student distribution with $(n-1)$ degree of freedom and $1 - \alpha$ is the probability that $\langle Y \rangle$ lies within the confidence intervals, \overline{CI}_s , around the sample



A1; (ii) $h = \text{constant} = h_l$ (i.e., the kriged value for the lower unit) for all cells below the bottom of A3; (iii) a linear variation of h from h_u to h_l with z for all cells between A1 and A3. Figure 3.12 also highlights that the main trend of groundwater flow, directed from the Apennines (South-West) towards the alluvial plain of the Po River (North-East), is superimposed to a large cone of drawdown in the central area, where the major well fields are located.

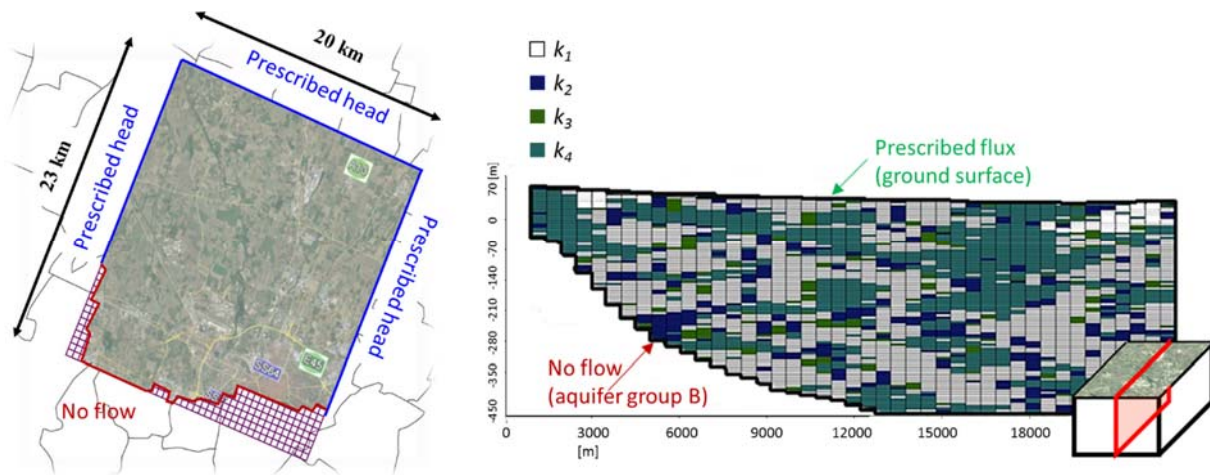


Figure 3.11 Numerical model and boundary conditions. The hydraulic conductivity field across a vertical plane of one SISIM simulation is also depicted.

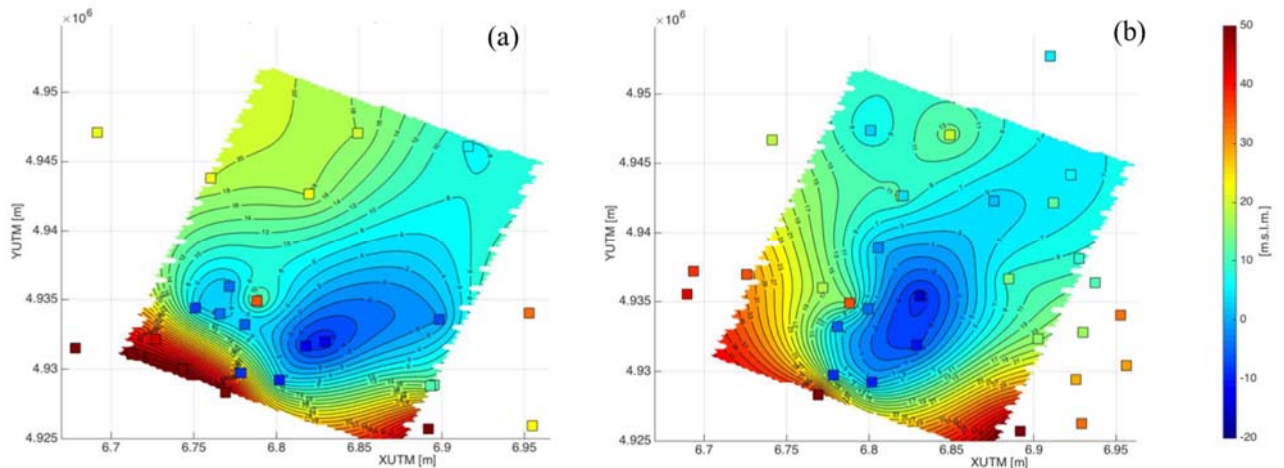


Figure 3.12 Kriged map of hydraulic heads obtained from (detrended) 2010 piezometric data (squares) for (a) lower and (b) upper confined aquifers.

Due to the large number of wells spread throughout the domain, within each municipality the total withdrawal has been concentrated in one point, corresponding to the well location with



mean $\langle Y \rangle_n$. The red dotted lines in Figures 3.16 and 3.17 represent \overline{CI}_s evaluated by setting $\alpha = 0.05$, i.e. the 95% \overline{CI}_s .

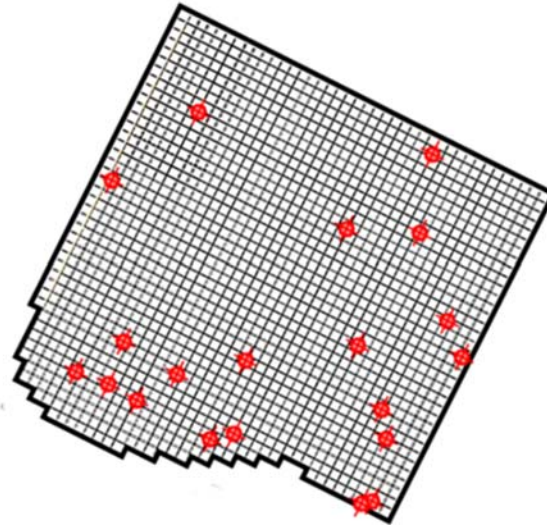


Figure 3.13 Location of the monitoring wells used for model calibration.

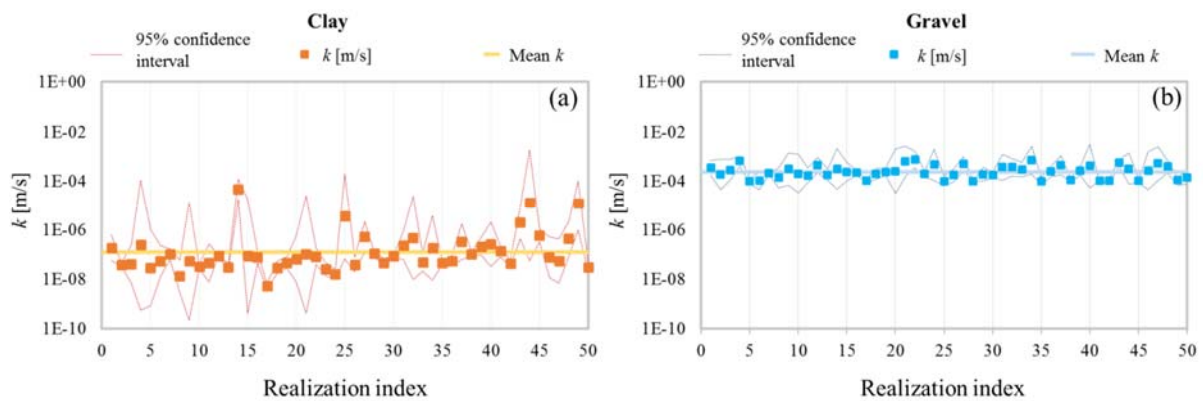


Figure 3.14 Parameter estimates with 95% CIs obtained for 50 SISIM realizations.

Model identification/discrimination criteria (see Section 2.4.2) have been applied to rank, for each method, the facies realizations. Figure 3.18 reports predicted versus measured hydraulic heads at monitoring wells associated with the simulation that minimizes KIC criterion within SISIM (Figure 3.18a) and TPROGS (Figure 3.18b) sets respectively. These plots suggest that the two methods provide calibration results of similar quality, as it is also



indicated by Table 3.3, where the results of model-identification criteria for these two realizations are summarized.

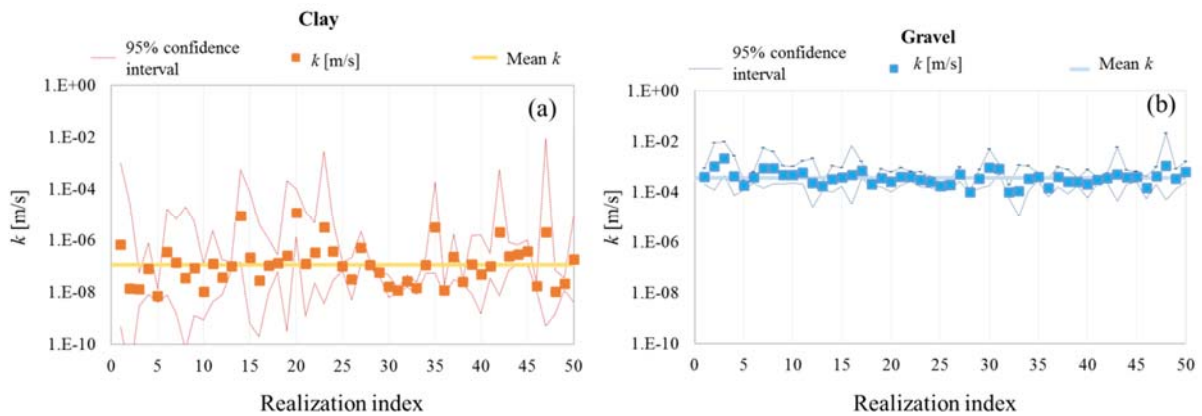


Figure 3.15 Parameter estimates with 95% CIs obtained for 50 TPROGS realizations.

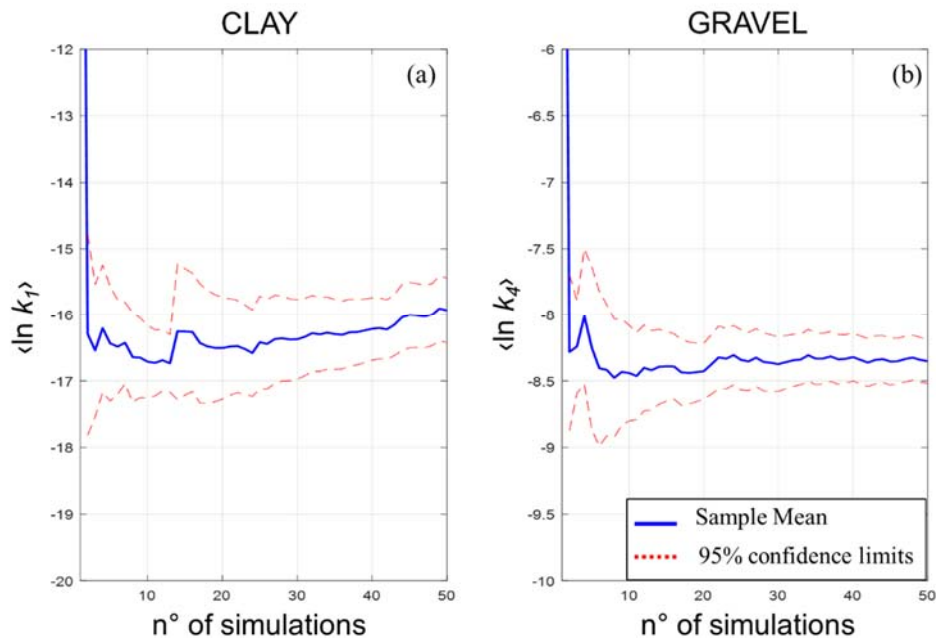


Figure 3.16 SISIM. Mean of $Y = \ln k$ for (a) clay and (b) gravel versus the number of MC simulations. The 95% confidence intervals, \overline{CI}_s , are also reported.

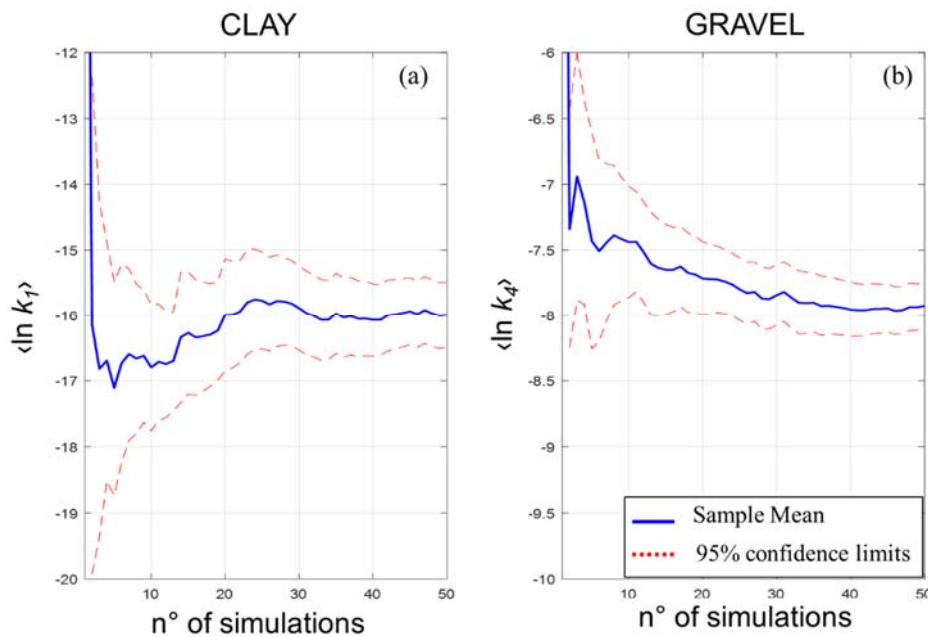


Figure 3.17 TPROGS. Mean of $Y = \ln k$ for (a) clay and (b) gravel versus the number of MC simulations. The 95% confidence intervals, \overline{CI}_s , are also reported.

Model identification/discrimination criteria (see Section 2.4.2) have been applied to rank, for each method, the facies realizations. Figure 3.18 reports predicted versus measured hydraulic heads at monitoring wells associated with the simulation that minimizes KIC criterion within SISIM (Figure 3.18a) and TPROGS (Figure 3.18b) sets respectively. These plots suggest that the two methods provide calibration results of similar quality, as it is also indicated by Table 3.3, collecting the results of model-identification criteria for these two realizations.

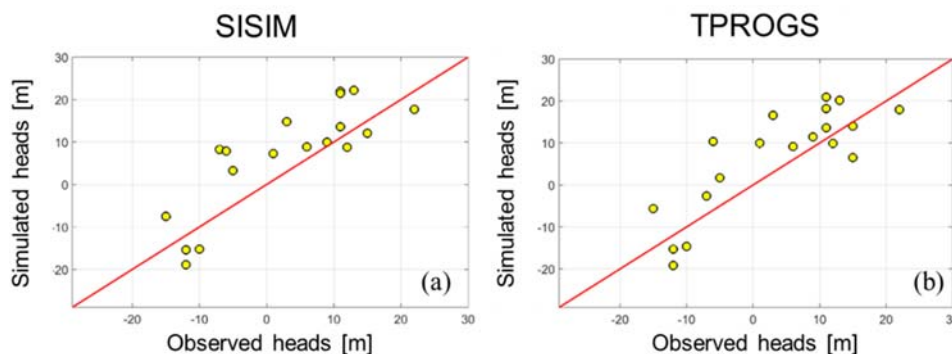


Figure 3.18 Simulated versus observed hydraulic heads for the two realizations minimizing KIC amongst the set of (a) SISIM and (b) TPROGS Monte Carlo simulations.



Criterion	SISIM set	TPROGS set
J	1188	1088
NLL	126	125
KIC	127	133
AIC	130	129
AICc	131	130
BIC	132	131

Table 3.3. Results of model identification criteria for the two realizations minimizing KIC amongst the set of SISIM and TPROGS Monte Carlo simulations.

3.3 Ongoing and future planned activities

Currently, we are performing additional numerical simulations in order to complete the convergence analysis. Moreover, we are planning to (i) extend the analysis within a multi-model approach (ii) analyze connectivity indicators (considering geometrical, flow and transport features) of the reconstructed fields. All these aspects will be crucial for the probabilistic risk assessment of the investigated area.



References

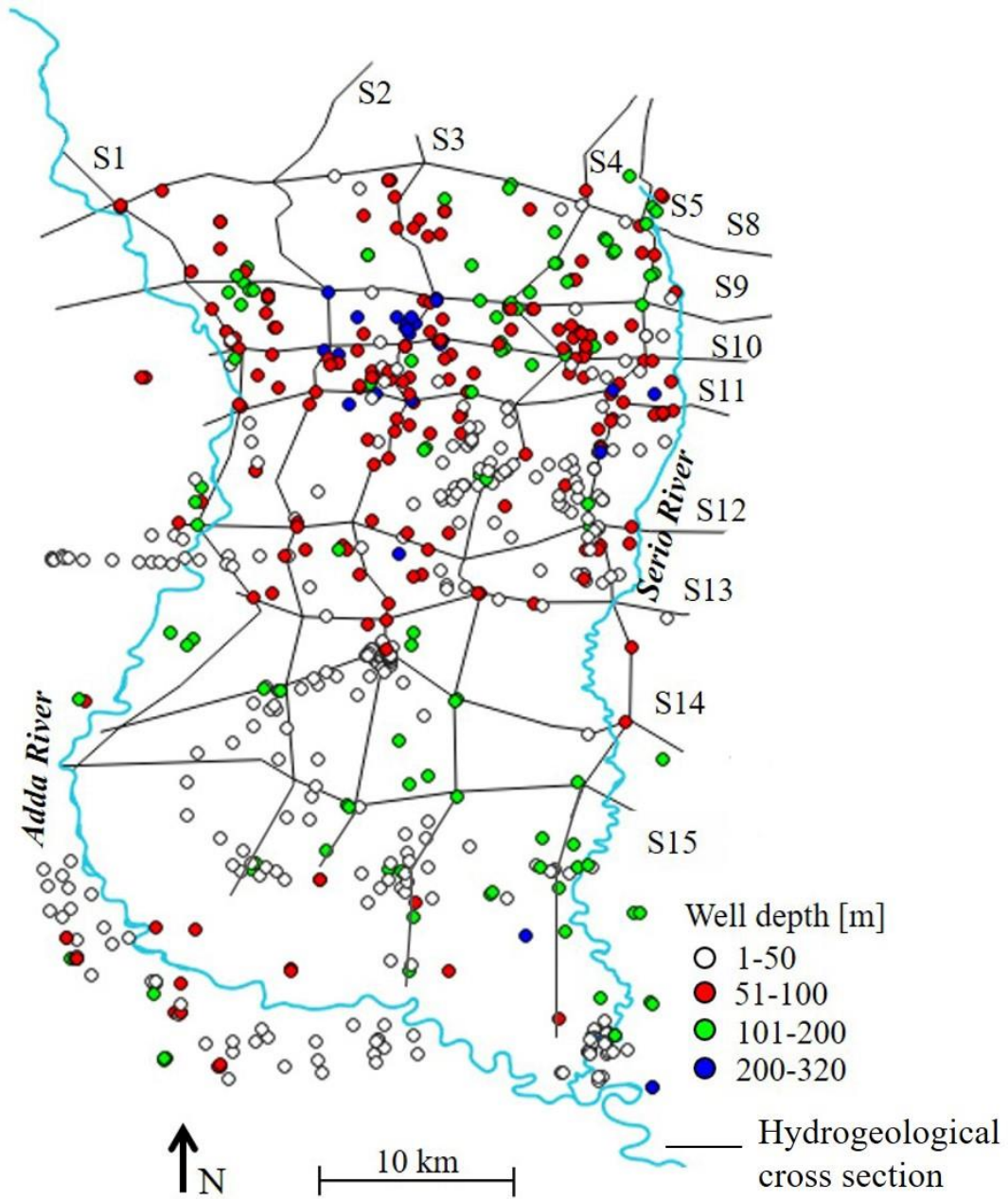
- Ackerer, P., Trotter, N., Delay, F., 2014. Flow in double-porosity aquifers: Parameter estimation using an adaptive multiscale method. *Adv. Water Resour.* 73, 108–122. doi: 10.1016/j.advwatres.2014.07.001.
- Akaike, H., 1974. A new look at statistical model identification. *IEEE T. Automat. Contr.* AC 19, 716–723. doi: 10.1109/TAC.1974.1100705.
- Ballio, F., Guadagnini, A., 2004. Convergence assessment of numerical Monte Carlo simulations in groundwater hydrology. *Water Resour. Res.* 40, W04603. doi: 10.1029/2003WR002876.
- Bentley, L.R., 1993. Least squares solution and calibration of steady state groundwater flow systems. *Adv. Water Resour.* 16, 137–148. doi: 10.1016/0309-1708(93)90004-Y.
- Beretta, G.P., Francani V., Fumagalli L., 1992. Studio Idrogeologico della Provincia di Cremona (Hydrogeological study on Cremona Province), Pitagora Editrice, Bologna.
- Byrd, R., Lu, P., Nocedal, J., Zhu, C., 1995. A Limited Memory Algorithm for Bound Constrained Optimization. *SIAM J. Sci. Comput.* 16, 1190–1208. doi: 10.1137/0916069
- Campolongo, F., Cariboni, J., Saltelli, A., 2007. An effective screening design for sensitivity analysis of large models. *Environ. Model. Softw.* 22, 1509–18. doi: 10.1016/j.envsoft.2006.10.004.
- Carle, S.F., Fogg, G.E. 1996. Transition probability-based indicator geostatistics. *Math. Geol.* 28, 4, 453–477.
- Carle, S. F., Fogg, G.E. 1997. Modelling spatial variability with one and multidimensional continuous-lag Markov chains. *Math. Geol.* 29, 7, 891–918.
- Carrera, J., Neuman, S.P., 1984. Adjoint State Finite Element Estimation of Aquifer Parameters under Steady-State and Transient Conditions, in: Laible, J.P., Brebbia, C.A., Gray, W., Pinder, G. (Eds.), *Finite Elements in Water Resources*. Springer Berlin Heidelberg, pp. 199–211.
- Carrera, J., Neuman, S.P. 1986. Estimation of aquifer parameters under transient and steady state conditions: 1. Maximum likelihood method incorporating prior information. *Water Resour. Res.* 22(2), 199–210. doi: 10.1029/WR022i002p00199.
- Carrera, J., Alcolea, A., Medina, A., Hidalgo, J., Slooten, L.J., 2005. Inverse problem in hydrogeology. *Hydrogeol. J.* 13, 206–222. doi:10.1007/s10040-004-0404-7.
- Chardigny, E., 1999. Modélisation de l'hydrodynamique des eaux souterraines: de la conception du modèle à l'estimation des paramètres par approche inverse (Thèse de doctorat). Université de Strasbourg.
- Chavent, G., 2010. *Nonlinear Least Squares for Inverse Problems*, Scientific Computation. Springer Netherlands, Dordrecht.
- Chavent, G., 1974. Identification of functional parameters in partial differential equations.
- Colombo, I., Porta, G.M., Ruffo, P., Guadagnini, A., 2017. Uncertainty quantification of overpressure buildup through inverse modeling of compaction processes in sedimentary basins. *Hydrogeol. J.* 25 (2), 385–403. doi: 10.1007/s10040-016-1493-9.
- Dell'Arciprete, D., Bersezio, R., Felletti, F., Giudici, M., Comunian, A., Renard, P., 2012. Comparison of three geostatistical methods for hydrofacies simulation: a test on alluvial sediments. *Hydrogeol. J.* 20, 299–311. doi:10.1007/s10040-011-0808-0.
- Dell'Oca, A., Riva, M., Guadagnini, A., 2017. Moment-based Metrics for Global Sensitivity Analysis of Hydrological Systems, *Hydrol. Earth Syst. Sci.*, in press, doi:10.5194/hess-2017-90.
- Deutsch C.V., Journel A.G. GSLIB, 1992. Geostatistical software library and user's guide. New York, Oxford, Oxford university press. doi:10.1016/0098-3004(94)90041-8.
- Doherty, J. 2002. PEST: Model independent parameter estimation, user manual. 4th ed. Watermark Numer. Computing, Corinda, Queensland.
- Ghanem, R.G., Spanos, P.D., 1991. *Stochastic Finite Elements: A Spectral Approach*, Springer, N. Y.
- Formaggia, L., Guadagnini, A., Imperiali, I., Lever, V., Porta, G., Riva, M., Scotti, A., Tamellini, L. 2013. Global Sensitivity Analysis through Polynomial Chaos Expansion of a basin-scale geochemical compaction model, *Computational Geosciences*, 17(1), 25–42, doi 10.1007/s10596-012-9311-5
- Guadagnini, L., Guadagnini, A., Tartakovsky, D.M., 2004. Probabilistic reconstruction of geologic facies. *J. Hydrol.* 294, 57–67. doi: 10.1016/j.jhydrol.2004.02.007.
- Harbaugh, A.W. 2005. MODFLOW-2005, The U.S. Geological Survey Modular Ground-Water Model -the Ground-Water Flow Process. U.S. Geological Survey Techniques and Methods 6-A16.
- Hassane Maina, F., Delay, F., Ackerer, P., 2017. Estimating initial conditions for groundwater flow modeling using an adaptive inverse method. *J. Hydrol.* 552, 52–61. doi: 10.1016/j.jhydrol.2017.06.041.
- Hassane Maina, F., Ackerer, P., 2017. Groundwater flow parameter estimation using refinement and coarsening indicators for adaptive downscaling parameterization. *Adv. Water Resour.* 100, 139–152. doi: 10.1016/j.advwatres.2016.12.013.
- Hurvich, C.M., Tsai C.L. 1989. Regression and time series model selection in small sample. *Biometrika* 76(2), 297–307.
- Isaaks, E.H., Srivastava, R.M., 1990. *An Introduction to Applied Geostatistics*. Oxford Univ. Press, New York.
- Kashyap, R.L. 1982. Optimal choice of AR and MA parts in autoregressive moving average models. *IEEE T. Pattern. Anal.* 4(2), 99–104. doi: 10.1109/TPAMI.1982.4767213.
- Laloy, E., Rogiers, B., Vrugt, J.A., Mallants, D., Jacques, D., 2013. Efficient posterior exploration of a high-dimensional groundwater model from two-stage Markov chain Monte Carlo simulation and polynomial chaos expansion. *Water Resour. Res.* 49, 2664–2682. doi: 10.1002/wrcr.20226.



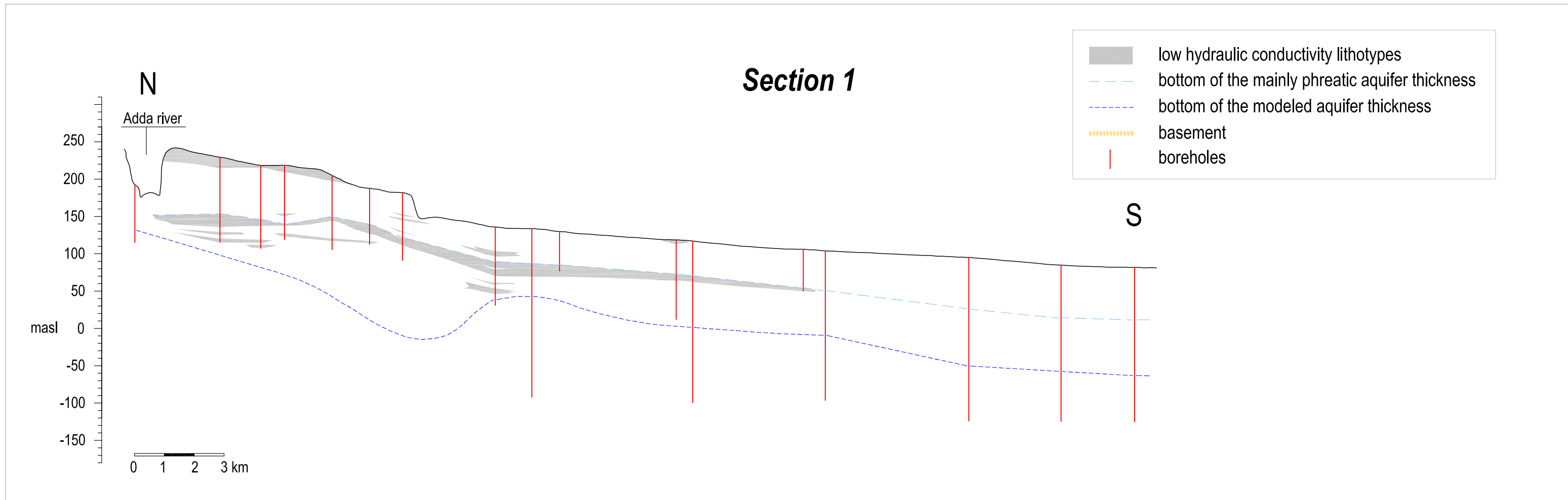
- Le Maitre, O., Knio, O., 2010. Spectral methods for uncertainty quantification. Scientific Computation, Springer, Heidelberg, Germany.
- Lee, S.Y., Carle, S.F., Fogg, G.E., 2007. Geological heterogeneity and comparison of two geostatistical models: sequential Gaussian and transition probability-based geostatistical simulation. *Adv. Water Res.* 30, 1914-1932. doi: 10.1016/j.advwatres.2007.03.005.
- Li, X., Tsai, F.T.C. 2009. Bayesian model averaging for groundwater head prediction and uncertainty analysis using multimodel and multimethod. *Water Resour. Res.* 45, W09403. doi: 10.1029/2008WR007488.
- Maione, U., Paoletti, A. and Grezzi, G., 1991. Studio di gestione coordinata delle acque di superficie e di falda nel territorio compreso fra i fiumi Adda e Oglio e delimitato dalle Prealpi e dalla linea settentrionale di affioramento dei fontanili. (Study on surface and subsurface water management in the area between the Adda and Oglio river, the Prealpi line and the springs line).
- Majdalani, S., Ackerer, P., 2011. Identification of Groundwater Parameters Using an Adaptive Multiscale Method. *Ground Water* 49, 548–559. doi:10.1111/j.1745-6584.2010.00750.x.
- Morris, M.D., 1991. Factorial sampling plans for preliminary computational experiments. *Technometrics* 33, 161–174.
- Neuman, S.P. 2003. Maximum likelihood Bayesian averaging of alternative conceptual-mathematical models. *Stoch. Env. Res. Risk A.* 17(5), 291–305. doi: 10.1007/s00477-003-0151-7.
- Neuman, S.P., Wierenga, P.J. 2003. A comprehensive strategy of hydrogeologic modeling and uncertainty analysis for nuclear facilities and sites. NUREG/CR-6805. U.S. Nuclear Regulatory Commission, Washington, DC.
- Neuman, S.P., Xue, L., Ye, M., Lu, D., 2011. Bayesian analysis of data-worth considering model and parameter uncertainties. *Adv. Water Resour.* 36, 75-85. doi: 10.1016/j.advwatres.2011.02.007.
- Poeter, E.P., Hill, M.C., 1997. Inverse Models: A Necessary Next Step in Ground-Water Modeling. *Ground Water* 35, 250–260. doi:10.1111/j.1745-6584.1997.tb00082.x
- Rametta, D., “Interazione tra reticolo idrografico superficiale e acquifero sotterraneo nella modellistica idrologica distribuita (Study on surface-subsurface water interaction by means of a distribute model)”, Master Thesis, Politecnico di Milano, Milano (2008).
- Regione Emilia Romagna, ENI-AGIP 1998. Riserve idriche sotterranee della Regione Emilia-Romagna, S.EL.CA., Firenze.
- Regione Lombardia, ENI- AGIP 2002. Geologia degli acquiferi padani della Regione Lombardia, S.EL.CA., Firenze.
- Regione Emilia-Romagna, Assessorato agricoltura, ambiente e sviluppo sostenibile – Autorità di bacino del Reno; 2005. Studio della conoide alluvionale del fiume Reno per la realizzazione di un modello idrogeologico per la gestione sostenibile delle risorse idriche. ARPA Emilia-Romagna, sezione provinciale di Bologna.
- Regione Emilia-Romagna, Assessorato agricoltura, ambiente e sviluppo sostenibile; 2008. Approfondimenti sulla conoide alluvionale del fiume Reno, aggiornamento della modellistica e valutazione delle necessità di adeguamento della stessa in base a specifiche esigenze. ARPA Emilia-Romagna, sezione provinciale di Bologna.
- Riva, M., Panzeri, M., Guadagnini, A., Neuman, S. P., 2011. Role of model selection criteria in geostatistical inverse estimation of statistical data- and model-parameters, *Water Resour. Res.*, 47, W07502, doi:10.1029/2011WR010480.
- Schwarz, G. 1978. Estimating the dimension of a model. *Ann. Stat.* 6(2):461–464.
- Sobol, I.M., 1993. Sensitivity estimates for nonlinear mathematical models. *Math. Modeling. Comput.* 1, 407–414.
- Sobol, I. M., 2001. Global sensitivity indices for nonlinear mathematical models and their Monte Carlo estimates. *Math. Comput. Simulat.* 55(1–3), 271–280. doi: 0.1016/S0378-4754(00)00270-6.
- Sudret, B. 2007. Global sensitivity analysis using polynomial chaos expansion. *Reliab. Eng. Syst. Safety* 93(7), 964–979.
- Tarantola, A., 2005. Inverse Problem Theory and Methods for Model Parameter Estimation. SIAM.
- Tsai, F.T.C., Li, X. 2008. Inverse groundwater modeling for hydraulic conductivity estimation using Bayesian model averaging and variance window. *Water Resour. Res.* 44, W09434. doi:10.1029/2007WR006576.
- Tsai, F.T.C., Li, X. 2010. Reply to comment by Ming Ye et al. on “Inverse groundwater modeling for hydraulic conductivity estimation using Bayesian model averaging and variance window”. *Water Resour. Res.* 46, W02802.
- Xiu, D., Karniadakis, G.E., 2002. The Wiener-Askey polynomial chaos for stochastic differential equations. *SIAM J Sci Comput* 24, 614–644. doi:10.1137/S1064827501387826.
- Ye, M., Lu, D., Meyer, P.D., Neuman, S.P., 2010. Comment on “Inverse groundwater modeling for hydraulic conductivity estimation using Bayesian model averaging and variance window” by Frank T.-C. Tsai and Xiaobao Li. *Water Resour. Res.* 46:W02801.
- Ye, M., Meyer, P.D., Neuman, S.P., 2008. On model selection criteria in multimodel analysis. *Water Resour. Res.* 44, W03428. doi: 10.1029/2008WR006803.
- Ye, M., Neuman, S.P., Meyer, P.D. 2004. Maximum likelihood Bayesian averaging of spatial variability models in unsaturated fractured tuff. *Water Resour. Res.* 40(5), W05113. doi: 10.1029/2003WR002557.



Annex I - Hydrogeological cross sections of the Cremona Aquifer

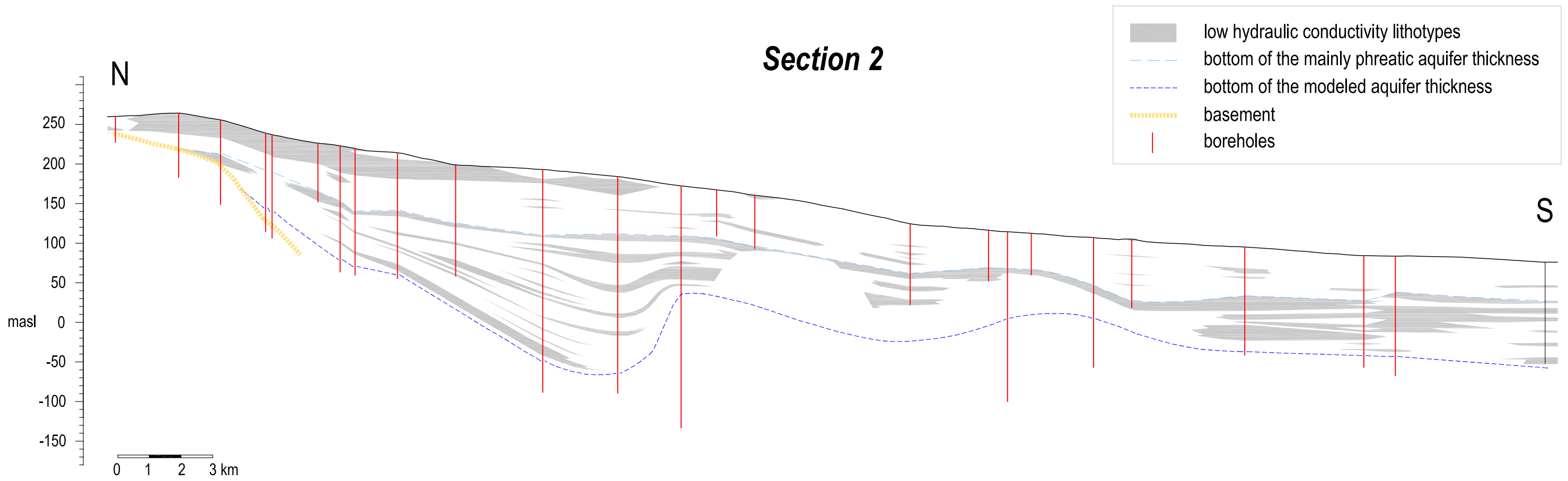


Limits of the study area together with the location of the hydrogeological cross sections. Cross sections are modified from Maione et al., 1991.



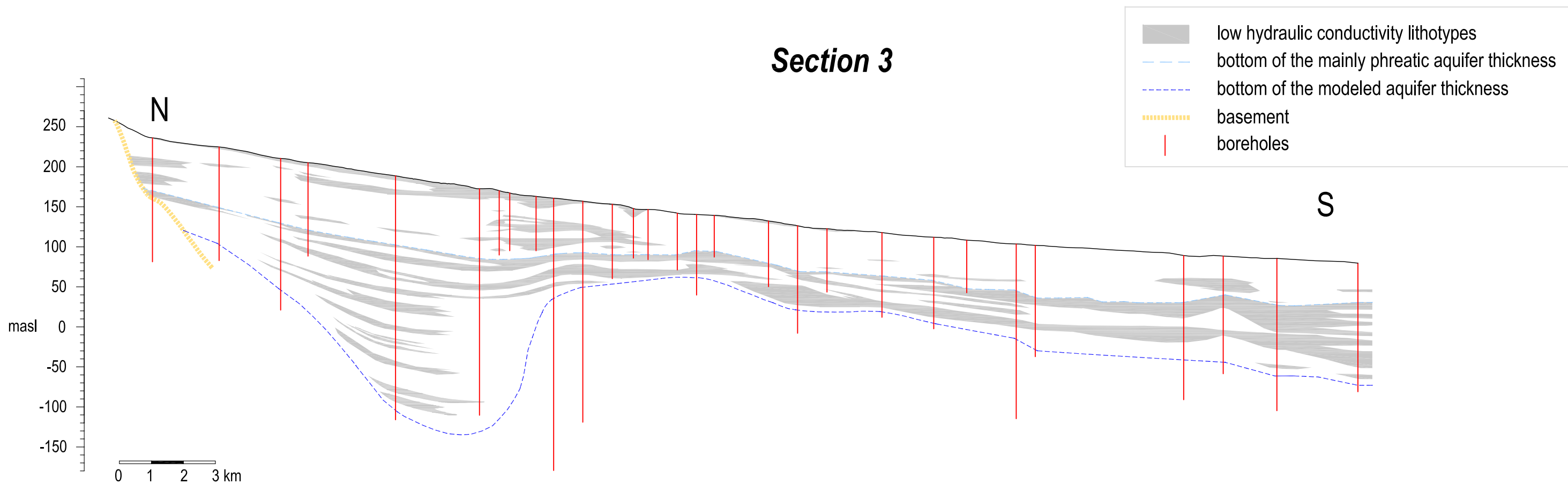


Section 2



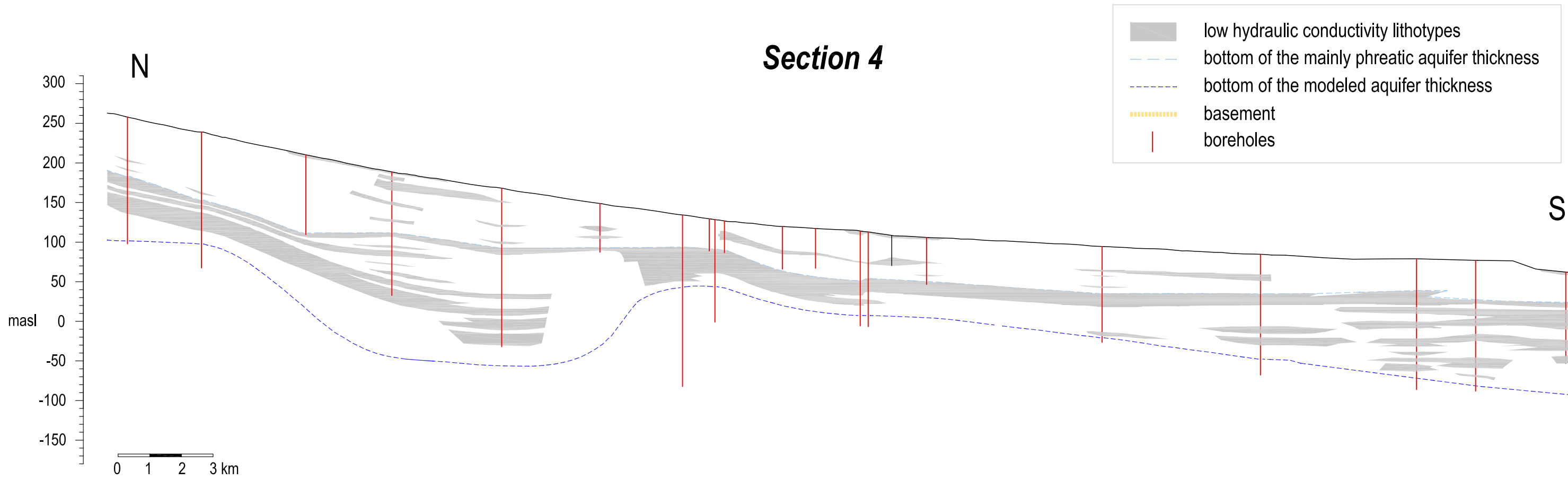


Section 3



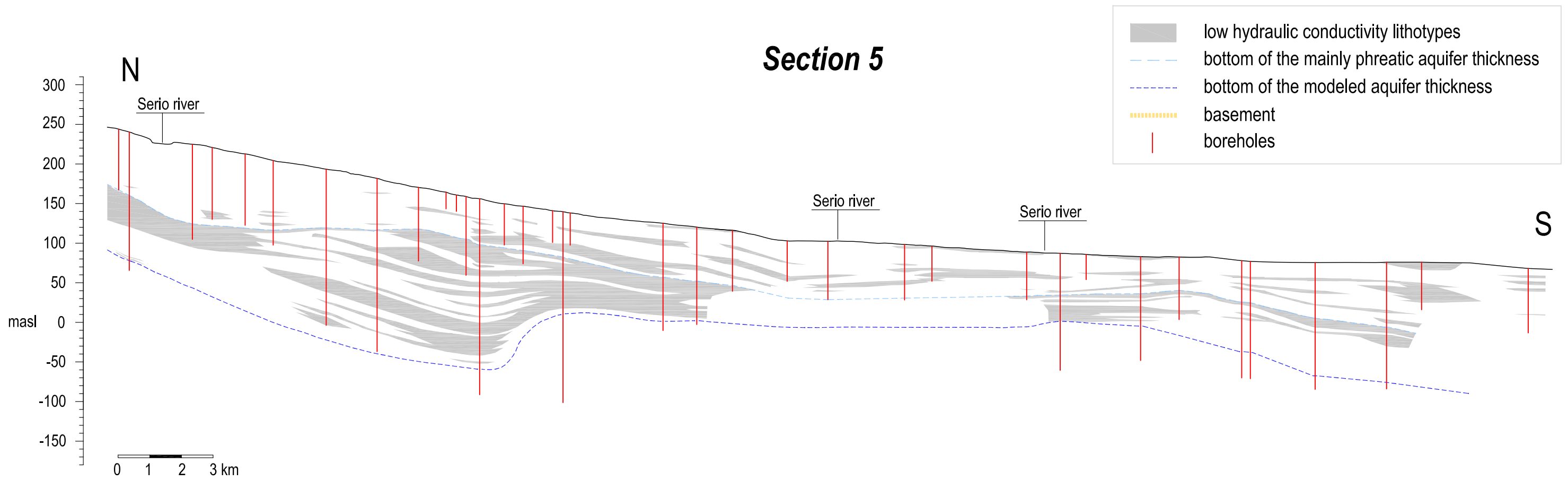


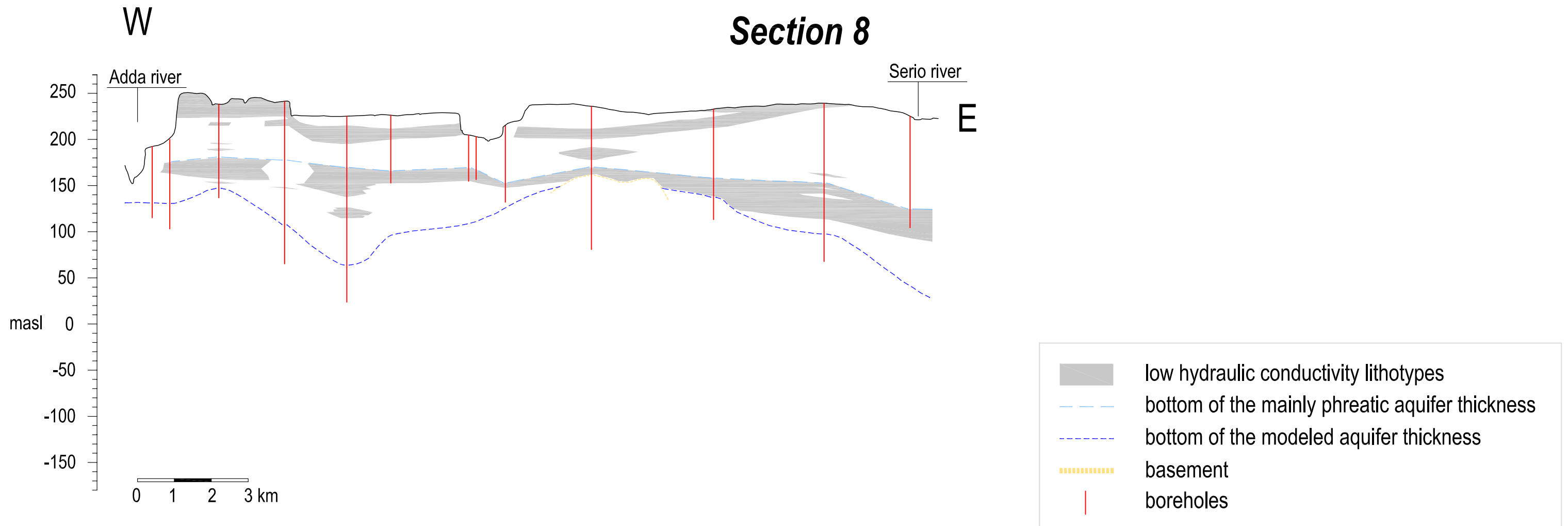
Section 4





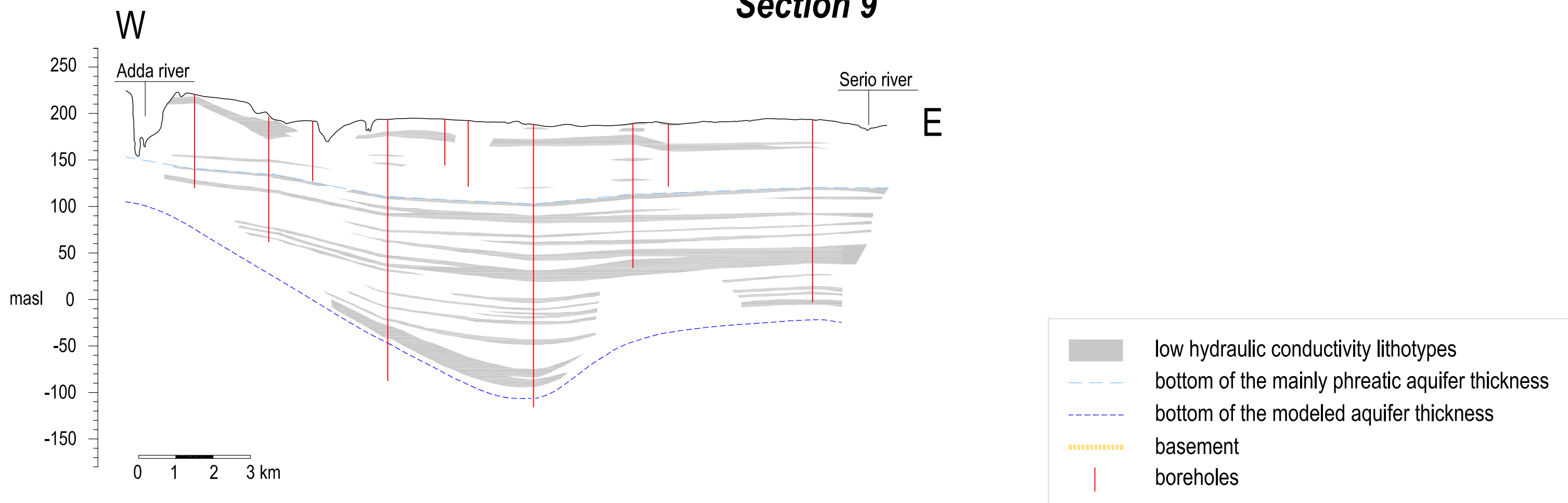
Section 5

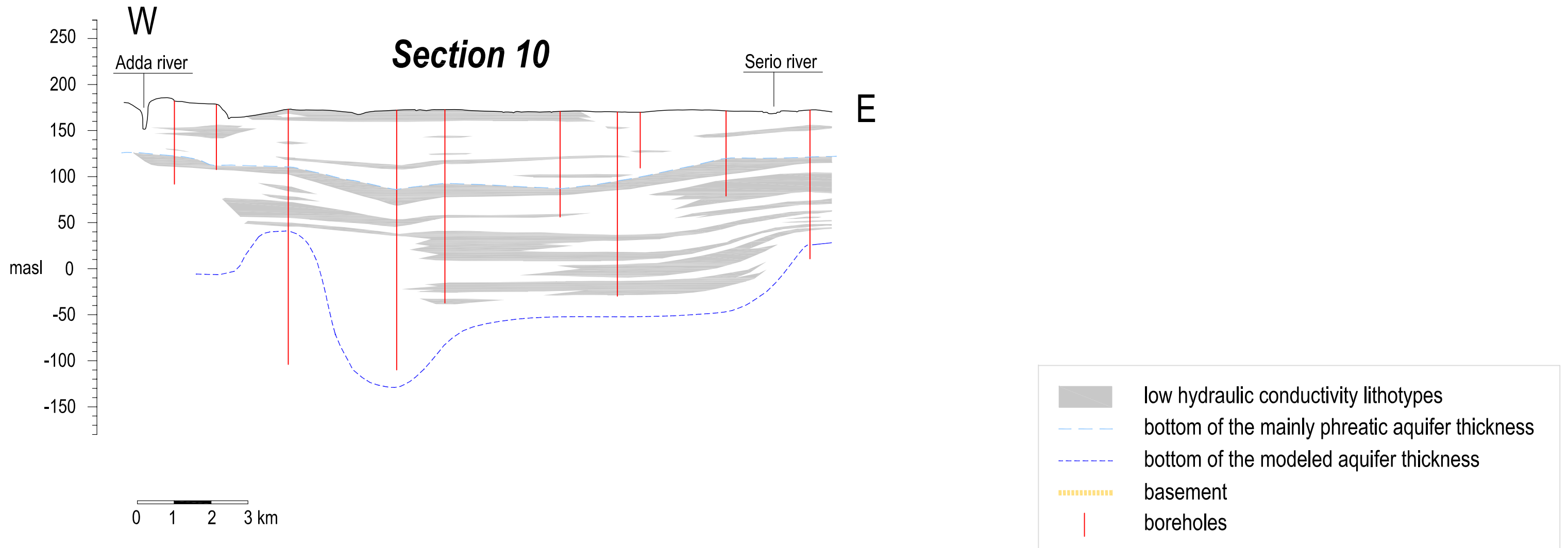


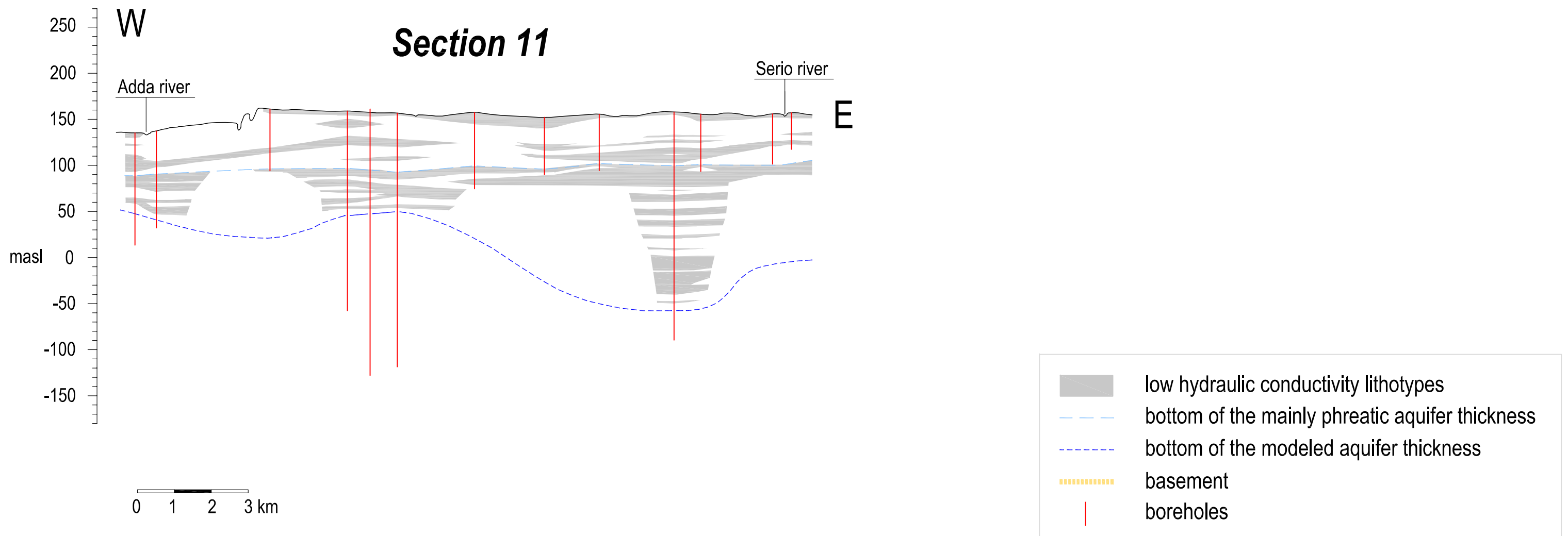




Section 9

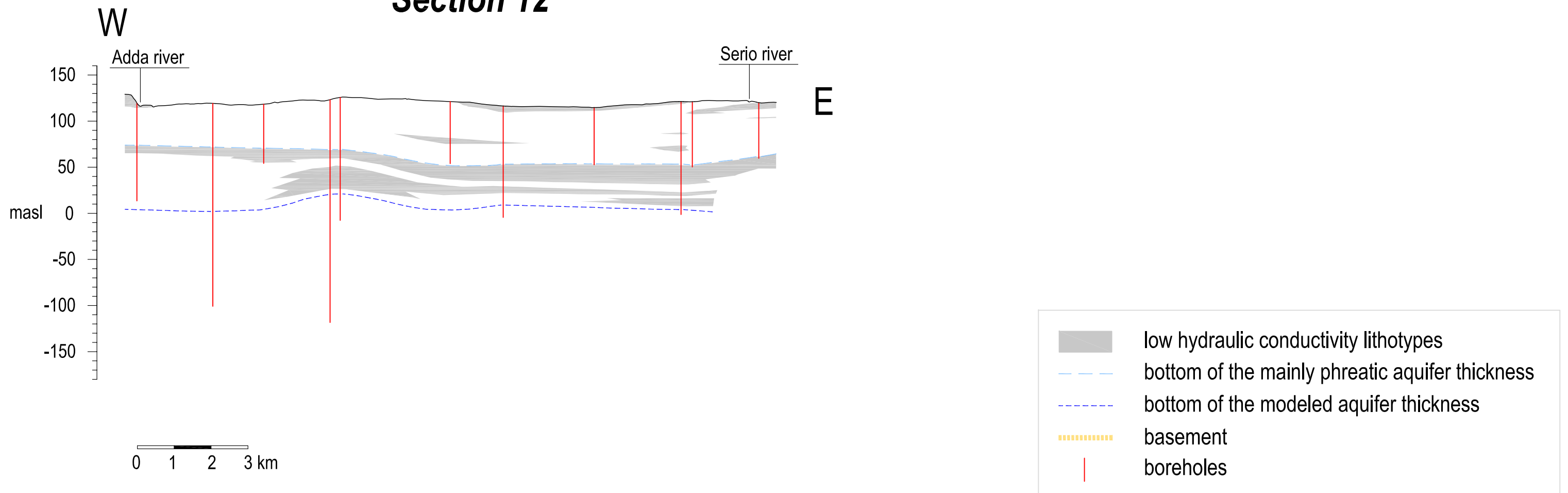






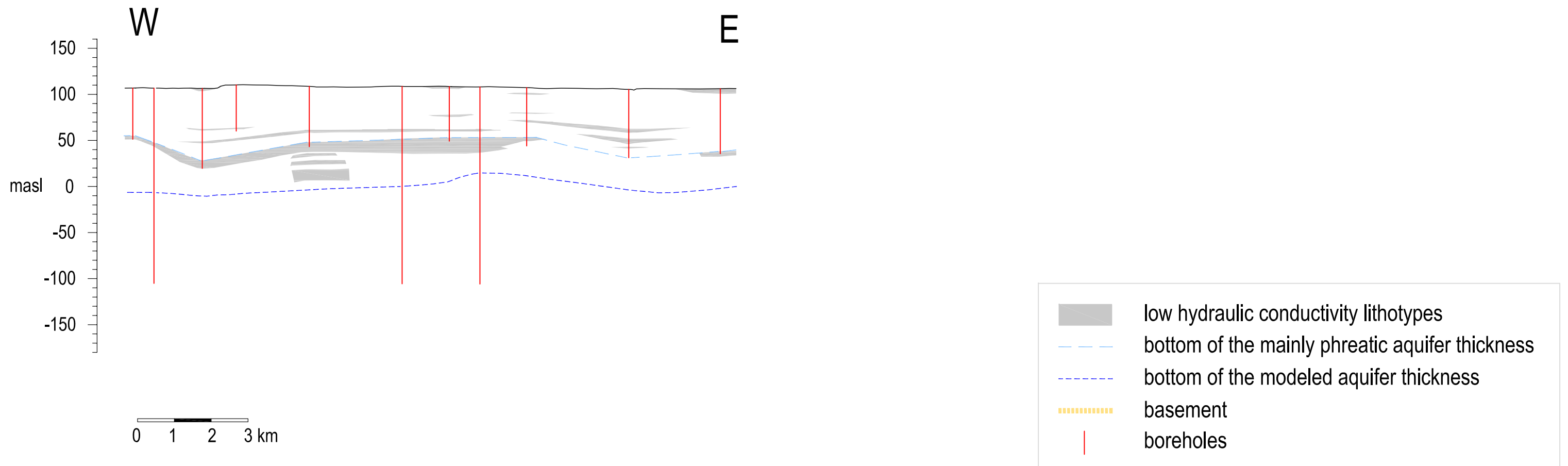


Section 12



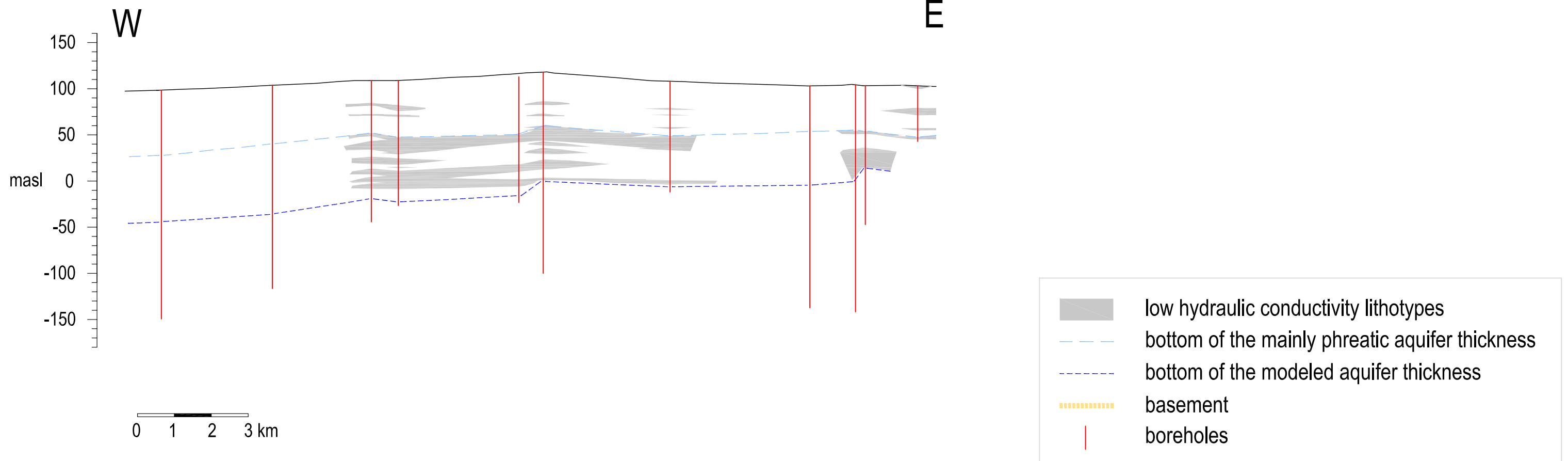


Section 13



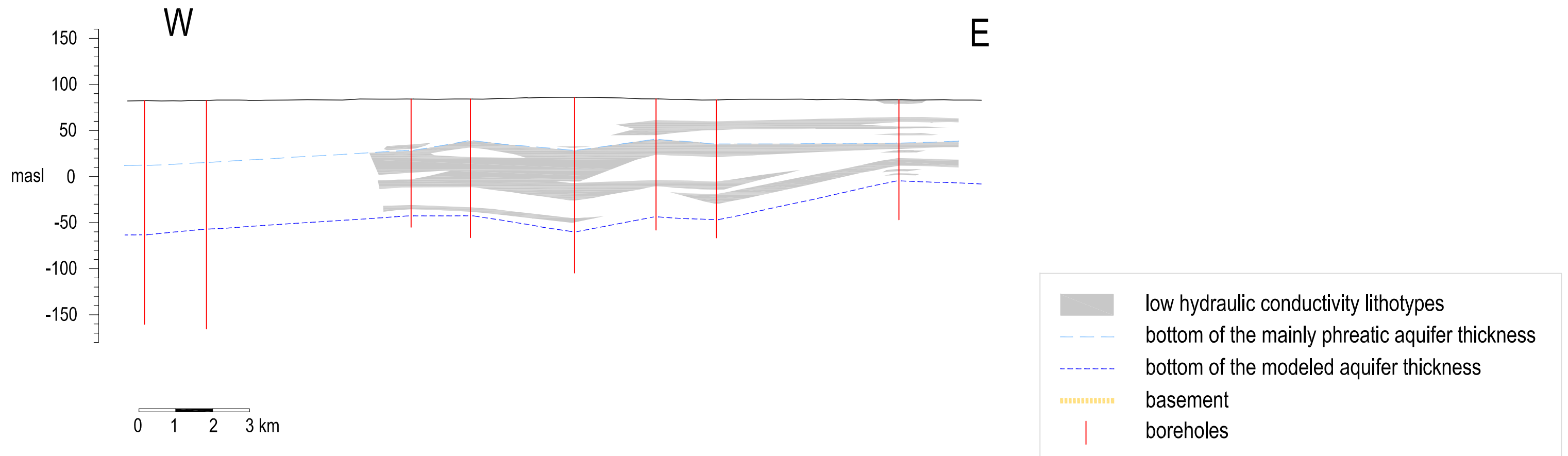


Section 14



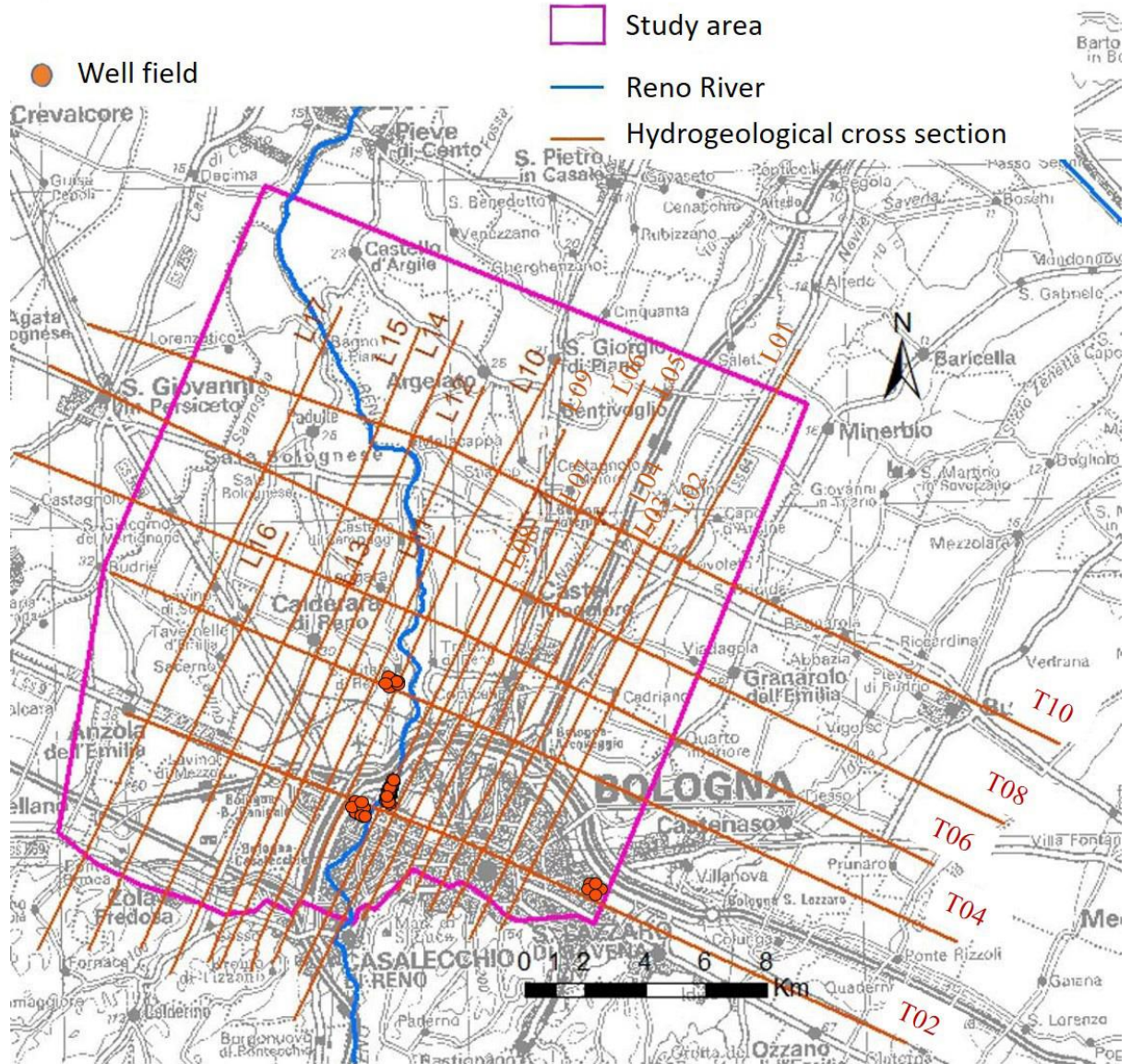


Section 15





Annex II - Hydrogeological cross sections of the Bologna Aquifer



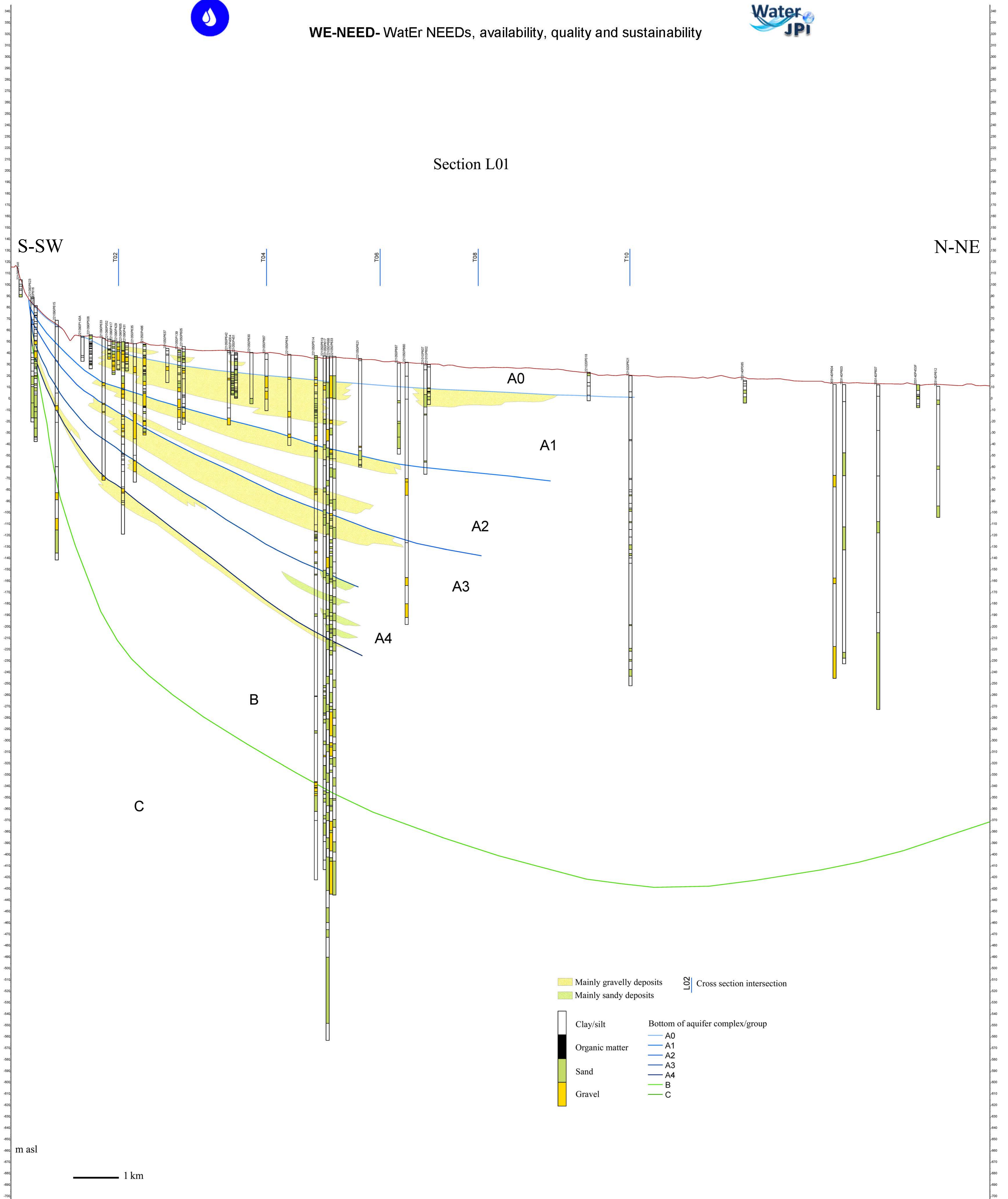
Limits of the study area together with the location of the well fields and hydrogeological cross sections. Cross sections are modified from cross sections provided by the Geological, Seismic and Soil Survey of the Emilia Romagna Region, available at https://applicazioni.regione.emilia-romagna.it/cartografia_sgss/user/viewer.jsp?service=geologia.



Section L01

S-SW

N-NE



m asl

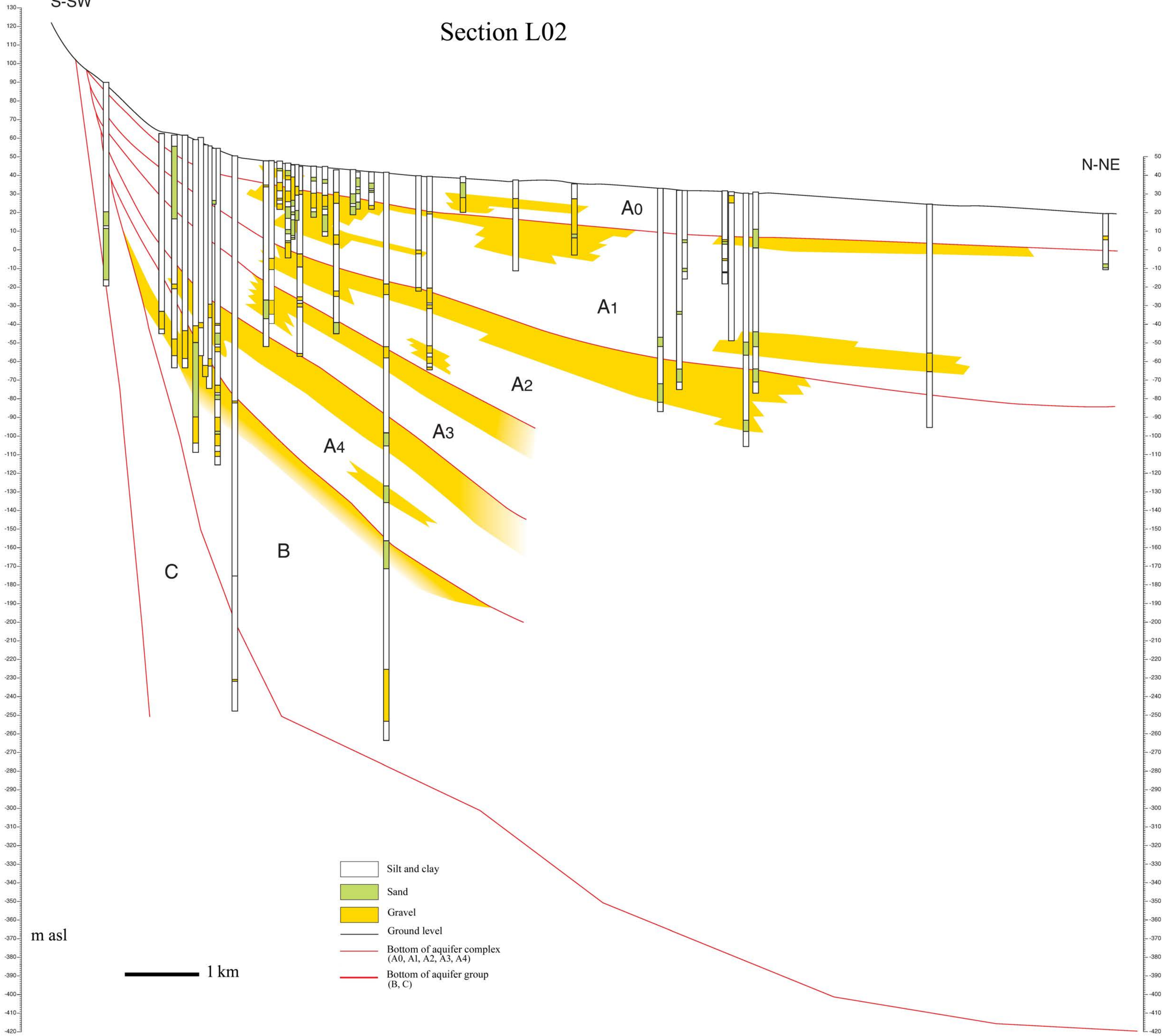
1 km



S-SW

Section L02

N-NE



m asl

1 km

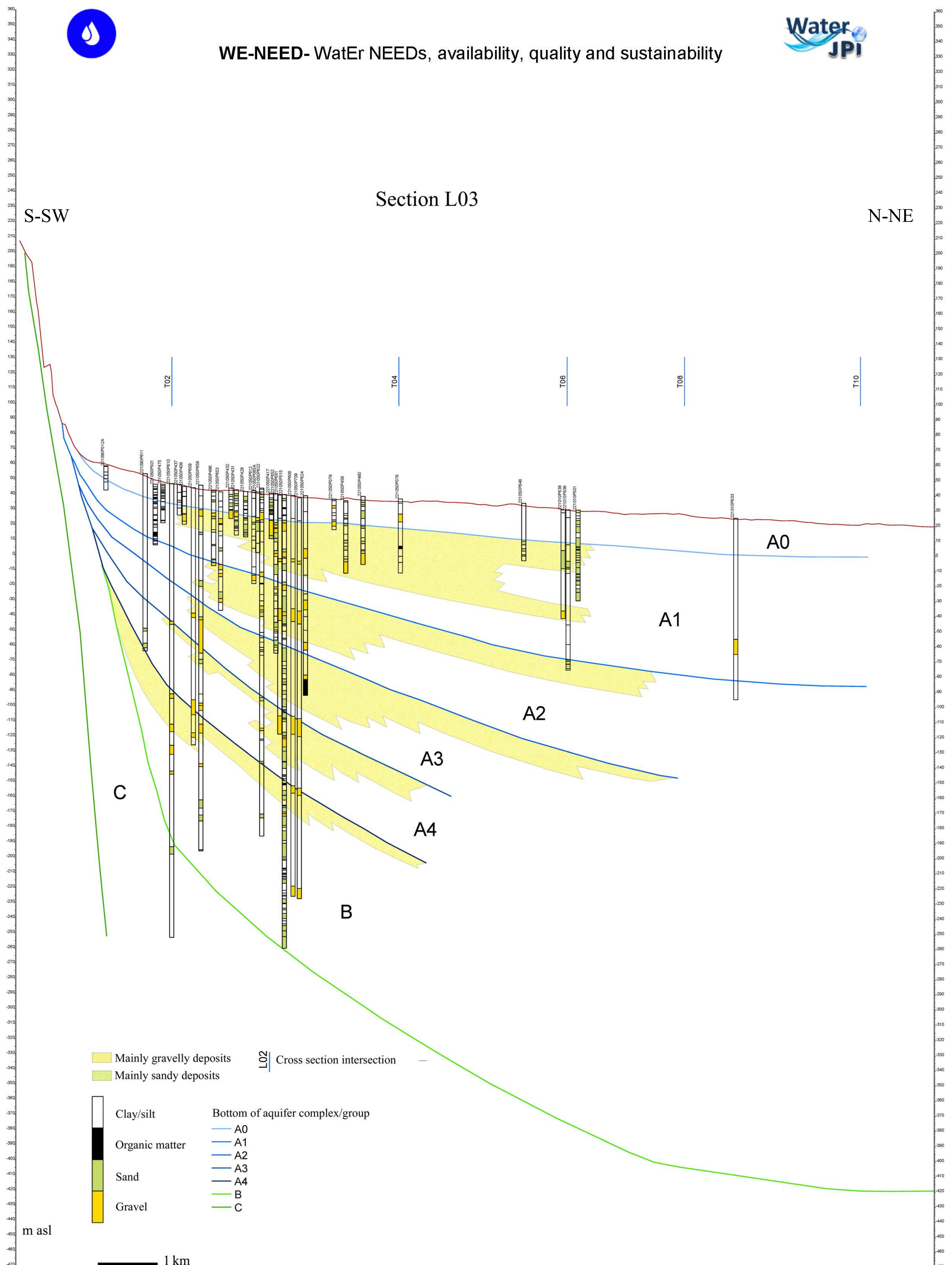
- Silt and clay
- Sand
- Gravel
- Ground level
- Bottom of aquifer complex (A0, A1, A2, A3, A4)
- Bottom of aquifer group (B, C)



Section L03

S-SW

N-NE



- Mainly gravelly deposits
- Mainly sandy deposits
- Clay/silt
- Organic matter
- Sand
- Gravel
- Bottom of aquifer complex/group
- A0
- A1
- A2
- A3
- A4
- B
- C

m asl

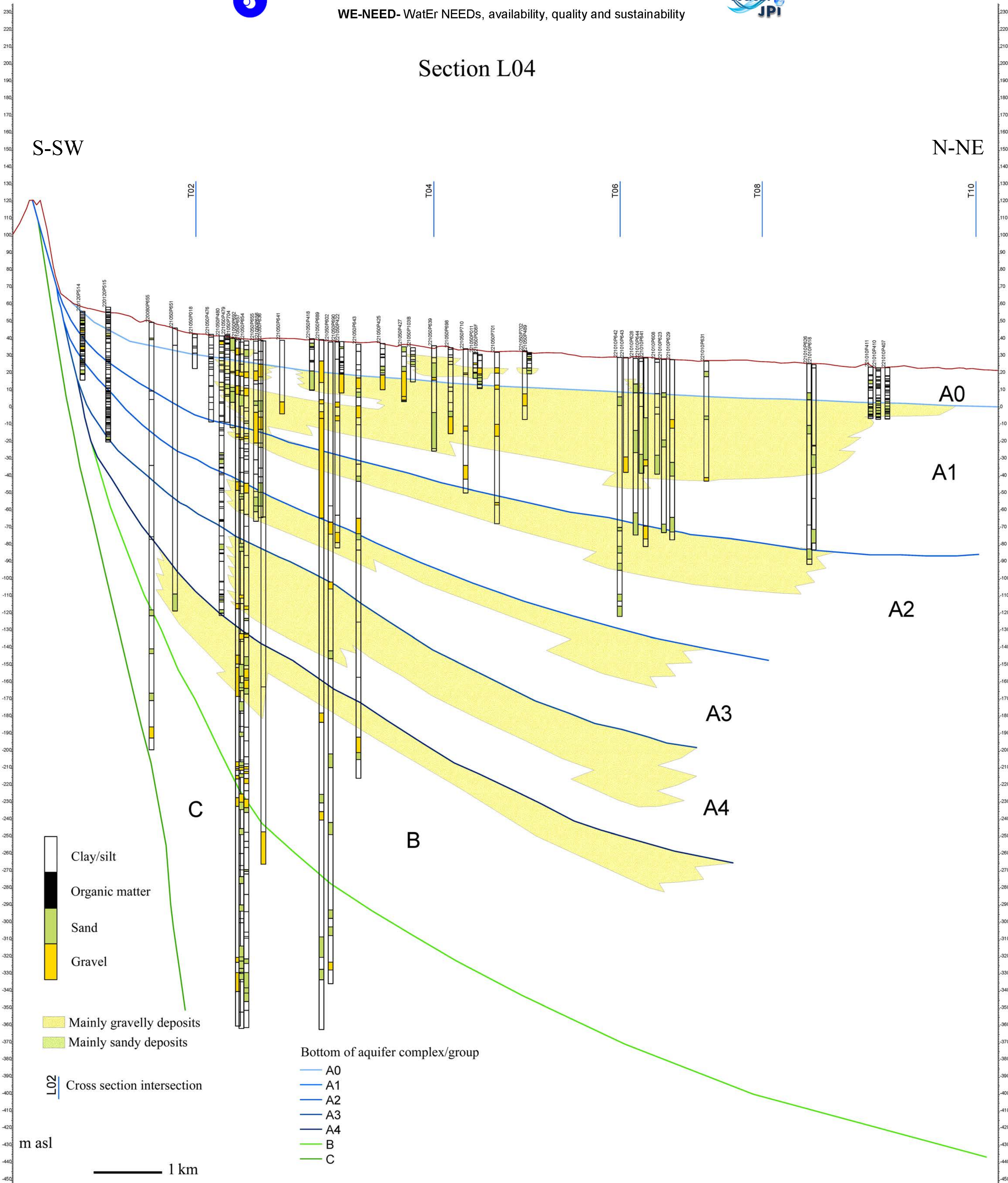
1 km



Section L04

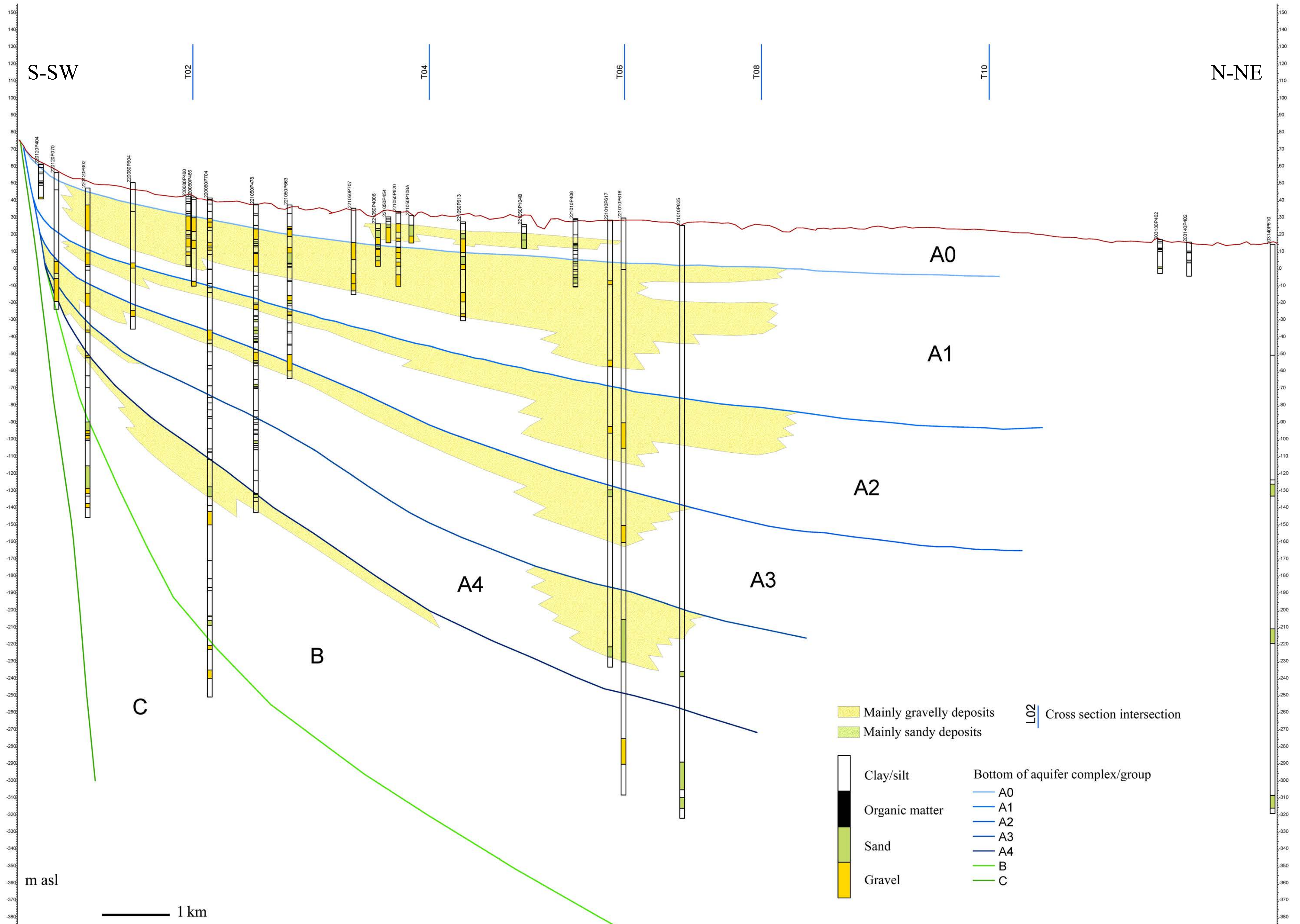
S-SW

N-NE





Section L05

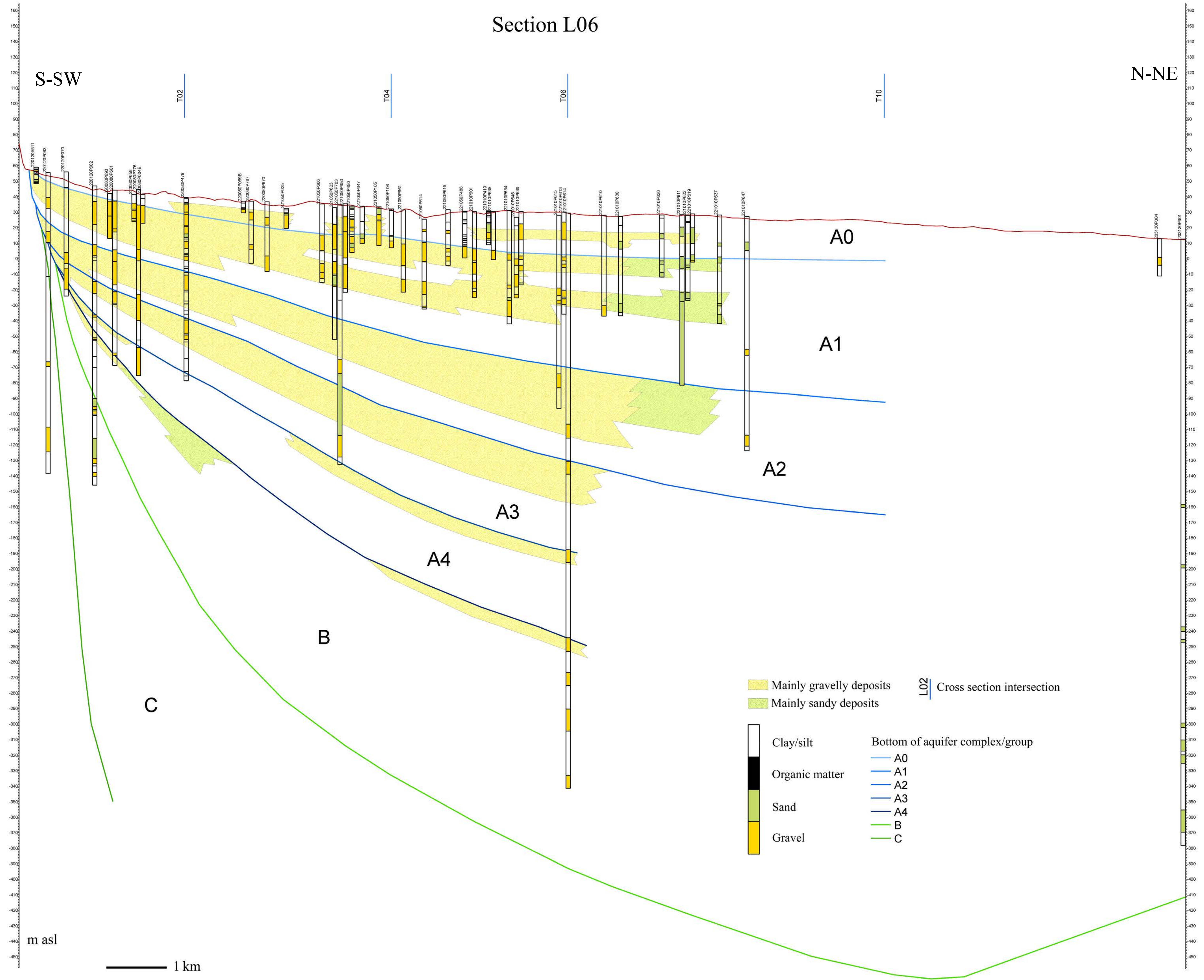




Section L06

S-SW

N-NE



- Mainly gravelly deposits
- Mainly sandy deposits
- Clay/silt
- Organic matter
- Sand
- Gravel
- Bottom of aquifer complex/group
- A0
- A1
- A2
- A3
- B
- C

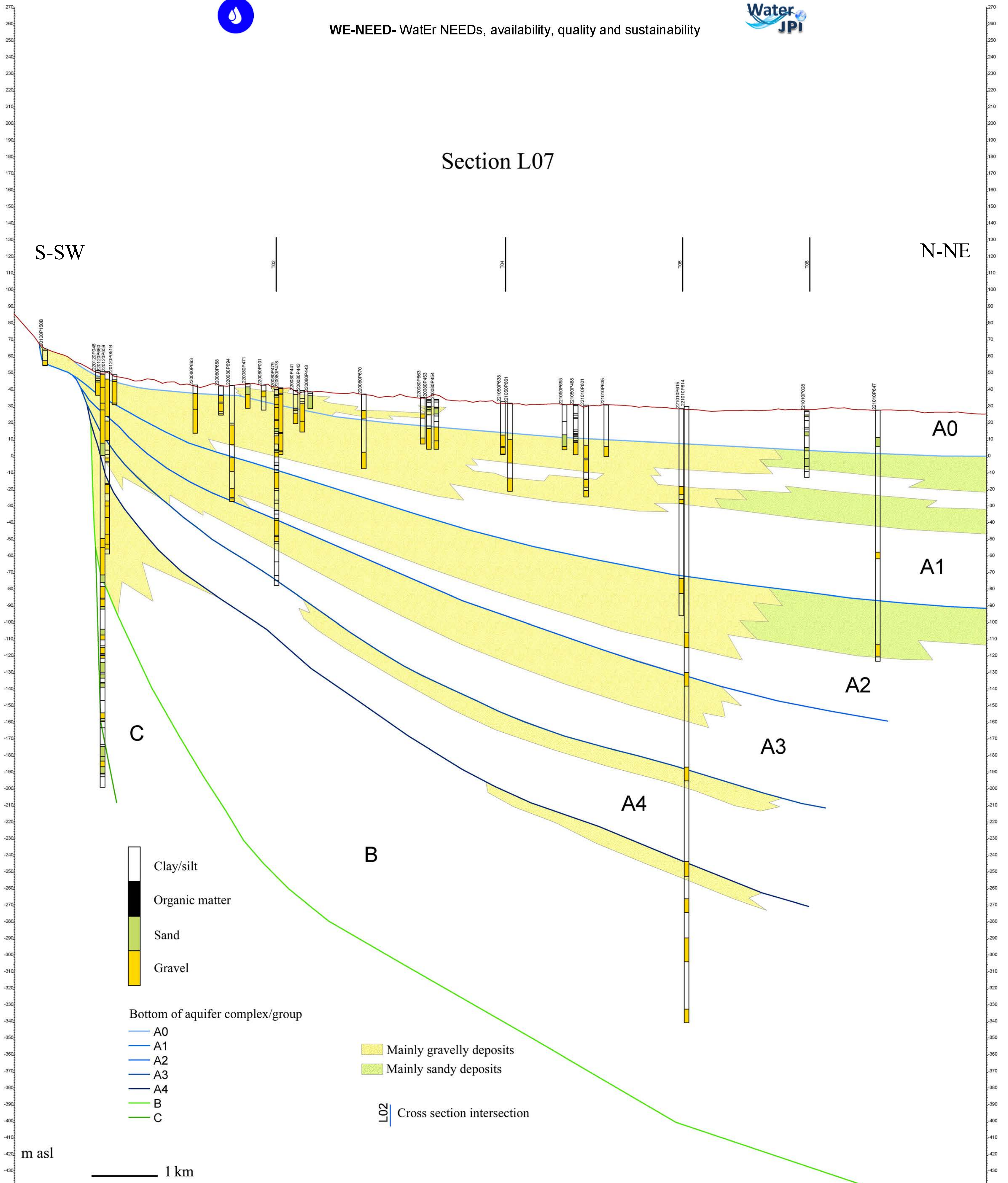
L02 Cross section intersection

m asl

1 km



Section L07



-  Clay/silt
-  Organic matter
-  Sand
-  Gravel

- Bottom of aquifer complex/group
-  A0
 -  A1
 -  A2
 -  A3
 -  A4
 -  B
 -  C

-  Mainly gravelly deposits
-  Mainly sandy deposits

L02 Cross section intersection

m asl

1 km

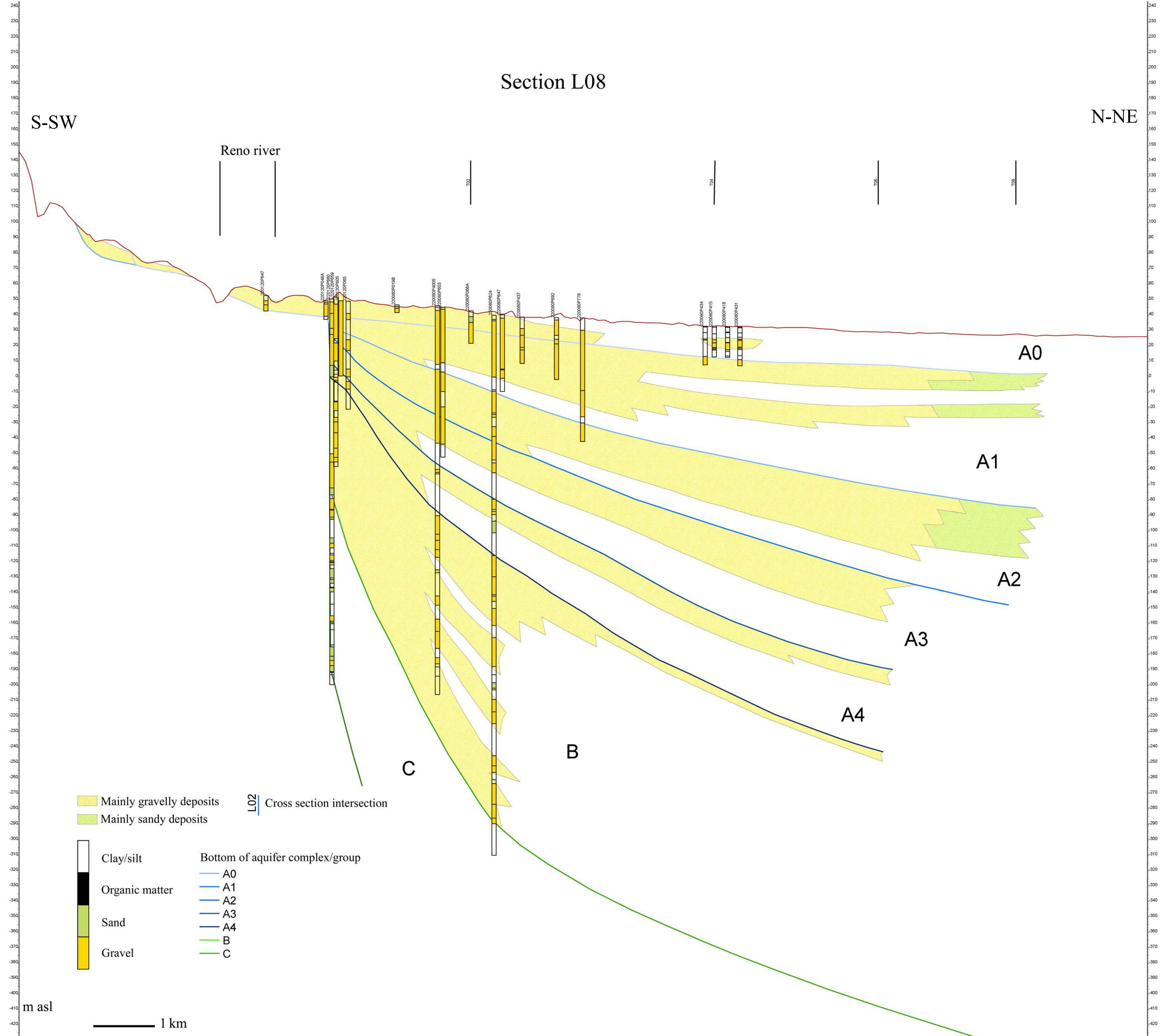


Section L08

S-SW

N-NE

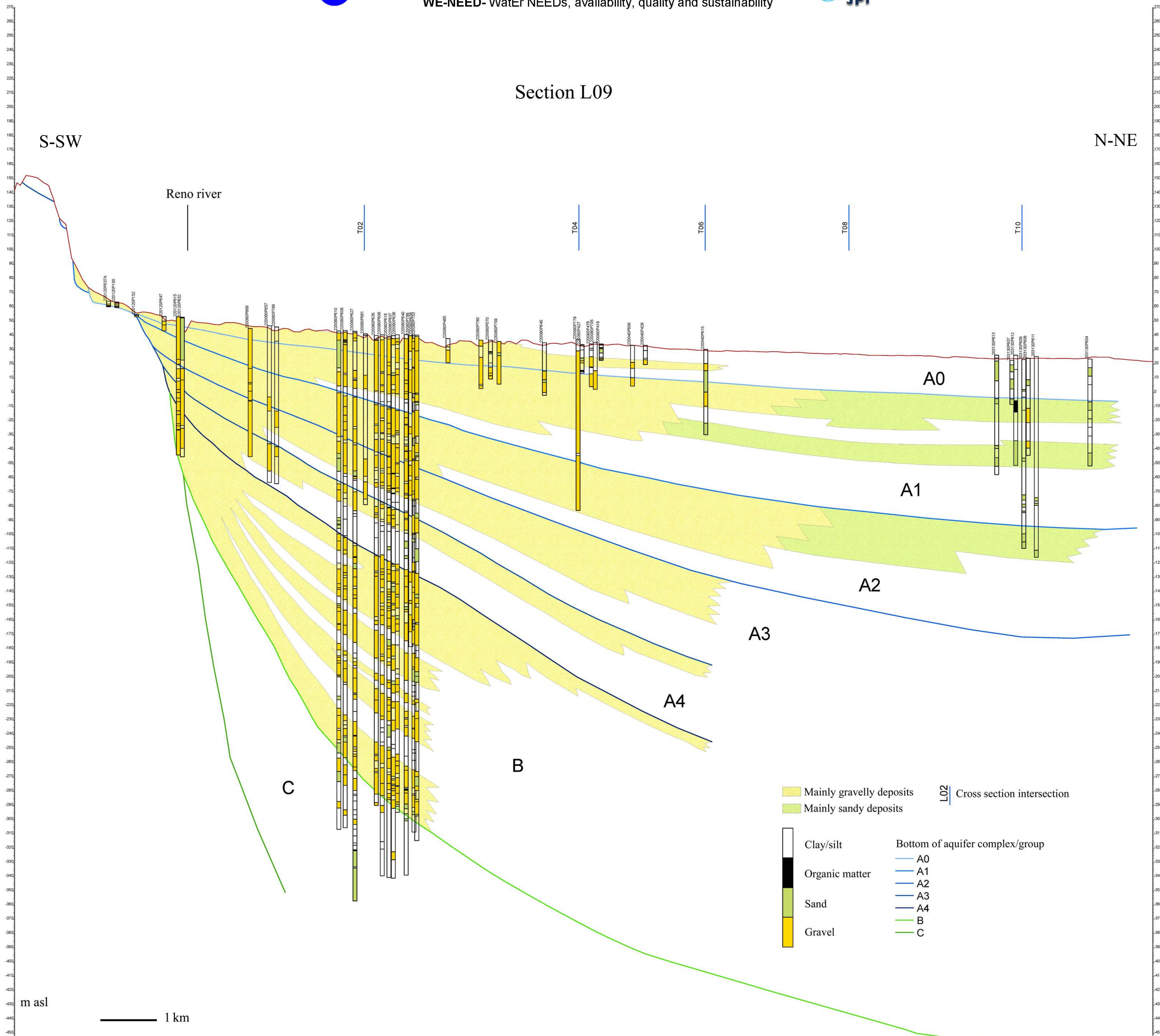
Reno river



- Mainly gravelly deposits
 - Mainly sandy deposits
 - Clay/silt
 - Organic matter
 - Sand
 - Gravel
 - Cross section intersection
- Bottom of aquifer complex/group
- A0
 - A1
 - A2
 - A3
 - A4
 - B
 - C



Section L09

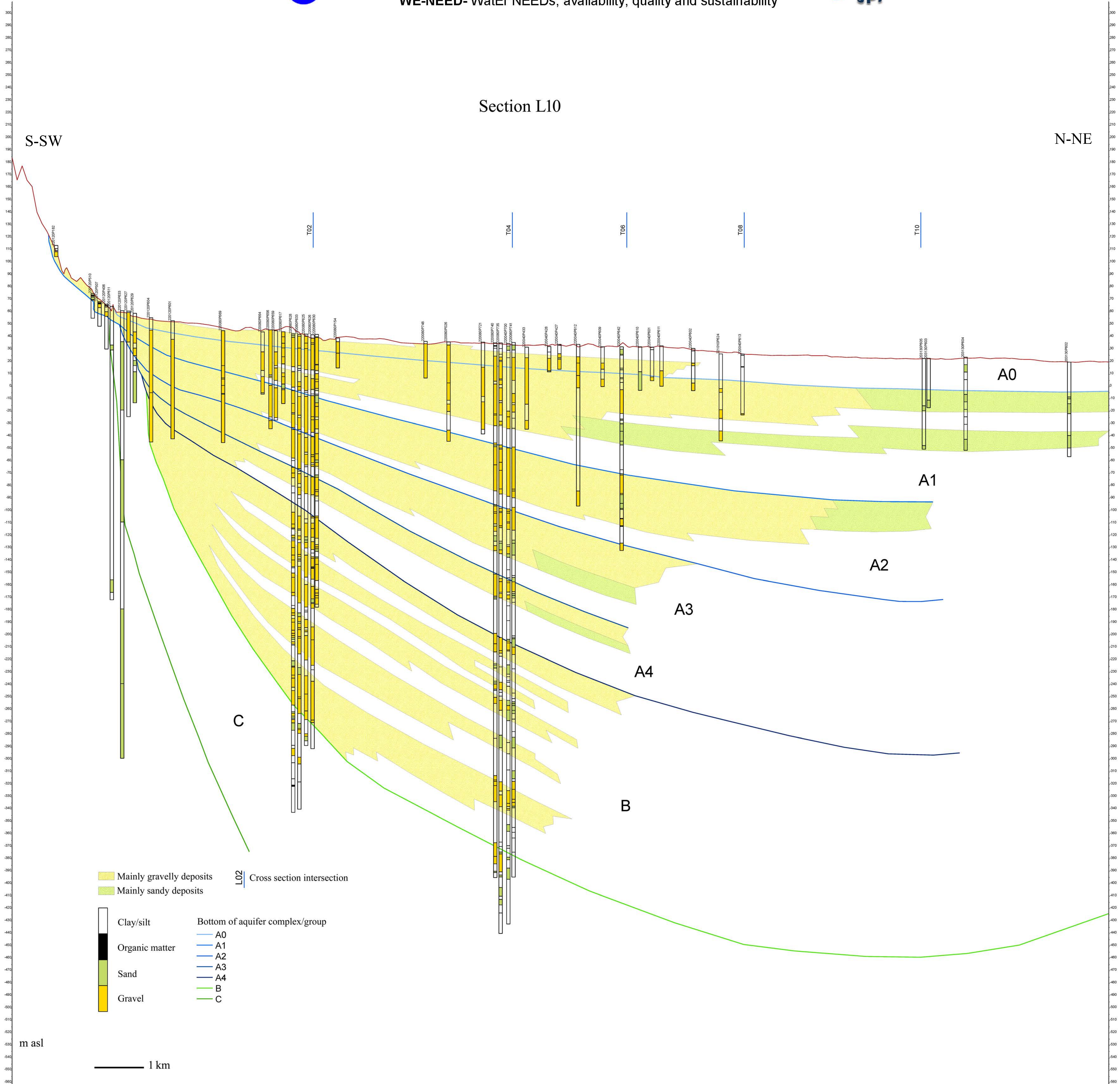




Section L10

S-SW

N-NE



- Mainly gravelly deposits
- Mainly sandy deposits
- Clay/silt
- Organic matter
- Sand
- Gravel
- Bottom of aquifer complex/group
- A0
- A1
- A2
- A3
- A4
- B
- C

L02 Cross section intersection

1 km

m asl